Informing Mars Sample Selection Strategies:

Identifying Fossil Biosignatures and Assessing Their Preservation Potential

by

Svetlana Shkolyar

A Dissertation Presented in Partial Fulfillment
of the Requirements for the Degree
Doctor of Philosophy

Approved October 2016 by the
Graduate Supervisory Committee:

Jack Farmer, Chair
Steven Semken
Thomas Sharp
Sang-Heon Dan Shim
Aaron Cody Youngbull

ARIZONA STATE UNIVERSITY

December 2016

ABSTRACT

The search for life on Mars is a major NASA priority. A Mars Sample Return (MSR) mission, Mars 2020, will be NASA's next step towards this goal, carrying an instrument suite that can identify samples containing potential biosignatures. Those samples will be later returned to Earth for detailed analysis. This dissertation is intended to inform strategies for fossil biosignature detection in Mars analog samples targeted for their high biosignature preservation potential (BPP) using in situ rover-based instruments. In chapter 2, I assessed the diagenesis and BPP of one relevant analog habitable Martian environment: a playa evaporite sequence within the Verde Formation, Arizona. Coupling outcrop-scale observations with laboratory analyses, results revealed four diagenetic pathways, each with distinct impacts on BPP. When MSR occurs, the sample mass returned will be restricted, highlighting the importance of developing instruments that can select the most promising samples for MSR. Raman spectroscopy is one favored technique for this purpose. Three Raman instruments will be sent onboard two upcoming Mars rover missions for the first time. In chapters 3-4, I investigated the challenges of Raman to identify samples for MSR. I examined two Raman systems, each optimized in a different way to mitigate a major problem commonly suffered by Raman instruments: background fluorescence. In Chapter 3, I focused on visible laser excitation wavelength (532 nm) gated (or time-resolved Raman, TRR) spectroscopy. Results showed occasional improvement over conventional Raman for mitigating fluorescence in samples. It was hypothesized that results were wavelength-dependent and that greater fluorescence reduction was possible with UV laser excitation. In Chapter 4, I tested this hypothesis with a time-resolved UV (266 nm) gated Raman and UV fluorescence spectroscopy

capability. I acquired Raman and fluorescence data sets on samples and showed that the UV system enabled identifications of minerals and biosignatures in samples with high confidence. The results obtained in this dissertation may inform approaches for MSR by: (1) refining models for biosignature preservation in habitable Mars environments; (2) improving sample selection and caching strategies, which may increase the success of Earth-based biogenicity studies; and (3) informing the development of Raman instruments for upcoming rover-based missions.

This dissertation is dedicated to my parents, Fianna and Oleg Shkolyar. Thank you for instilling in me the sense of perseverance, creativity, commitment, and dedication that brought me here.

This is also dedicated to my husband, Marc Neveu. Thank you for your love, guidance, and encouragement throughout our PhD journeys. I am grateful that our shared passions allowed us undertake the PhD journey, as well as many others, together.

ACKNOWLEDGMENTS

First, I would like to first acknowledge my advisor, Jack D. Farmer, for shaping me into researcher I have become. I will always be thankful for his support, guidance, enthusiasm, friendship, and passion for his equal roles in research and mentorship.

I would like to acknowledge financial support from NASA Astrobiology Institute (NAI), ASU's School of Earth and Space Exploration (SESE), the ASU SESE 2016 Summer PhD Student Research Award, the NASA Space Grant program, the NASA-SETI (Search for Extraterrestrial Intelligence) Institute, the NASA Mars Program, and ASU's Graduate and Professional Student Association (GPSA) Graduate Education Graduate Research and Support Program (GRSP) funding. Additional travel support to attend professional meetings and collaborating facilities was provided by grants from the NAI Early Career Collaboration Award and the ASU Graduate and Professional Student Association (GPSA). I gratefully acknowledge the use of two ASU facilities for the analytical instrumentation used in this dissertation: the LeRoy Eyring Center for Solid State Science and the John M. Cowley Center for High Resolution Electron Microscopy.

Analyses on the 532 nm time-resolved Raman spectroscopy instrument described in Chapter 3 were carried out at the Jet Propulsion Laboratory, California Institute of Technology, under a contract with the National Aeronautics and Space Administration (NASA). Support from NASA JPL Strategic University Research Parternship (SURP), the NASA JPL Student-Faculty Programs Office, and NASA Mars exploration Program are acknowledged for this work. Analyses on the 266 nm gated Raman and fluorescence spectroscopy instrument described in Chapter 4 were carried out at York University's Centre for Research in Earth and Space Science (CRESS) in Toronto, Ontario.

Finally, I would like to acknowledge those whose feedback, insights, and analytical help made this research possible. Dr. Steven Semken, Dr. Thomas Sharp, Dr. Sang-Heon Dan Shim, and Dr. Cody Youngbull are thanked for invaluable input throughout the years as members of my graduate committee. I would also like to thank Dr. Erik Alerstam (JPL), Candace Ashley (ASU), Christopher Haberle (ASU), Dr. Yuki Maruyama (JPL), Dr. Emmanuel Soignard (ASU), Dr. Nathan R. Williams (ASU), Dr. Axel Whittmann (ASU), and Dr. Natalya Zolotova (ASU) for helpful contributions to this dissertation research.

TABLE OF CONTENTS

Page

CHAPTER Page

CHAPTER Page

CHAPTER Page

LIST OF TABLES

LIST OF FIGURES

CHAPTER 1

INTRODUCTION

The search for life on Mars has been identified as a top priority by NASA's most recent Planetary Science Decadal Survey and other similar documents from the Mars Exploration Program (including those from the Mars Exploration Program Analysis Group, or MEPAG). A Mars Sample Return (MSR) mission will be the first step towards fulfilling this goal, carrying a rover with an *in situ* instrument payload to identify and cache the highest priority samples for later Earth return.

The purpose of MSR will be to maximize the chances of finding potential biosignatures in samples. Biosignatures are characteristic features (i.e., elements, molecules, morphologies, mineral assemblages) that can be used as evidence of past or present life, and are distinct from an abiogenic origin. Detailed Earth-based analyses are more likely to confirm or reject the biogenicity of potential biosignatures found on Mars.

The most widespread and abundant biosignature on Earth is kerogen, a degraded, macromolecular form of fossilized organic matter. (Of the organic matter that is buried, ~80% is found as kerogen.) Kerogen is commonly captured and preserved in aqueous sedimentary rocks, such as shales, clays, evaporites (e.g. sulfates), and two common host rocks for Precambrian fossils on Earth: carbonates and chert. These lithotypes have been repeatedly confirmed on Mars over the last decade, both from orbit and by *in situ* rover analyses. These lithotypes are considered high-priority targets in the search for a Martian fossil record and provide the primary focus for this dissertation.

To maximize the chances that rover-based biosignature searches will succeed on Mars, sample- and instrument-dependent strategies should be developed ahead of time, using realistic Mars analog samples which have high biosignature preservation potential, or BPP. Finding the highest BPP samples on Mars is a major priority of the Mars Exploration Program, yet the concept of BPP is not well constrained, or even well understood, in terrestrial sedimentary systems, especially across the different subfacies that comprise a single, complex depositional environment. Chapter 2 explores an example of how to approach constraining BPP across different subfacies in one relevant Mars analog environment - a Miocene-Pliocene evaporite playa lake.

Analog studies using samples representing what is or was present on Mars are intended to inform sample targeting and biosignature detection strategies in preparation for rover-based *in situ* analyses on Mars. However, often times, these studies assume simple mineral and organic "analogs" that are pure, synthetic, and not representative of complex, natural biosignatures preserved within (and interacting with) their mineral host matrices. As exemplified by the biosignatures found in the terrestrial rock record, any organics found in the Martian rock record will most likely contain organic compounds as complex mixtures with minerals. Such sample complexities are typically not captured in the pure samples and mixtures used in many analog studies (e.g., in synthetic quartz sand mixed with controlled amounts of aromatic organics isolated in solution, or in purified, extracted kerogen). Although valuable information can be obtained from simple synthetic samples, understanding the performance of rover-based payload instruments should be based on studies of realistic Mars analog samples that are likely to be targeted for successful rover-based missions.

When MSR occurs, the sample mass returned will likely be restricted to a limited mass of <500 grams. Thus, there is great need for *in situ* instruments that can accurately select the most promising samples for cache and later return to Earth.

Raman spectroscopy is one favored technique for identifying aqueous samples with high BPP. The technique has a successful history for performing useful *in situ* analyses of both organic and inorganic compounds in geological samples on Earth. Raman is a vibrational spectroscopy technique in which an incoming laser signal is inelastically scattered off of a sample surface, exchanging energy with the sample. The difference between the outgoing and incoming laser energy (and by extension, frequency) is termed Raman shift (which is the x-axis of a Raman spectrum). This allows for non-destructive identification of mineral and organic structures, as well as their mixtures, with high sensitivity, speed, and efficiency. Because different molecules have varied structures and bond strengths, a Raman spectrum can provide a fingerprint of a molecule as sharp, discrete, narrow peaks, each indicating unique molecular bonds and functional groups. Another benefit of Raman is that signals may be collected from meter-scale distances.

The next two Mars rover missions are planned to launch within the next 5 years. This includes NASA's Mars 2020 rover and European Space Agency's ExoMars rovers, together planned to carry a total of three laser Raman spectrometers in their payload instrument suites. The Mars 2020 rover payload is planned to include two Raman spectroscopy instruments: (1) The Scanning Habitable Environments with Raman & Luminescence for Organics & Chemicals instrument (SHERLOC), an arm-mounted, resonance Raman and fluorescence spectrometer, with a CW deep UV 248.6 nm laser source; and (2) the SuperCam, an integrated suite of four instruments, that includes a

spectrometer with gated excitation at 532 nm for Raman and fluorescence measurements. ExoMars, scheduled for launch in 2018, is planned to include a 532 nm CW Raman Laser Spectrometer (RLS). A major goal of all three Raman payload instruments will be to identify samples that contain potential organic biosignatures, whether for *in situ* analyses (i.e., all three instruments) and / or caching and earth return (i.e., Mars 2020).

This dissertation is motivated by recommendations to inform biosignature studies on Mars using realistic analog samples, and to improve *in situ* Raman spectroscopy techniques targeted for astrobiology investigations. Two themes are woven together throughout this dissertation: (1) understanding sample-dependent challenges in complex natural mixtures as Mars analog samples and (2) understanding instrument-dependent considerations for improving rover-based Raman instruments. Both themes are equally emphasized to highlight their co-dependence in the planning stages of successful Mars rover mission development.

These themes are addressed in Chapter 2, "Biosignature Preservation Potential in Playa Evaporites: Impacts of Diagenesis and Implications for Mars Exploration," where one particularly challenging, relevant, and little-studied Mars analog environment is studied. This study examines an ancient evaporative dry lakebed (playa), within the late Miocene to early Pliocene Verde Formation of central AZ. In the outcrop examined, evaporite formation was favored by playa development, within an arid basin with a negative water balance, which remains dry 75% of the year. Although evaporites have been known at the evaporite quarry since ancient times, this is the first known study to examine Verde Basin playa evaporites in an astrobiological context with the goal to inform Mars rover instrument strategies.

The goals of the study described in Chapter 2 were to investigate (1) the diagenetic processes (i.e., post-depositional alteration) that affected the Verde Fm. playa evaporites and (2) the impact of diagenesis on the BPP of biosignatures within the subfacies identified. This study combines outcrop-scale observations, diverse field-collected samples, and laboratory analyses, including: (1) thin-section petrographic microscopy; (2) X-ray powder diffraction; (3) Raman spectroscopy; (4) Total Organic Carbon (TOC) analyses; (5) electron microprobe; and (6) visible to near infrared reflectance (VNIR) spectroscopy. Using this suite of instrument analyses highlighted the importance of using diverse complimentary capabilities to enhance the overall understanding of an environment and BPP, both on a rover and in the laboratory.

In Chapter 2, a model is presented for the diagenetic evolution of the Verde Fm. playa system originating from a Mg-Na-Ca-SO_4-Cl brine type in a hydrologically open continental basin. During initial deposition in the Miocene, fine-grained clay-rich silts and muds from alluvial fan sources along the southern basin margin were deposited on the playa surface. Four major diagenetic events in the history of the play are discussed in Chapter 2: (1) In the shallow subsurface, early displacive growth gypsum (DGG) crystallized within playa muds and underwent five later-stage alteration events. Gypsum dissolved and formed cavities within muds. Dissolution cavities were infilled with secondary gypsum and in some instances, recrystallized to coarser grain sizes. Gypsum also dehydrated to intermediate hydration state Ca-sulfates, or experienced Na-Ca-Sr cation substitution; (2) Another diagenetic event was marked by shallow ponded brine pans forming by evaporite dissolution on the playa surface. These depressions accreted locally, forming pods dominated by bottom-nucleated halite. The outer edges of the halite

pods were later replaced with thenardite; (3) The final stages of playa deposition during the Pliocene, were marked by cyclic oxidation and cementation by Fe-rich fluids in mudstones exposed in the upper quarry; (4) Finally, during the Pleistocene, a lake developed covering most of the Verde Basin. This lake system laid down extensive lacustrine limestones, associated with the Mg-carbonate cementation of playa mudstones. This marked the last diagenetic event in the system.

Chapter 2 also presents a model for the long-term BPP in Verde Fm. evaporites by comparing biosignature preservation over the four inferred diagenetic pathways. As a proxy for BPP, Total Organic Carbon (TOC) analyses reveal that mudstones, including Fe-oxidized mudstones, revealed higher BPP. BPP was lower for the DGG and halite-thenardite subfacies.

During investigations of the Verde Fm. playa evaporites, a major limitation was encountered with one of the analytical instruments used: Raman spectroscopy. Interference from high-background fluorescence in Raman spectra proved to be a problem in confidently identifying kerogen and minerals. Overwhelming fluorescence can impede reliable Raman-based identification of organics and minerals, especially in lithologies targeted for MSR. When light interacts with matter, the Raman scattering process is weak and has to compete with absorption effects, such as fluorescence. Fluorescence is a laser-induced effect that occurs when a photon incident on a molecule excites an electron to a vibrational level in a higher electronic state. The electron will subsequently settle back to the ground vibrational level of the first excited electronic state, emitting a photon. The molecule then relaxes from its vibrationally excited level back to the lowest vibrational level of the electronic state. Fluorescence originates from

two long (>10 ns to ms) lifetime effects arise from inorganic sources, such as lattice defects and impurities in the mineral lattice (e.g., trace metals, or rare Earth elements) and short (<1-10 ns) lifetime effects that arise from chromophores in the organic matter. Many complex organics exhibit fluorescence when excited with radiation that is often many orders of magnitude stronger than the Raman scattered signal. This issue has been previously noted in many previous Raman studies of minerals and organics, as detailed in Chapters 3-4.

Investigating a way forward for rover-based Raman spectroscopy analyses of biosignatures in fluorescent samples provided the motivation for Chapter 3, "Visible Excitation Raman Spectroscopy for Fossil Biosignature and Mineral Identification: Challenges and Recommendations for Mars Sample Return." Of the various approaches developed to reduce fluorescence for commercial systems, the study in Chapter 3 investigates time-resolved Raman (TRR) spectroscopy. TRR captures the instantaneous Raman signal, while gating out longer lifetime fluorescence interference by using an optimized detector. (The principles of TRR fluorescence reduction with gating are illustrated in Fig. 3.1.)

In Chapter 3, Raman data taken with a 532 nm (visible) laser wavelength excitation TRR instrument are compared to that taken on a traditional, non-gated (continuous wave, or CW) Raman spectroscopy instrument. Samples were analyzed to emphasize similarities to settings found on Mars and which have been given top priority for fossil biosignature studies. Lithotypes surveyed for this study included sulfate evaporites, clay-rich shales, cherts, and carbonates. Chapter 3 results reveal that the successful identifications of kerogen and minerals with Raman in a range of natural

samples were highly sample-dependent, with laser-induced sample alteration and degradation effects occurring in some sample types. In addition, this study reveals that 532 nm wavelength excitation time-resolved Raman (TRR) analyses show limited success in reducing fluorescence.

It was hypothesized that the lack of significant improvement in Raman-based fluorescence reduction with 532 nm TRR was caused by the Raman laser excitation wavelength used. Visible excitation wavelengths may cause fluorescence but UV excitation reduces it for two reasons: (1) Raman and fluorescence bands are spectrally separated in the UV; and (2) Raman scattering is proportional to the fourth power of the excitation frequency, thus increasing sensitivity when moving to shorter (i.e., UV) wavelengths.

To investigate this hypothesis, the study in Chapter 4 investigates a UV TRR (266 nm) to interrogate the same diverse sample suite as in Chapter 3, including a highly fluorescent playa mudstone from the Verde Fm. sample suite (Chapter 2). Chapter 4, "Finding Biosignatures in Mars Analog Samples Using Visible and UV-Gated Raman Spectroscopy, And UV Time-Resolved Fluorescence Spectroscopy," presents two Raman-based fluorescence reduction techniques implemented by SHERLOC and SuperCam: UV excitation wavelength optimization and time gating. This chapter compares the performance of two Raman spectrometers: a 532 nm (visible) continuous wave (V-CW) Raman system and a 266 nm (UV) gated (UV-G) Raman combined with a UV laser-induced time-resolved (UVLITR) fluorescence spectroscopy system. The goals of Chapter 4 were to (1) assess the effectiveness of time-gating compared to laser excitation wavelength optimization as a Raman-based fluorescence reduction strategy to

enable successful caching of samples for MSR; (2) to identify sample-specific issues that could challenge the identification of samples using the two Raman spectroscopy systems described; and (3) to assess the capabilities of UVLITR fluorescence spectroscopy for detecting biosignatures in samples.

Three different data sets are presented for each sample: (1) standard Raman, (2) time-gated Raman, and (3) fluorescence spectra, along with independent methods to characterize minerals and organics in each sample (petrographic microscopy and XRPD). Raman and fluorescence data sets were acquired on the same locations on samples, which was possible since the spectrometer grating in the UV Raman instrument was interchangeable with one that collects in a fluorescence wavelength range. This allowed valuable information to be gained from coupling micro-scale Raman and fluorescence data of both minerals and kerogen on the same spot in samples without moving the sample from the instrument stage.

Chapter 4 results indicate that compared to V-CW Raman, UV-G Raman requires fewer attempts and allowed higher confidence when detecting minerals and organics without fluorescence interference. Chapter 4 also reveals two sample-dependent challenges that arose with both Raman systems: (1) challenges included successful V-CW Raman which depended on lithotype and kerogen maturity, and (2) the evaporitic mudstone sample complicated detections of matrix and kerogen components with both Raman systems). Fluorescence spectroscopy results reveal two diverse types of organic fluorescence present in all samples, even the challenging evaporitic mudstone.

The specifications of all Raman spectroscopy systems used in this dissertation as well as for those planned for ExoMars and Mars 2020 are summarized in Table 1.1.

Table 1.1

Specifications of all Raman Spectroscopy Systems.

System	λ_{ex} (nm)	Power	Range (cm^{-1})	Sampling Vol.	Spot size (μm)	Pulse rate (kHz)	Pulse energy (μJ)	Temp. pulse width (ps)	Pulse gate width (ns)	Min – max gate widths
Visible CW, ASU	532	0.75 - 25 mW	0 – 2000	Sample dep.	~1-5	NA	NA	NA	NA	NA
Visible gated, JPL	532	1-3 mW	0 – 2300	~10 um diameter; ~20 um length	~1-5	40	1	500	1	1-16 ns
UV, York Univ.	266	~5 mW	0 – 3500	Surface area	~20 x 35	5	1.6	700	1.5	7 ns -1 μs
RLS, ExoMars	532	0.6 -1.2 kW/ cm^{2*}	150 – 3800	Unknown	50	NA	NA	NA	NA	NA
SuperCam, Mars 2020	532	Unknown	150-4400	Unknown	<500	0.01	10	Unknown	Unknown	<100 ns
SHERLOC, Mars 2020	248.6	6 mW/ cm^2	810-3600	Surface area	50	NA	NA	NA	NA	NA

Table 1.1. Relevant specifications of all Raman spectroscopy systems used in this dissertation as well as those chosen for upcoming Mars rover missions (discussed in the text) are summarized here. All reported values are as used for experiments in this dissertation (for the laboratory Raman systems described) or as expected during interrogations on Mars (for the ExoMars and Mars 2020 instruments). CW denotes the continuous wave, or standard, ungated Raman system housed at ASU's LeRoy Eyring Center for Solid State Science in Chapters 2-4. "Visible gated" denotes the visible excitation wavelength gated system at JPL, detailed in Chapter 3. "UV" denotes the UV wavelength excitation gated Raman and fluorescence spectroscopy system used at York University's Centre for Research in Earth and Space Science (CRESS), detailed in Chapter 4. "RLS" denotes the Raman Laser Spectrometer planned for the ExoMars rover. "NA" denotes not applicable.
*This value is an irradiance level (Rull et al., 2011).

Finally, Chapter 5, "Concluding Thoughts," presents a brief synthesis of the results and implications presented in Chapters 2 – 4. Chapter 5 also details further studies that are recommended based on the results revealed in these chapters. This includes bridging the efforts to inform MSR strategies, presented in this dissertation, with near-future studies in development, planned to inform biogenicity protocols of samples returned from Mars.

CHAPTER 2

BIOSIGNATURE PRESERVATION POTENTIAL IN PLAYA EVAPORITES: IMPACTS OF DIAGENESIS AND IMPLICATIONS FOR MARS EXPLORATION

2.1. INTRODUCTION

2.1.1. Relevance to NASA's Priorities

NASA's 2011 Planetary Science Decadal Survey (NRC, 2011), the NASA Astrobiology Roadmap (Des Marais et al., 2008), the Mars Exploration Program Analysis Group (MEPAG, 2015), and the NASA Astrobiology Strategy (NASA, 2015) all emphasize two major priorities for Mars science: (1) Characterize aqueous, habitable environments and their biosignature preservation potential (BPP); and (2) identify biosignatures that can reveal whether Mars hosted life. To do this, specific recommendations have been made to address gaps in our understanding of preservation and habitability. They include studies to:

1. Develop integrated data sets by that will inform how to evaluate preservation potential in habitable environments;
2. Understand effects of chemical and physical conditions within aqueous reservoirs during environmental deposition;
3. Understand long-term preservation potential using terrestrial analogs; and
4. Compare modes of biosignature preservation over a range of habitable environments.

To address these recommendations, this study analyzed playa evaporite samples from a previously unstudied Mars analogue site in the Verde Formation, AZ. This study

was aimed at identifying evaporite subenvironments and comparing the impact of post-depositional processes (diagenesis) on preservation potential of microbial biosignatures.

2.1.2. Depositional Processes in Evaporitic Environments

On Earth, aqueous sedimentary lithologies with a high BPP include evaporite minerals, which precipitate from a brine when water evaporates. Evaporite formation is driven by the rate of solar evaporation and evaporite deposits retain microtextural evidence of the depositional process (Warren, 1999; 2006).

In the Verde Fm., evaporite deposition occurred under playa conditions. A playa is defined as a discharging intracontinental arid basin with a negative water balance, which remains dry 75% of the year (Biere, 2000). Within the upper millimeter to meter of the playa surface, there is often a capillary fringe where unconsolidated sediments are partially saturated with brine (Warren, 2016). A zone of saturation is overlain by a partially brine-filled capillary fringe that is drawn upward to the surface by capillary forces (surface tension effects) until the brine reaches the surface and evaporates, inducing mineral precipitation. Minerals grow displacively within the sediment, or are deposited as crusts and cements near the surface.

In the Verde Fm. playa sediments, gypsum grew displacively within porous, permeable playa muds and silts, just above the zone of saturation, driven by capillary evaporation of a $CaSO_4$-enriched brine. This type of growth forms "rosette" crystal aggregates (see Figure 1.17 in Warren, 1999; 2006 and Figure 2.2D), contrasted from bottom-nucleated gypsum growth, which forms characteristic "swallow-tail" gypsum crystals in a standing water column (Figure 1.16 in Warren 1999; 2006, and references

therein). Bottom-nucleated gypsum displays parallel-sided, prismatic, and twinned crystals (Warren, 1999). Schopf et al. (2012) found that bottom-nucleated gypsum effectively preserves organic matter and microfossils. Displacive growth gypsum (DGG) may also provide a favorable environment for preserving organic matter, but its preservation potential is understudied. This study was conducted to understand preservation in DGG and to compare it across the other playa evaporite subfacies in the locality.

2.1.3. Preservation Potential in Playa Environments

The long-term preservation of organic matter (OM) occurs under a narrow range of geological conditions involving accumulation in sediment, burial, and diagenesis, the post-depositional alteration processes (Allison and Briggs, 1991; Allison and Pye, 1994). Taphonomy is the study of processes that affect that the capture, preservation and post-burial alteration of fossil biosignatures, from the time of death of organisms, to the time they are exhumed for study (Allison and Briggs, 1991; Allison and Pye, 1994 and references therein).

In this section, the taphonomic factors relevant to preservation of OM in evaporitic playa lake environments are summarized. On Earth, only a few percent of the original OM produced by living systems survives post-depositional alteration after entering the rock record. Of the OM that is buried, ~80% is found as kerogen (Allison and Briggs, 1991), the degraded, macro-molecular fossilized OM found in aqueous sedimentary rocks. See Farmer and Des Marais (1999) for a general review of OM preservation.

Many environmental factors can affect the preservation of OM before it is buried. For example, the rapid deposition of sulfates can dilute the concentration of preserved OM, relative to inorganically deposited carbonate in surrounding mudstones (Warren, 1986; Katz et al., 1987). High concentrations of certain minerals, such as sulfates in brines, can enhance oxidation, thereby degrading labile organics (Katz et al., 1987).

Hypersaline evaporite environments enhance BPP because they have relatively low oxygen in surface and sediment pore waters (Powell, 1986; Warren, 1986 and references therein). Combinations of hypersalinity, high osmotic pressure, and anoxia can cause enhanced nutrient levels in the surface and subsurface pore waters, which can enhance BPP. It has been argued by some authors (Allison and Briggs, 1991; Farmer and Des Marais, 1999; Westall and Cavalazzi, 2011) that density-stratified water columns, such as hypersaline brines, increase bottom water anoxia, enhancing preservation. However, others (Katz et al., 1987) argue that stratification prolongs OM exposure to oxidation before reaching the anoxic bottom. In shallow saline lakes, preservation is thought to be enhanced because organics settle to the lake bottom faster, with shorter exposure to oxidation in the water column (Warren, 1986).

Once buried, OM continues to be affected by the sedimentary environment. The long-term preservation of OM depends on the degree of post-burial alteration during diagenesis, including compaction, lithification, dissolution, and replacement (Cady, 2001; Westall, 2008). In particular, recrystallization can reduce preservation potential, by the loss of primary microfabrics that could otherwise protect against OM oxidation (Allwood et al., 2009; Farmer, 1999). Burial by fine-grained, low permeability, and clay-rich sediment is known to enhance preservation (Farmer, 1995; Farmer, 1998; Farmer and

Des Marais, 1999; Westall and Cavalazzi, 2011). The presence of clays promotes preservation by binding organic molecules to charged mineral surfaces, or by incorporating them into interlayer sites (Farmer and Des Marais 1999 and references therein), especially in expansible smectite clays (i.e., Kennedy et al., 2002). Compaction of clays during early lithification reduces porosity and permeability. Compaction, combined with early and rapid diagenetic cementation, can create a closed chemical environment that promotes preservation (Allison and Pye, 1994).

2.1.4. Past Habitable Evaporite Environments on Mars

Both surface and orbital data from Mars have shown evidence for past habitable conditions, including lacustrine basins, and layered evaporite-rich, sedimentary sequences. For instance, ground-based data sets include those that have confirmed the presence of varied sulfates such as hydrated layered deposits with interbedded sulfate and phyllosilicate minerals as well as dehydrated Ca-sulfates, such as bassanite and anhydrite (Vaniman et al., 2014; Rapin et al., 2016). Hydrated Ca-sulfate (gypsum) has been found in a variety of Martian environments, such as displacive nodules (Nachon et al., 2014), in shallow playa-like settings (Glotch and Rogers, 2007), and in veins cutting sedimentary rocks (Squyres et al., 2012; Grotzinger et al., 2014; Rapin et al., 2016). Microscale textural features observed during *in situ* analysis have shown potential evidence of relict "hopper crystals" of halite (Squyres et al., 2006) and dissolved crystal molds of sulfates (McLennan et al., 2005).

The Mars Science Laboratory (MSL) rover is currently exploring a location in Gale Crater which observations suggest sustained ancient habitable environments with

high BPP. The central mound in Gale crater, Mt. Sharp (Aolis Mons), is interpreted to be a thick sedimentary section composed of phyllosilicate- and sulfate-rich sediments that likely formed in an alluvial fan/lacustrine setting (Cabrol et al., 1999; Milliken et al., 2010; Thomson et al., 2011; Grotzinger et al., 2015). To date, MSL has explored fluvio-lacustrine deposits exposed in the lower foothills of Mt. Sharp and on the Peace Vallis alluvial fan system (Grotzinger et al., 2014). Potentially habitable conditions are indicated by the discovery of smectite clays, (e.g., Mg-saponite) in the Sheepbed mudstone at Yellowknife Bay (Grotzinger et al., 2014; Vaniman et al., 2014). As MSL continues to explore Mt. Sharp's layered sedimentary record, further insights should be gained into the evolution of ancient habitable environments in Gale Crater.

The Verde Fm. playa evaporites are dominated by mudstones and siltstones that contain sulfate-rich zones with abundant displacive growth gypsum ($CaSO_4 \cdot 2H_2O$) and lenticular interbeds of halite (NaCl), thenardite (Na_2SO_4) and minor glauberite [$Na_2Ca(SO_4)_2$]. Areas of modern surface crusts that contain mirabilite ($Na_2SO_4 \cdot 10H_2O$), and minor limestone are also present (DeWitt et al., 2008). This study indicates that Verde Fm. evaporites represent a potentially valuable terrestrial analog for assessing the preservation potential of similar evaporitic environments on Mars (Farmer and Des Marais, 1999).

Evaporites are thought to be favorable environments for capturing and preserving fossil biosignatures. Halophilic microorganisms have not only been shown to preserve details of cellular morphology (Schopf et al., 2012), but may also exhibit prolonged viability following entombment in salt (Norton and Grant, 1988; Norton et al., 1993; Rothschild et al, 1994; Vreeland et al, 2000; Benison et al., 2008; Lowenstein et al.,

2011a). By extension, it is feasible that the evaporites described here can be preserved under similar conditions on Mars (Melvin, 1991; Richardson et al., 2009; Vitek et al., 2010; Lowenstein et al., 2011; Schopf et al., 2012; Winters et al., 2013).

2.1.5. Motivations for this Study

As new insights emerge about past habitable conditions in Gale Crater, it is important to go beyond simply "following the water," to a strategy of "following the preservation potential" (Farmer and Des Marais, 1999; Grotzinger, 2009). Understanding the taphonomic conditions and processes on Mars that may have enhanced BPP is a critical step in the search for life, since many factors can operate to reduce the long-term retention of OM after entombment in sediments (MEPAG, 2015; Summons et al., 2011; Farmer and Des Marais, 1999; Farmer, 1999).

Even if a Mars rover lands in an ancient habitable environment thought to have high BPP, competing priorities may complicate the choice of sampling targets. Present Mars analog studies that seek to define *in situ* sampling strategies for missions often do not consider complex conditions that can affect BPP - both *within* and *between* geologic environments. Additionally, the effects of diagenesis on long-term evaporite preservation potential, and how it varies between evaporite environments, are still understudied. This study of the Verde Fm. playa evaporites as Mars analogs highlights the complexity of evaporite diagenesis, and its potential effects on long-term preservation of organic matter in these environments. Such studies may inform future strategies for the astrobiological exploration of Mars and refine landing site and sampling strategies for Mars Sample Return (MSR), NASA's next phase of biosignature analyses on Mars. Samples cached

during NASA's next mission, Mars 2020, will potentially be brought back to earth for detailed biogenicity analysis. Therefore, caching the samples on Mars with the highest BPP may enable the success of finding any fossil life in samples returned to Earth.

2.1.6. Old Indian Salt Mine Historical Background

This study focuses on the late Miocene to early Pliocene Verde Fm., near Camp Verde, AZ. Historical documents indicate that this site has been actively mined for salts for more than two millennia. The Hohokam, Sinagua, and Yavapai Apache people inhabited the area (Wadell, 1972). The Sinagua people are thought to have used the site for burials and other spiritual purposes (Ayers, 1912). Early Native Americans are thought to have left behind numerous artifacts and even mummified bodies in and around the quarry site (Morris, 1928).

One of the earliest documented accounts of evaporites at the Old Indian Mine appeared in descriptions by Blake (1890). In the modern era, industrial thenardite mines have been established there, starting with Western Chemical Company in the 1920s (Morris, 1928), with industrial activities continuing into the 1960s. Today, the mine is inactive, but early quarrying operations have extensively exposed sedimentary units, providing access outcrops of the local stratigraphic section that is the focus of the present study.

2.1.7. Geological Context of the Study Site

The Verde Fm. was deposited within a continental basin that formed by crustal extension in the Transition Zone separating the Basin and Range structural province of

western North America and the Colorado Plateau province (Figure 2.1). The Verde Basin is one of several extensional sedimentary basins within the Transition Zone; it is bounded to the north by the Mogollon Rim and to the south by the Black Hills (Nations et al., 1981).

Sequences comprising the Verde Fm. record three primary depositional environments: (1) lacustrine, (2) marginal-lacustrine, and (3) alluvial fan (DeWitt et al., 2008). The lacustrine sequences of the Verde Fm. were deposited during the late Miocene to early Pliocene by episodic deposition of evaporite minerals under playa conditions (Nations et al., 1981; DeWitt et al., 2008). Deposition of the Verde Fm. occurred between ~7.5 - 2.5 Ma (Bressler and Butler, 1978 and references therein; Nations et al., 1981). This was followed by the formation of a perennial lake formed during the mid to late Pliocene (~5.3 – 2.3 Ma; Wadell, 1972). Widespread lacustrine sediments were deposited during this time, including well-bedded lacustrine limestones (both calcite and magnesite compositions). Lake levels underwent cyclical changes controlled in part by periodic damming of the Verde River by volcanic flows, as well as climatic and tectonic events (Donchin, 1983).

This study focuses on a sulfate-rich, calcareous playa mudstone sequence exposed in the Old Indian Salt Mine quarry along the southern edge of the Verde Basin in the Verde Fm. (Figure 2.1; Wadell, 1972). Figure 2.2 shows the depositional environments and subfacies sampled for this study.

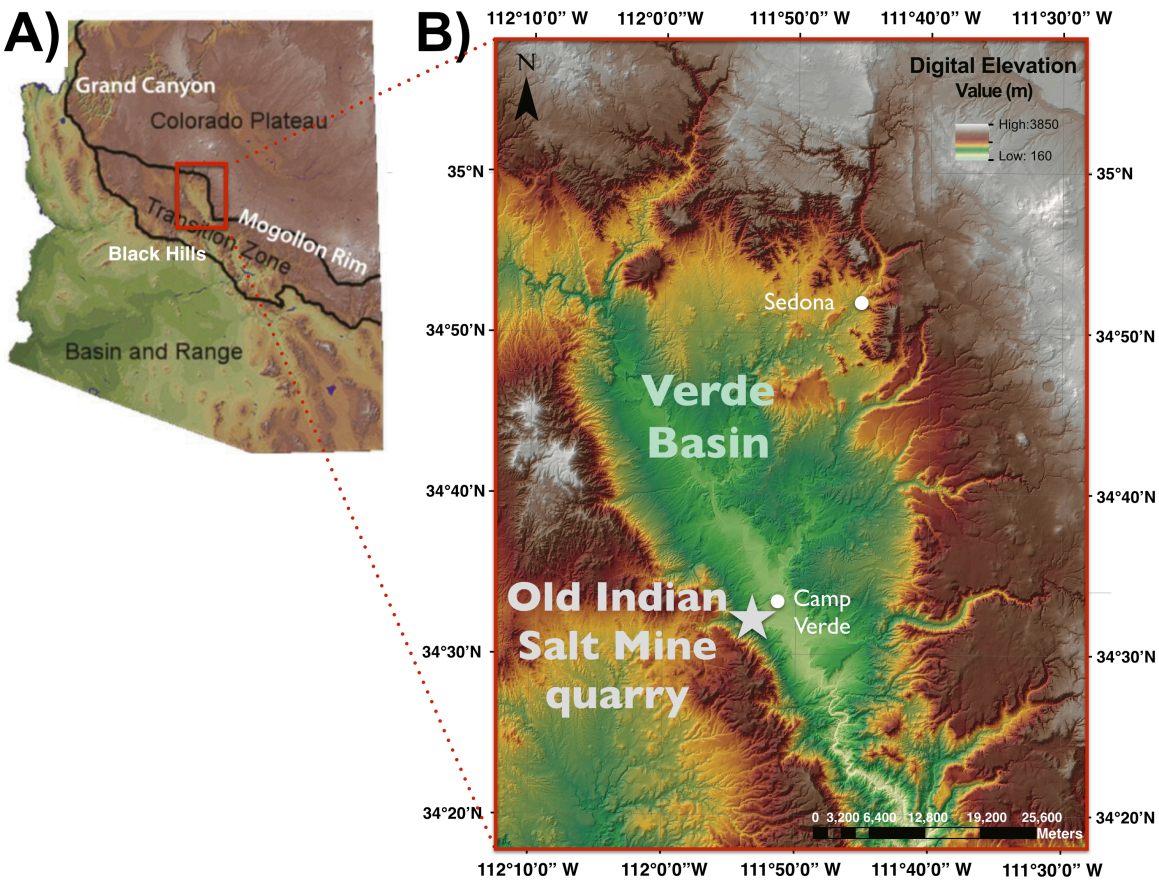

Figure 2.1. Geologic context of the Old Indian Salt Mine Quarry. (**A**) The Verde Basin lies within the transition zone of central AZ, between the Basin and Range Geologic Province and the Colorado Plateau Province. The Verde Basin lies within the red box in (A), magnified in (B). The map in (A) is reproduced from Ott (2014) with permission. (**B**) A magnified view of the area within the red box in (A) pinpoints the location of the Old Indian Salt Quarry (starred) within Verde Fm. near the town of Camp Verde. An early version of (B) is credited to Andrew Darling.

The diagenetic evolution of the Verde Fm. evaporites is inferred in the Results section, based on the model of Hardie and Eugster (1970) with modifications by Jankowski and Jacobson (1989). In this model, five major brine types were distinguished in evaporite basins: (1) Ca–Mg–Na–K–Cl; (2) Na–Ca–SO4–Cl_3; (3) Mg–Na–Ca–SO_4–Cl; (4) Na–CO_3–Cl; and (5) Na–CO_3–SO_4–Cl waters. One important deviation from the Hardie and Eugster (1970) model is that the present diagenetic model assumes a

hydrologically open, not closed, continental basin. (For a detailed review of continental basin hydrology, see Warren, 1986; 2010).

Working backwards from mineral assemblages sampled, it is assumed that brine chemistry can be traced to one of these starting brine types: the Mg–Na–Ca–SO_4–Cl brine type in the case of Verde Basin. With evaporation, dissolved ions increased in concentration, removing minerals from solution through precipitation. This brine type deposited a characteristic mineral suite, including halite, gypsum, and Na-sulfates. In the Results section, the present study integrates this model and sampled subfacies analyses to recreate the evolution of this basin, including the precipitation of Ca sulfates, including gypsum (displacive grown), and Na-rich and Cl-rich phases (thenardite and halite), and later stage Mg-carbonate cements.

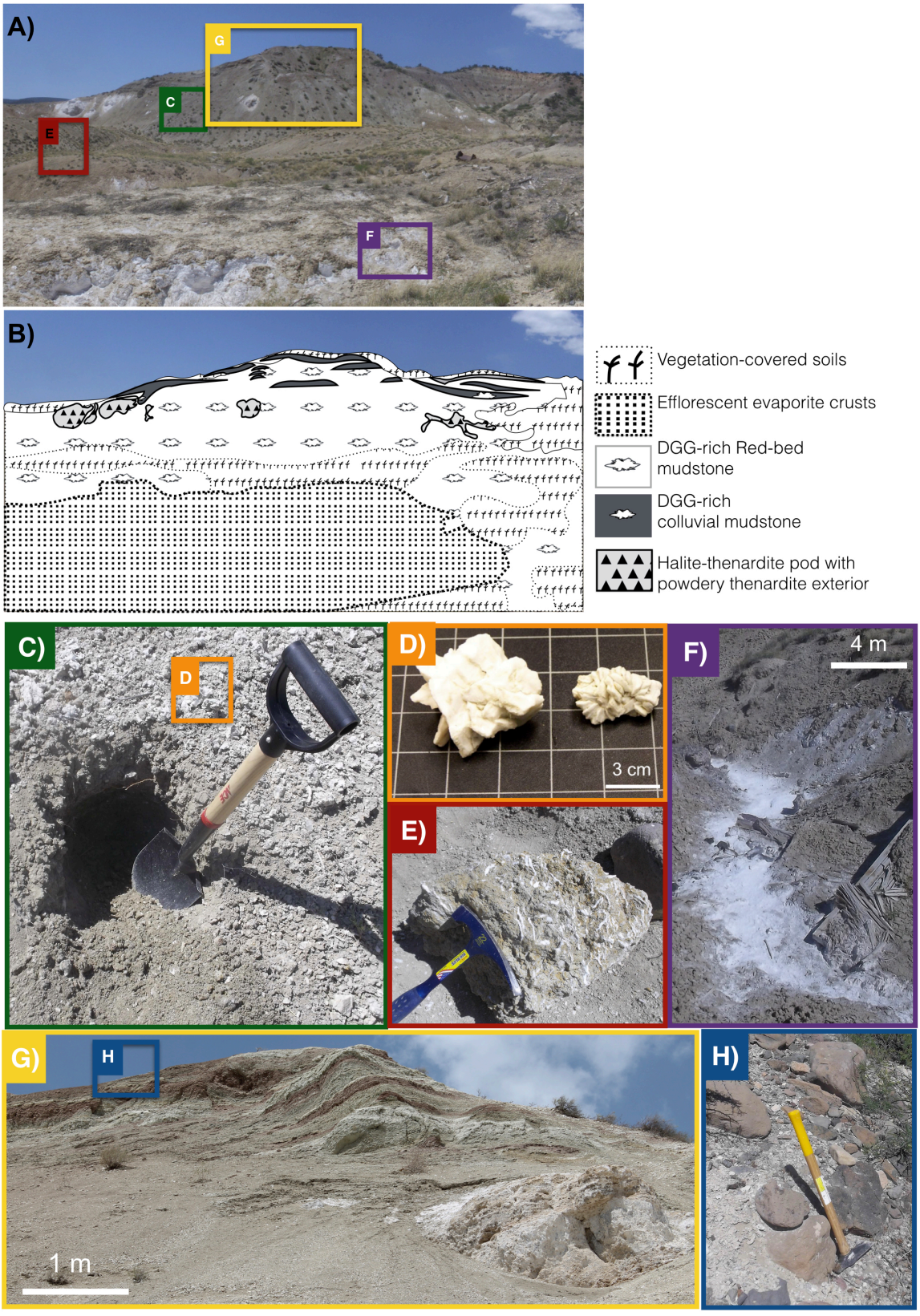

Figure 2.2. Sampled outcrop environments. (**A**) Panorama of the south quarry wall with

outcrop views of the boxed regions corresponding to images (**C**) – (**I**). (**B**) Main members of the quarry are shown in an outcrop map overlain onto (A). Main members include the following. Gray, magnesite-cemented colluvial playa gray mudstone is the dominant slope-forming unit of the quarry. This unit is overlain by interbedded gray and Fe-oxide cemented, red mudstone units (labeled "red mudstone" in B), visible at the top of the quarry, offset by meter-scale faults. These beds are overall lenticular and many thin out laterally. Both the gray and red mudstone units contain abundant displacive growth gypsum (DGG) crystal "rosettes". On the quarry floor, small streams cut channels by headward erosion. Dry channels banks and floors are covered by efflorescent crusts of Na-sulfates. Halite-thenardite pods are exposed on mid and upper slopes of the south quarry wall. The pods have irregular shapes and are visible as white, exteriors of powdery thenardite. Pods are aligned laterally on the slope of the quarry wall. Much of the quarry floor is covered by vegetation. Not visible in the quarry image in A is a thin capping gravel unit which overlays the playa sequence (see H). Some symbols are based on Warren (1999). (**C**) Quarry slopes are dominated by gray mudstone shown here, exposed after trenching to remove a surface layer of colluvium. Also visible are abundant clusters of white DGG, which have been concentrated on the surface of the colluvium by slope wash which removed sediment. Mudstone and associated clusters were sampled from various localities (see Table 2.1). (**D**) Close-up view of clean DGG rosettes. (**E**) Block of indurated, Fe-oxide-cemented mudstone from the upper quarry wall with sub-parallel gypsum crystal alignment. (**F**) White, powdery efflorescent crust, collected from the margins of a shallow bank that has incised the quarry floor. (**G**) SE-facing view of thinly bedded, Fe-oxide-rich mudstone collected from the upper quarry wall. Evidence was observed near the SW-facing hillslope (not shown) of minor faulting and irregular lenticular bedding that disrupted lateral continuity of beds. In the lower right corner, the halite-thenardite pod is visible below the redbed mudstone unit on the upper wall. See Figure 2.9 for additional pod outcrop images. (**H**) The unit capping the quarry hill is associated with well-rounded pebble to boulder-sized clasts of mafic volcanic and metamorphic rocks thought to be remnants of alluvial fan deposits laid down before the channel incision by the Verde River.

2.2. METHODS

2.2.1. Overview of Methods and Objectives

The goals of this study were to understand:

1. *What post-depositional, diagenetic processes affected Verde Fm. evaporites?*
2. *How did the documented diagenetic pathways in (1) affect the biosignature preservation potential (BPP) of each subfacies in the Verde Fm. evaporite system?*

The main body of this paper is organized as follows. In Section 2, our field sampling strategy is summarized, along with our data collection strategy from six different analyses, including: (1) thin-section petrography, to understand diagenetic processes and paragenesis; (2) X-ray powder diffraction, to obtain bulk mineralogy; (3) Raman spectroscopy, to identify and place mineral phases (and kerogen) within a microtextural context; (4) Total Organic Carbon (TOC) analyses to obtain weight percentage of preserved organic carbon for each subfacies, as a measure of BPP; (5) electron microprobe to characterize kerogen and minerals *in situ* for each subfacies; and (6) visible to near infrared reflectance (VNIR) spectroscopy, to confirm the identities of Fe-bearing phases. In Section 3, the results are reported and summarized for each subfacies, as well as for organic matter results (EPMA and TOC). There, this study's first goal is also addressed with a presentation an empirical model of diagenetic pathways in Verde Fm. evaporites. In Section 4, this study's second goal is addressed. Next, results are integrated for diagenetic pathways and TOC analyses to present a model of selective preservation of organic matter across diagenetic pathways in Verde Fm. evaporites. Limitations of the methods used and the importance of using multiple, complementary analyses when trying to understand BPP, are addressed. Finally, in Section 5, a synthesis of data and interpretations is provided, with implications for refining taphonomic models for BPP in evaporite environments, for analyzing BPP in similar systems on Mars, and for preparing for upcoming Mars biosignature missions.

2.2.2. Field Sampling

Field collection and photo-documentation of samples from major six different endmember environments occurred each April from 2014 to 2016. Outcrop-scale observations were combined with laboratory analyses of collected samples. See Table 2.1 for details.

Table 2.1

Verde Fm. Sample Collection Descriptions and Coordinates.

Sample #	Locality Description	GPS Coordinates	Image, Fig. 2.2
04232014.1	Surface gypsum clusters from mudstone exposed at the base of the slope of south quarry wall	34°32.754'; 111°52.575'	C, D
04232014.2	Crystals from a halite-then. block collected on the quarry floor where it fell from a halite-thenardite pod located within mudstone unit on quarry slope	34°32.701'; 111°52.620'	G
04232014.3	Thenardite–rich weathering rind occurring as a friable white powder collected from the exterior of sample #04232014.2	34°32.754'; 111°52.575'	NP
04232014.4	Block of coherent mudstone collected on the slope above the quarry floor (from layered sequence midslope on quarry hill)	34°32.546'; 111°52.876'	NP
04232014.5	Gypsum crystals collected from the interior of #04232014.4	34°32.546'; 111°52.876'	D
04232014.6	Thenardite–rich weathering rind occurring as a friable white powder on a block collected from halite-thenardite pod within mudstone unit on quarry slope	34°32.549'; 111°52.877'	NP
04232014.7	Vertically oriented halite and thenardite crystals in pod associated with sample #04232014.6	34°32.549'; 111°52.877'	NP
04232014.8	Indurated crystal from within mudstone-rich region of pod near sample #04232014.7	34°32.549'; 111°52.877'	NP
04232014.9	Efflorescent crust collected from the surface of the bank of a shallow creek on the quarry floor	34°32.757'; 111°52.541'	F
0423201.10	Efflorescent crust collected from mudstone-rich subsurface of the bank below sample #04232014.9	34°32.757'; 111°52.541'	F
04152015.11	Mudstone underlying colluvium from mid-slope on south quarry wall	34°32.703'; 111°52.616'	C
04152015.12	Loose, weathered gypsum clusters from #4152015.11 collected from colluvial surface materials deposited on indurated mudstone	34°32.703'; 111°52.616'	C, D
04152015.13	Single indurated crystal from halite-thenardite pod associated with samples #04232014.6 - 04232014.8	34°32.701'; 111°52.620'	NP
04152015.14	Loose gypsum clusters dug out from ~1 m deep surface colluvium, top of slope, south quarry wall	34°32.756'; 111°52.590'	D
04152015.15	Mudstone matrix from same region as #04152015.14	34°32.756'; 111°52.590'	NP
04152015.16	Fe-oxide cemented (red) mudstone at top of south quarry wall	34°32.756'; 111°52.590'	G
04152015.17	Fe-oxide coated gypsum crystals from sample #04152015.16	34°32.756'; 111°52.590'	NP
04152015.18	Loose block of Fe-oxide-rich mudstone originating from top red mudstone unit and collected from the eastern base of south quarry wall	N/A	NP
04152015.19	Fe oxide-cemented indurated mudstone containing gypsum crystals, originating from top red mudstone unit, collected at the base of the slope, where it fell from the upper quarry wall	N/A	E

Table 2.1. Representative field images of most samples are provided in Figure 2.2; the last column denotes their location in Figure 2.2. GPS coordinates are given as latitude (N); longitude (W). N/A indicates not available. NP indicates not pictured in Figure 2.2.

2.2.3. Petrographic Microscopy

To create spatially integrated data sets using microscopy and Raman spectroscopy analyses, petrographic thin section studies were carried out for each sample subfacies. Standard (30 μm-thick) petrographic thin sections and strew mounts (from powdered samples) were prepared by Spectrum Petrographics Inc. (www.petrography.com). Non-fluorescent thin section epoxy (EPOTEK 301 resin from Epoxy Technology) was used in preparing thin sections.

For light microscopy analyses, thin sections were analyzed using a Nikon Eclipse E600 POL polarizing microscope and an Optronix digital camera system. Major and minor mineral components were documented as photomicrographs using transmitted (plane- and cross-polarized) and reflected light illumination. Identifications of minerals and kerogen involved alternating between transmitted and reflected light illumination, comparing data for specific mineral and kerogen targets in thin section with compositional data acquired from spot analyses from Raman. Spatial relationships between minerals and fabric elements in thin sections were used to reconstruct diagenetic processes. Primary and secondary mineral components and cross-cutting spatial relationships, as well as microtextures, were used to reconstruct paragenetic events and to place them in a time-ordered sequence. Phases identified by microscopy were confirmed by other analyses (Table 2.2). This approach provided a framework for placing kerogen biosignatures within a paragenetic framework to better constrain its origin and preservation potential. This strategy also provided a framework for selecting specific spots for Raman analyses. To maintain a spatial context during analyses, colored markers

were adhered near representative kerogen and mineral grains on thin sections, allowing those spots to be reliably relocated for Raman spectroscopy analyses.

2.2.4. Raman Spectroscopy

A laboratory V-CW Raman spectroscopy system at ASU's Center for Solid State Science was used to obtain point spectra from uncovered thin sections. This micro-Raman system uses a 532 nm Coherent Sapphire SF laser source and a Princeton Instruments liquid nitrogen cooled CCD detector and Acton 300i spectrograph. A 1200 lines/mm grating was used with an acquisition window from 70–2000 cm^{-1}.

A built-in transmitted light microscope was used for relocating kerogen and mineral grains of interest that had been pre-labeled with markers during microscopy analyses (see above). The Raman laser spot (diameter, ≲5 μm) was manually focused on the sample surface. Spectra were acquired over a range of integration times, power settings, and depths below the surface of thin sections to obtain the optimal signal (i.e., spectrum with the least fluorescence and highest signal to noise ratio). Integration times ranged from 1-30 seconds, powers from 750 μW- 6 mW, and sampling depths from 1-20 μm. Powers were manually controlled using a neutral density filter wheel. Sampling depth was manually controlled by focusing the Raman laser spot (<5 μm diameter) on the sample surface.

Raman shift positions were calibrated using a cyclohexane standard. No background correction was applied. Mineral identifications were obtained using the *CrystalSleuth* software (Downs, 2006) and the associated RRUFF online reference database of minerals obtained using a 532 nm laser (Lafuente et al., 2015).

2.2.5. X-Ray Powder Diffraction (XRPD)

XRPD analyses were obtained from bulk, powdered samples to provide an independent assessment of mineralogy. (Note that kerogen cannot be identified using XRPD.) Bulk samples were crushed in a plattner mortar, ground to powder using a quartz mortar and pestle and sieved to a <150 μm fraction. A Siemens D5000 X-ray Diffractometer with a Ni-filtered Cu radiation source was used to identify minerals present in bulk samples. Sample powders were scanned from 5° to 81.759° with a step size of 0.016303º. Operating conditions were 40 kV at 30 mA using CuKα ($\lambda_{\alpha 1}$ = 1.5060 Å; $\lambda_{\alpha 2}$ = 1.54439 Å**)** with an 8-second dwell time, for a total analysis time of 12 hours per sample. Background subtraction and mineral identifications were performed using the *JADE*™ software, version 9 (Materials Data, Inc.), with the International Centre for Diffraction Data (ICDD) library reference database.

2.2.6. Electron Probe Microanalysis (EPMA)

For EPMA analyses, standard, doubly polished 1-inch rounds were obtained (Spectrum Petrographics, Inc.). Rounds were cleaned with compressed air and then coated with 0.6 nm of iridium.

Elemental analyses were performed using a JEOL JXA-8530F Electron Probe Microanalyzer at ASU's John M. Cowley Center for High Resolution Electron Microscopy. Elemental compositions were obtained as both point spectra and maps. Operating conditions included a 15 keV accelerating voltage, 20 nA beam current, 5 μm beam diameter, 50 ms dwell times, and 5-10 μm step size. C-rich epoxy can infiltrate porous mudstones during thin section preparation and mimic a false-positive kerogen

signal. Since Cl is found in epoxy but not kerogen, it was used as a kerogen anti-indicator. Dwell times for EPMA analyses were maximized for high Cl counts and minimized for beam-induced degradation. X-ray intensities (maps and point scans) were measured on C, O, Na, Mg, Al, S, Cl, and K intensities using energy-dispersive spectrometry (EDS) for all phase identifications.

2.2.7. VNIR Reflectance Spectroscopy

Visible to near infrared (0.35–2.5 μm) reflectance spectroscopy was performed on samples from the Fe-oxide cemented mudstones to identify iron-bearing phases. Hand samples and powders were prepared using the same methods used for XRPD. Spectra were acquired at ASU's SCORPIUN lab using an Analytical Spectral Devices (ASD Inc.) FieldSpec 3 spectroradiometer. Analyses were carried out at room temperature and under ambient atmospheric conditions. The Muglight option was used for powder measurements and a goniometer with mounted fiber optic cable and external light source was used for hand samples. Samples analyzed were ~1 cm in surface area. The Muglight had an internal light source fixed at a 23° incidence angle. The goniometer was set to an incidence angle of 30°. A Spectralon® 99% diffuse reflectance standard was used as a white reference. Spectral data were processed to units of absolute reflectance using the ASD ViewSpec software.

2.2.8. Total Organic Carbon (TOC) Analysis

Representative samples from each subfacies were powdered to 150 μm (as for XRPD analyses). Multiple rounds of silver capsule method *in situ* acidification, using 1

M hydrochloric acid, were performed to digest carbonate fractions. Dissolution continued until no effervescence was observed. Samples were left to fully dry in a desiccator between acidification rounds and before measurement.

Total organic carbon (TOC) analyses were performed in the W. M. Keck Foundation Biogeochemistry Laboratory at ASU using a Thermo Delta plus Advantage isotope ratio mass spectrometer, interfaced with a Costech Elemental Analyzer. In-house glycine standards as well as the NIST2710 standard were used for calibration and isotopic data normalization. To promote complete combustion, silver capsules were wrapped in tin capsules and combusted at 1020°C. TOC concentrations are reported as weight percent (wt %).

Two to five replicate samples were analyzed for each subfacies. When fewer than four replicates were used, it was because additional replicates showed evidence for evaporite formation on capsule exteriors during acidification. These replicates were discarded due to presumed loss of sample mass.

TOC and carbon isotopes were measured on the same samples to confirm that TOCs were derived from organic carbon and not from inorganic sources (which would imply incomplete digestion of carbonate). Carbon isotopes were expressed as per mil variation from the PDB reference standards.

Uncertainties for both TOC and isotopic measurements, Δ, were determined using:

$$\Delta = \sqrt{\mathrm{RSD}_{inst}{}^2 + \sigma_{rep}{}^2}$$

where RSD_{instr} is the relative standard deviation between measurements for a glycine standard (instrumental uncertainty), and σ_{rep} is the standard deviation between replicate measurements of a sampled subfacies (defined in Table 2.2).

2.3. RESULTS

Samples were studied using the analytical techniques discussed above. Results are reported in Table 2.2 for each of the five subfacies sampled, as identified in at the outcrop and detailed below.

Table 2.2

Mineral Phases Identified within Each Subfacies Analyzed

Phase		Subfacies					
		Gray Mudstone	**DGG**	**Red Mud-stone**	**Red DGG**	**Halite-Thenardite Pod**	**Efflorescent Crusts**
Carbonates	Magnesite	MXRE	MRX	MX		MXE	M
Chlorides	Halite					MXE	
Metal Oxides	Goethite	V		V	V		
	Hematite	MRV		V	V		
	Ilmenite			E			
	Lepidocrocite[3]	v					
	Rutile			E			
	Unidentified	M		E	E		
Phosphates	Apatite			E			
	Phosphosiderite					r	
Phyllosilicates	Montmorillonite	V	x	V			
	Muscovite	MRX		x			
	Saponite (Fe or Mg)	xV		V			
Silicates	Amphibole			E			
	Feldspars[4]	MRE		MRE	ME		
	Quartz	MREX		MREX			
	Titanite			E			
Sulfates	Anhydrite/Bassanite		MR				r[1]
	Celestine		r[1]		rE	MR[1]	R[1]
	Ferric sulfates		r[2]			x[2]	
	Glauberite		r[1]			MR	R[1]
	Gypsum	MRX	MRX	MRX	MRXV	MREx	Mr[1]X
	Thenardite		MRX			MR[1]XE	RX
Sulfides	Arzakite[5]	MR					

Table 2.2. It should be noted that DGG and red DGG are separated only in this table so their identified components can be tabulated. M = petrographic microscopy; R = Raman spectroscopy; X = XRPD; E = EPMA; and V = VNIR. Lower case letters indicate a weak feature.

[1]When appears between two related phases in the same subfacies, this denotes a cation-substituted intermediate phase.

[2]Nearby post-mine minerals (Vance and Condie, 1987) such as Kieserite group sulfates, rhomboclase, hexahydrite sulfates, or Lausenite (Lausen, 1928), were the best matches for otherwise ambiguous Raman and XRD data.

[3]Limonite is also possible.

[4]Detrital feldspars entrapped within mudstone components included alkali, Na-, K-, and Ca-rich subfacies endmembers.

[5]The presence of this uncommon sulfide is explainable by (1) the sodium chloride presence and elevated salinity of ancient brines in the lake and (2) the sulfide ore body that existed nearby in Jerome (Vance and Condie, 1987) or the Black Hills.

2.3.1. Mudstone Subfacies

The Verde Fm. playa deposits are dominanted by clay-rich and calcareous (rich in Ca-carbonate) mudstones. In outcrop, the mudstone is mostly a slope-forming, structureless unit. The lack of fine layering within the mudstone unit is likely a result of extensive haloturbation by displacive growth of sulfates (i.e., gypsum) within sediment and by the dissolution and precipitation of soluble evaporites during early diagenesis. (In saline playa muds, haloturbation is the mechanical rotation of primary textural features in sediments by cycles of halite growth, dissolution, and reprecipitation; Warren, 1999). Mudstone forms the host matrix for displacive growth gypsum and the halite-rich pod subfacies.

In thin sections, calcareous mudstones are predominantly a fine-grained, mudstone and siltstone, cemented by patchy micrite (microcrystalline calcite; Figure 2.3A). XRPD, EMPA, and Raman confirmed magnesite ($MgCO_3$) to be the main carbonate phase cementing mudstone samples, consistent with results of Wadell (1972), who previously mapped the Verde Fm. mudstone-evaporite unit.

Irregular, sub-rounded and rounded, feldspar-rich clasts (sand to fine sand size range) were sometimes seen throughout mudstones (Fig. 3B). These fine clasts included quartz, feldspars and grains with Fe-oxide coatings, interpreted to be weathering rinds on mafic grains formed (during transport or after deposition).

The composition of the alteration rinds seen on some fine sand grains in the mudstone subfacies was initially interpreted based on their color in thin sections as being due to concentrations of Fe-oxides. However, Raman analyses of the rinds were unable to identify any Fe phases due to high fluorescence. (The only Fe-bearing phase confirmed

by Raman was hematite; Table 2.2 and Figure 2.3G). Similarly, XRPD also failed to identify Fe-oxides, suggesting that they were either poorly ordered, or were present at an abundance below the instrument's ~5% detection limit. In contrast, VNIR analyses of bulk mudstones did confirm Fe phases, including varying abundances of hematite, goethite, lepidocrocite, and similar Fe-oxide phases and their mixtures (see Figure 2.4). See Discussion for formation details. Results are summarized in Table 2.2.

Fine, detrital silicates (Figure 2.3B-E) were also seen in thin sections, including phyllosilicates. Phyllosilicates were an abundant phase in the mudstone unit. Wadell (1972) found mainly montmorillinoid clays, as well as other mixed layer clays in his analyses of Verde Fm. mudstones. Using XRPD and VNIR analyses, montmorillonite was identified as an important mudstone component, as well as smectite (Fe- and Mg-rich saponite; Figure 2.4; Table 2.2). Both clays are part of the smectite group. Detrital micas, such as muscovite, were also identified as a minor component in thin section (Figure 2.3C).

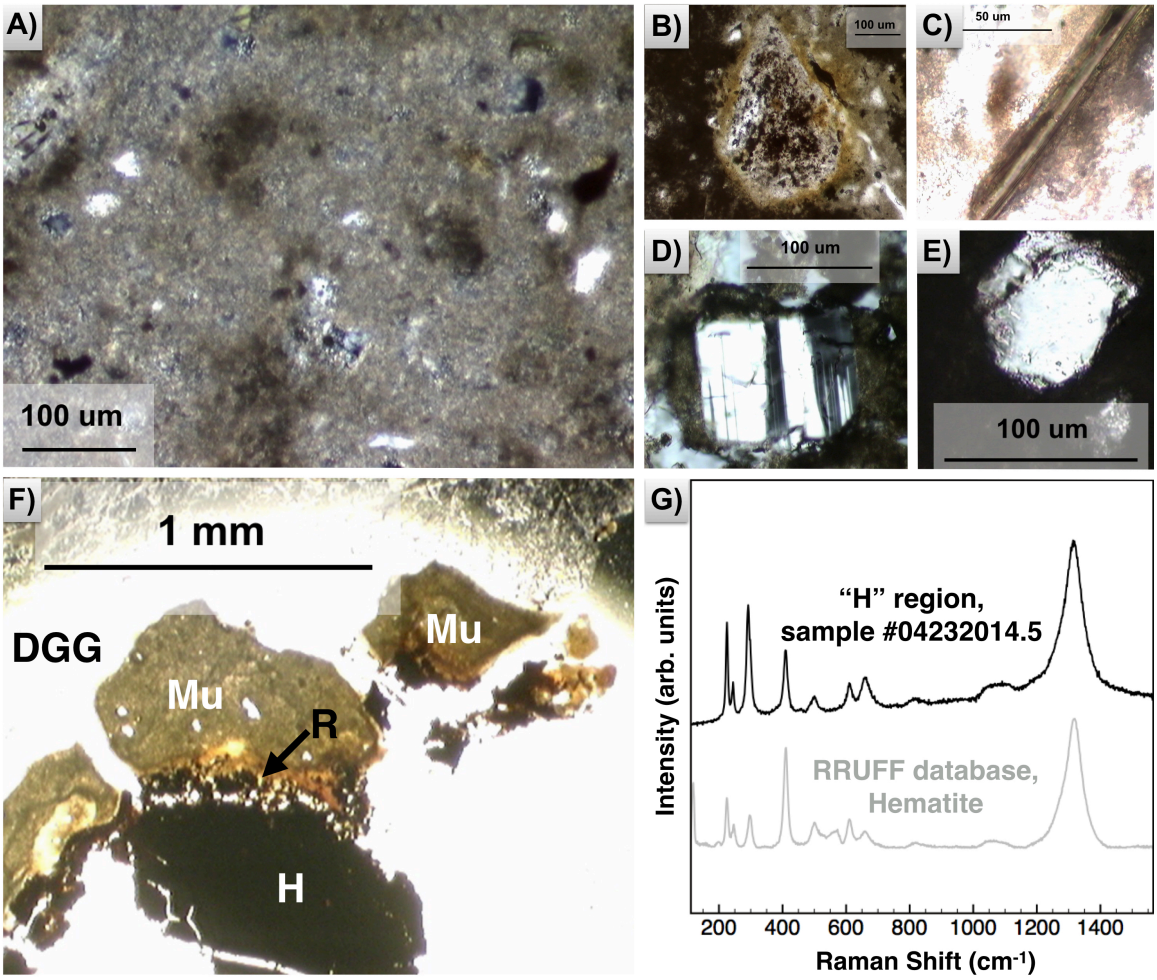

Figure 2.3. Mudstone subfacies. (**A**) Mudstones are composed of a mud matrix with lighter and coarser patches of cloudy micrite visible along with scattered detrital grains in plane-polarized light. (**B**) This plane-polarized photomicrograph shows an irregular clast within mudstone with a diffuse rust-colored alteration rim. (**C**) Large, platy micas were visible in mudstones in cross-polarized light. Coarse detrital grains were seen commonly under cross-polarized light, including (**D**) plagioclase feldspars, recognizable by their twinned patterns, and (**E**) quartz. (**F**) A rust-colored, diffuse rim ("R") is seen at the interface between mudstone ("Mu") and an opaque, rounded, fragmented hematite clast ("H"). The composition of the alteration rim remains unidentified but is likely Fe-rich. Broken chunks of this mudstone region and clast fragment are entrapped within a transparent DGG crystal. (**G**) Raman analyses confirmed the presence of hematite regions (such as that shown F) with spectral matches from the RRUFF database.

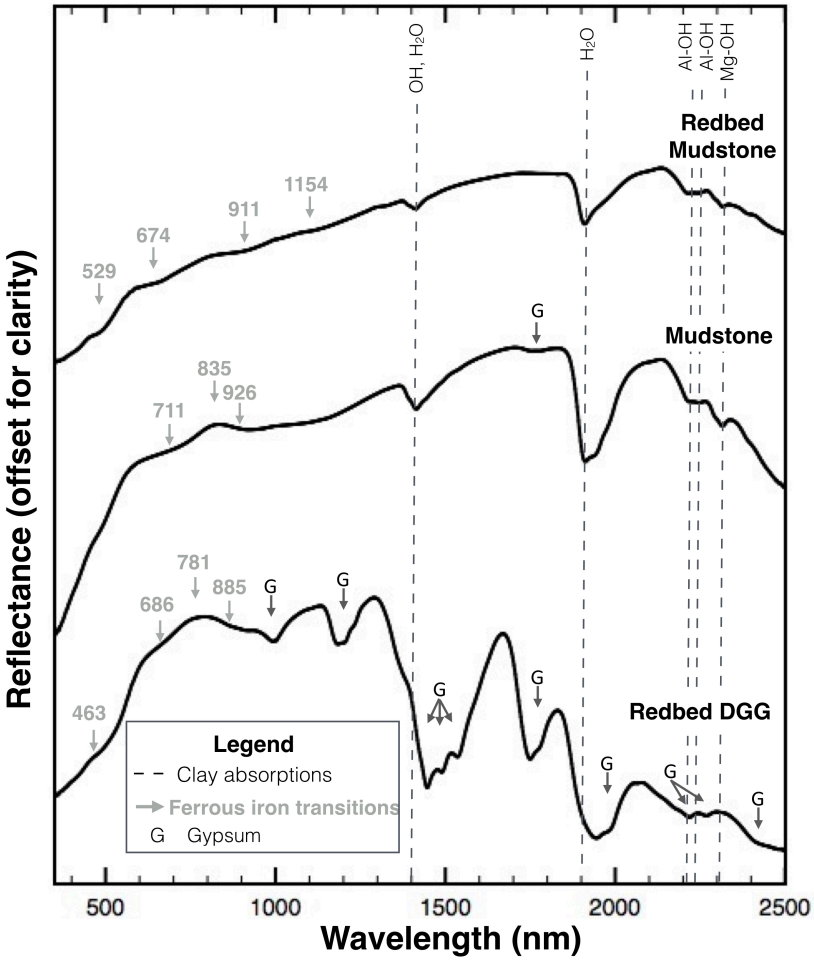

Figure 2.4. VNIR reflectance spectra. Spectra shown for powders of a red mudstone, #04152015.19, a gray mudstone, #04232014.5, and a hand sample of a red DGG, #04152015.17. Gray arrows indicate the absorption edge, shoulder, reflectivity maximum, or band minimum positions of identifiable Fe electronic transition features that are attributed to mixtures of hematite, goethite, lepidocrocite, or similar Fe- oxide phases (Morris et al., 1985; Cornell and Schwertmann, 2001). Dashed lines indicate montmorillonite and saponite clays at 1410 nm (OH, H_2O), 1920 nm (H_2O), 2210 nm (Al-OH), 2240 nm (Al-OH), and 2310 nm (Mg-OH; Clark et al., 1990; Bishop et al., 2008). The weak 1154 nm feature may be attributed to ferrous iron in saponite. "G" indicates a gypsum absorption feature (Clark et al, 1990). Spectra are stacked offset from one another for clarity.

2.3.2. DGG Subfacies

Displacive-growth gypsum (DGG) rosettes are another subfacies in the playa mudstone. These were collected at several localities along the lower south quarry wall

(Table 2.1). Clusters of sulfate crystals are abundant enough to form surface lags on the quarry slope, accumulating where surface runoff is channeled (Figure 2.2). Displacive growth forms crystal aggregates, as opposed to swallow-tail morphology formed by bottom-nucleated growth (see *Evaporite Environments and Preservation Potential* section).

All analyses of DGG crystal clusters were consistently gypsum-dominated (Table 2.2; Figure 2.4-2.6). Single crystals entrapped within mudstones often displayed well-developed lensoidal forms. Displacive growth of crystal clusters often resulted in the incorporation of the host mudstone and associated organic matter within the interiors of the crystal clusters (Figure 2.5B). Patchy textural coarsening of gypsum due to recrystallization was sometimes observed (Figure 2.5B). This occurred likely where diagenetic dissolution had occurred, leaving an external crystal cavities in the host mudstone (Figure 2.5C-D) followed by subsequent infilling of cavities by fine bladed gypsum crystals, and then by recrystallization that resulted in coarsening of the secondary, infilling phase (Figure 2.5E-F).

Raman spectroscopy point analyses collected on DGG and recrystallized gypsum commonly showed evidence for cation substitution through the detection of intermediate Na-Ca-Sr sulfates (Figure 2.6). Similar results indicating cation substitution in sulfates were obtained in analyses from halite-thenardite pod samples (Table 2.2).

Raman analyses also revealed that DGG was occasionally associated with a dehydrated Ca-sulfate intermediate between anhydrite, or $CaSO_4$, and bassanite, or $CaSO_4 \cdot 0.5(H_2O)$, but not completely matching the RRUFF database entries

(Lafuente et al., 2015) for either (Figure 2.6B). This is consistent with previous reports of anhydrite from mining operations at the nearby Graham Winfield Sulfate Ground (Phillips, 1987).

DGG aggregates were also sampled from red mudstone subfacies, interbedded with gray mudstones at the upper quarry (see section 2.3.3). These samples share many basic features with the gray mudstones with two exceptions. DGG samples from red mudstone units had Fe-oxide coatings on their exterior, attributed mostly to hematite (Figure 2.4; Table 2.2). In addition, EPMA and Raman analyses revealed Sr-cation substitution as well as total Sr-replacement (as celestine) as a minor component within gypsum domains in DGG crystals from the red mudstone unit. In contrast, within DGG crystals from gray mudstone units, only incomplete Sr-cation-substitution was observed (Figure 2.6-2.7; Table 2.2).

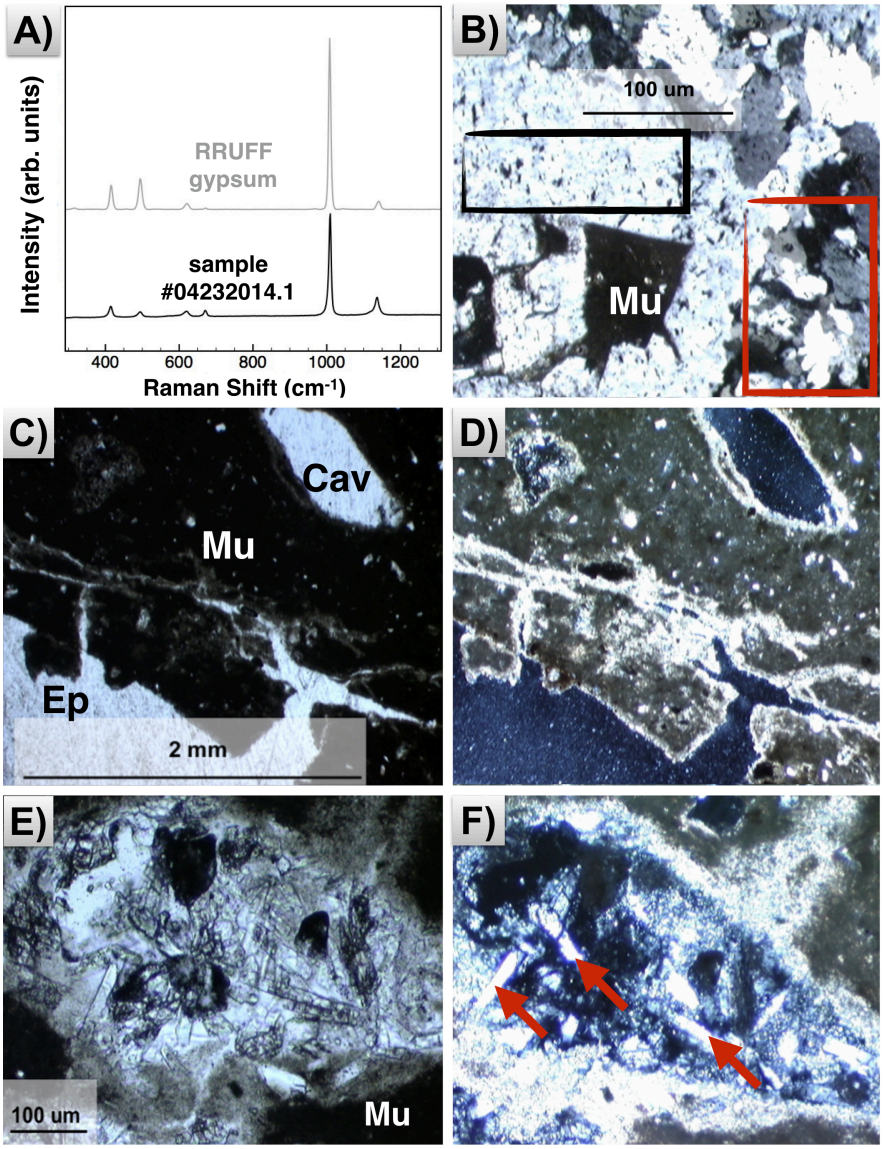

Figure 2.5. DGG subfacies components. (**A**) Gypsum Raman spectrum is shown for a DGG crystal (black spectrum) compared to a gypsum spectrum from the RRUFF Raman database (gray spectrum). (**B**) Cross-polarized photomicrograph showing mudstone ("Mu") trapped in a secondary gypsum crystal, which displays a recrystallization texture. Megacrystalline (black box) as well as microcrystalline (red box) gypsum domains are visible. Some cavities ("Cav") within mudstones appeared to have lensoidal forms, as seen in this (**C**) plane- and (**D**) cross-polarized photomicrograph of the same location. Some cavities were empty after dissolution and infilled with epoxy ("Ep") during thin section preparation. This is evident based on the epoxy region (the bottom left corner of thin section pictured) matched the optical properties of the cavity. Other cavities displayed complete cavity infilling, visible in (**E**) plane- and (**F**) cross-polarized light images. Extinction in (F) highlights the contrast between long, bladed recrystallized gypsum crystals, denoted with arrows.

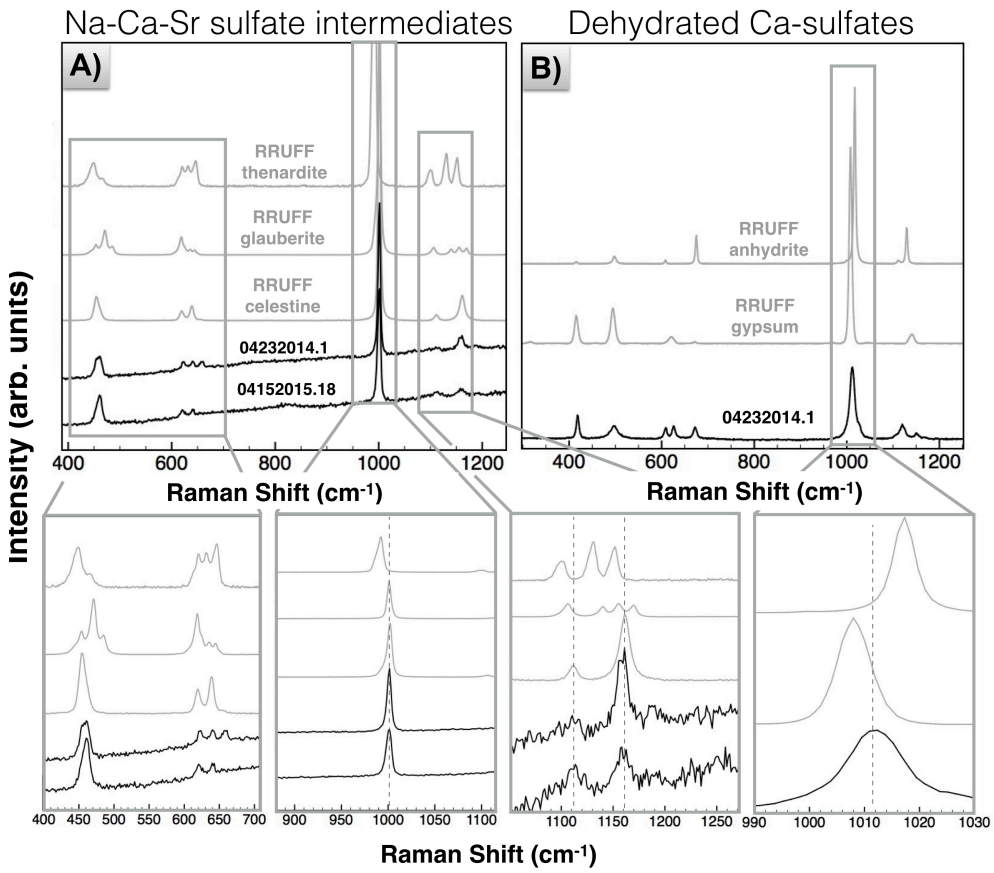

Figure 2.6. Raman spectroscopy in DGG samples. (**A**) Na-Sr-Ca intermediate sulfates are shown from a DGG crystal rosette from a gray mudstone unit (sample #04232014.1) and one from a red mudstone unit (#04152015.18). RRUFF database endmember matches are shown in gray for thenardite, glauberite, and celestine. In both spectra, the main sulfate vibrational mode (~1002 cm^{-1}) matches either glauberite or celestine. In spectrum 1, some vibrational bands (460, 621, 633, and 647 cm^{-1}) best match thenardite (Hamilton and Menzies, 2010) while others (1112, 1162 cm^{-1}) match celestine (Kloprogge et al., 2001). Spec. 2 best fits celestine. (**B**) An anhydrite-bassanite-gypsum intermediate Ca-sulfate is shown along with an inset magnifying the main sulfate vibrational mode (~1014 cm^{-1}), as compared to anhydrite and gypsum RRUFF database entries in gray. (No bassanite database standard was available.) Its sulfate anion vibrational band (~1014 cm^{-1}) and one cation band (628 cm^{-1}) are unique to bassanite, two are unique to anhydrite (498 and 608 cm^{-1}), while other cation bands (419, 673, and 1151 cm^{-1}) could be assigned to different combinations of the three Ca-sulfates (Prasad et al., 2001; Liu et al., 2009; Berenblut et al., 1973).

2.3.3. Fe-Rich Mudstone Subfacies

Samples were also obtained from a red mudstone subfacies, which occurs as interbeds with the gray mudstone at the top of the quarry (Figure 2.2G). Red mudstones include a silt-sized detrital component of silicates of igneous provenance, similar to the mudstone subfacies (Table 2.2). Silicate minerals present (i.e., feldspars) were associated with Fe-oxide alteration rinds, interpreted to be weathering products. VNIR reflectance spectroscopy of both the red and gray mudstones revealed the presence of similar Fe phases, including saponite (which was sometimes Fe-rich; Figure 2.4; Table 2.2).

Red mudstones differed from the gray mudstone samples in several ways. A pervasive Fe-oxide phase is present in red mudstones (in addition to the magnesite and fine-grained clay cements). The detrital component was enriched in volcanic clasts, especially Fe-rich phases, like ilmenite and biotite (Figure 2.7), which was not the case in gray mudstone samples. Detrital grains were coarser in the red mudstones (Figure 2.7B). Sand sized clasts present within red mudstones also contained fewer alteration rims as compared to those in gray mudstones (i.e., Figure 2.3B). This observed difference in the weathering of mafic silicate grains is somewhat at odds with the rusty red color of the unit, what appears to trace to a higher abundance of iron-rich cement caused by interactions with oxidizing fluids during diagenesis (see Discussion).

EPMA analyses revealed the presence of embayed Fe-oxides within the red mudstones (Figure 2.7E). However, it was unclear whether embayed grains were associated with alteration rinds in our analysis. These observations are consistent with an explanation that Fe-rich oxidizing fluids migrated through coarser and more permeable and porous muds, imparting a red color to the mudstones in the upper quarry (Figure

2.7F). This suggests that iron oxides formed as either a cement or as alteration products in the red mudstones.

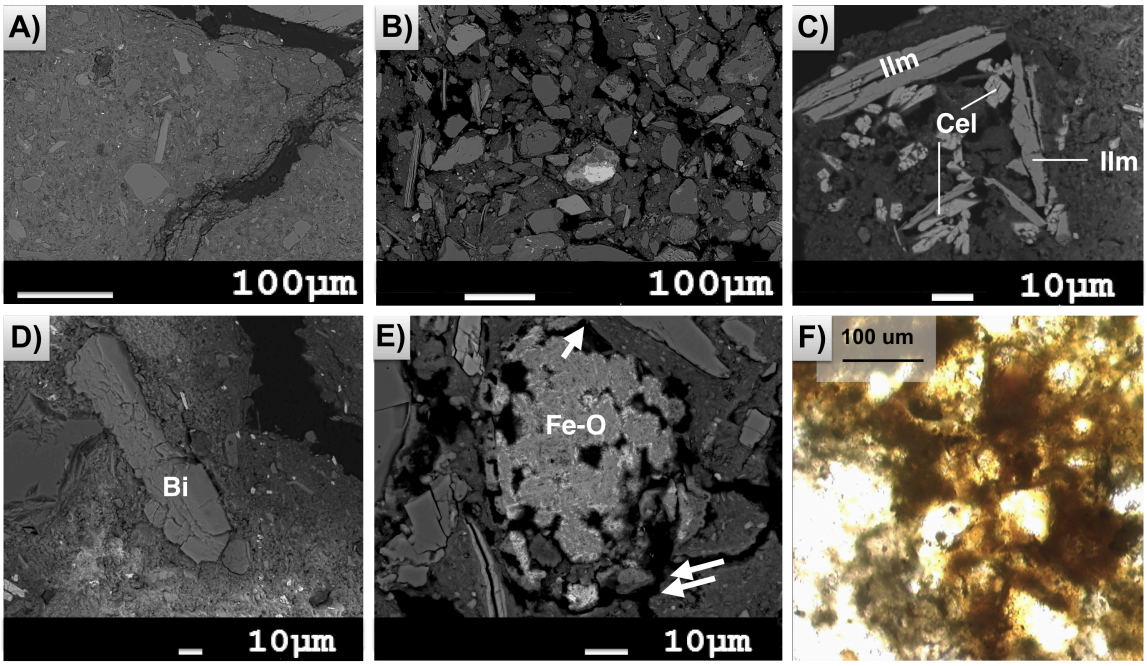

Figure 2.7. Red mudstone subfacies. When viewed at similar scales using EPMA backscattered electron mode, (**A**) sample #04232014.1, from a gray mudstone trapped within a DGG crystal, shows both finer grained and a lower abundance of fine sand silt-sized detrital grans as compared to (**B**) sample #04152015.19, from the red mudstone unit. Backscattered EPMA images are shown of (**C**) ilmenite ("Ilm," $FeTiO_3$) and celestine ("Cel," $SrSO_4$), as well as (**D**) abundant detrital biotite grains ("Bi," or $K(Mg,Fe)_3AlSi_3O_{10}(OH,F)_2$, all present in the red mudstone subfacies. (**E**) Fe-oxide grains sometimes occurred with features suggesting embayment, shown in the backscattered EPMA image pictured here. Arrows point out angular regions indicating the original grain boundary, interpreted as epoxy-filled molds (black regions) of the original grain. (**F**) Red mudstone samples contained "rusty" cements, seen in this plane-polarized photomicrograph of #04152015.19.

2.3.4. Halite-Thenardite Pod Subfacies

Samples were collected from lenticular beds ("pods") of halite, gypsum and thenardite at multiple sites along the south quarry wall, occurring as lenses within the gray mudstone (Table 2.1; Figure 2.2G). The pods represent a localized subfacies within

the gray mudstone subfacies based on outcrop observations suggesting that the white color, mineralogy, and pod–shaped geometry of these deposits was distinctive and localized.

Pods consist of interbedded halite and gypsum, surrounded by an outer zone consisting of thenardite and a thick, white, powdery surface coating (thenardite) on the surface (see below). XRPD and EPMA analyses indicated that all samples from pods were dominated by thenardite, halite, and minor gypsum. In thin sections, thenardite occurred as coarse-grained crystals containing cores of halite.

Halite was unconfirmed with Raman since it does not have Raman-active vibrational modes (Kieffer, 1979). However, in outcrops, pods halite-rich layers occurred as lenticular interbeds of bottom-nucleated, growth-aligned, cubic crystallites, consistent with halite (Figure 2.8-2.9). Similarly, thin sections showed textures dominated by interlocking subhedral to euhedral cubic grains (Figure 2.8B), consistent for halite. Halite domains were often visible as corroded domains within thenardite crystals (Figure 2.8C-D). EPMA confirmed the halite composition, with high Na and Cl (Figure 2.8E-F). EPMA results also eliminated concerns over Cl-rich epoxy contamination (Figure 2.8G).

Crystal growth within pods often entrapped the surrounding gray mudstone (Figure 2.8A). In outcrop observations (Figure 2.9), the general absence of mudstone matrix and subvertically-oriented gypsum crystals was consistent with bottom-nucleated growth. Bottom-nucleated gypsum was interbedded with bottom-nucleated halite (Figure 2.9).

Early literature frequently identified abundant glauberite in the Old Indian Mine locality as the dominant phase comprising the rosette crystal clusters found within

mudstone units (i.e., Twenter and Metzger, 1963; Anthony et al., 1982; Wadell, 1972; DeWitt et al., 2008). Contrary to these accounts, our study did not to identify glauberite as a replacement (i.e., pseudomorph) of the previously discussed DGG. Instead, glauberite was identified by microscopy and Raman spectral analyses in pod samples, where it occurs as a minor phase, specifically, as small crystals entrapped within larger, thenardite crysals (Table 2.2). Other sulfates similar to those described from the *DGG subfacies* were also detected in minor abundances within the halite-thenardite pod subfacies (Table 2.2).

The halite-thenardite pods displayed a thick, white, powdery surface coating. Strew mount thin sections from samples of this powder were dominated by thenardite. This coating is interpreted to be an alteration phase that formed by dissolution and reprecipitation of thenardite during surface weathering processes.

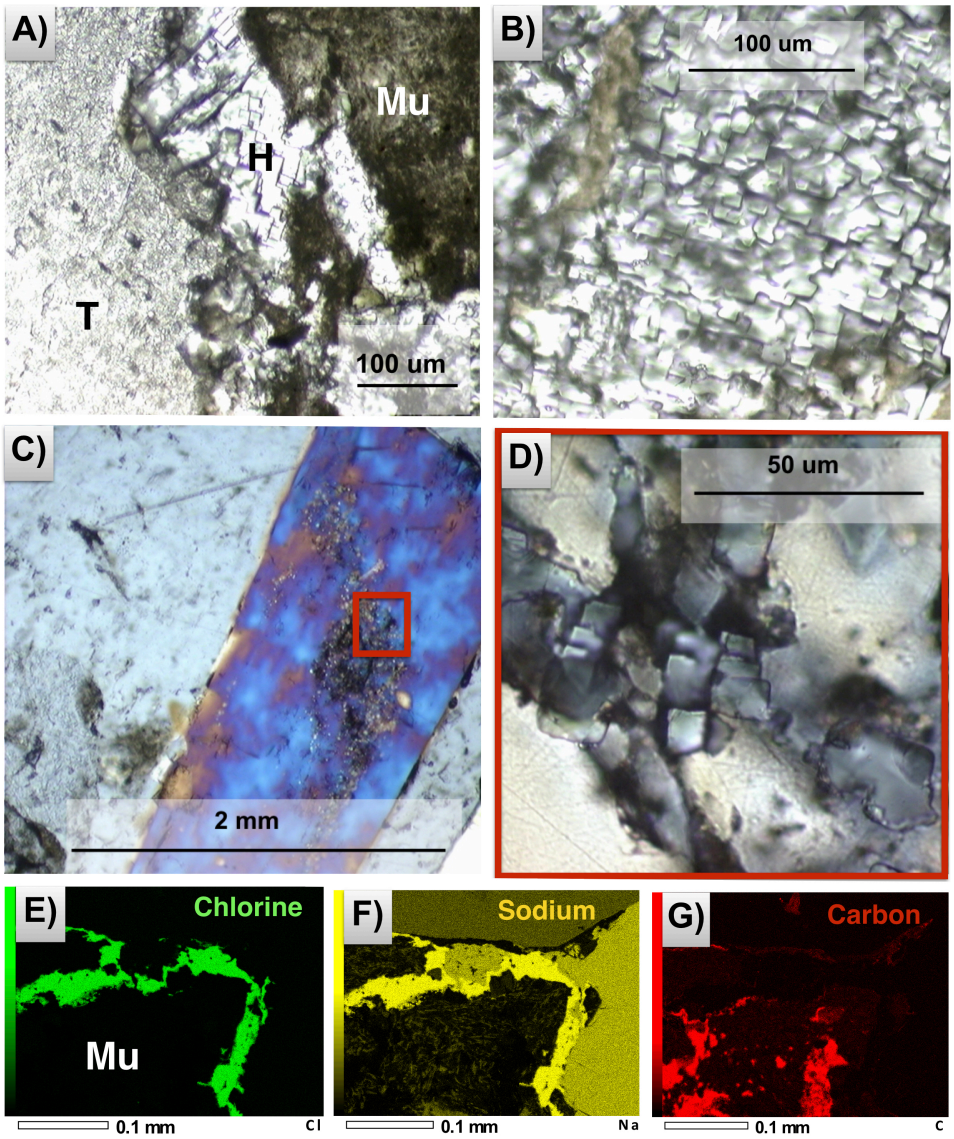

Figure 2.8. Halite-Thenardite pod subfacies. (**A**) Mudstones ("Mu") were seen surrounded by a halite ("H") border and embedded within a thenardite ("T") matrix, as seen in plane-polarized light. (**B**) Halite appears as subhedral to euhedral cubic crystals in a matrix of interlocking crystallites, as seen in this plane-polarized photomicrograph. **(C)** A thenardite photomicrograph is visible here in cross-polarized light, showing a large, angular thenardite crystal (appearing to have high blue birefringence colors) entrapped within a larger thenardite region (gray). The red boxed region is magnified in (D). **(D)** A domain of corroded replacement of halite is visible on the thenardite crystal shown in (C) in cross-polarized light. (**E-G**) EPMA EDS maps of a mudstone region confirmed the composition of halite. Surrounding mudstones, there was often a phase having abundant (E) chlorine and (F) sodium. (G) This region had low C, confirming that Cl-rich epoxy had not been misidentified as halite in other analyses.

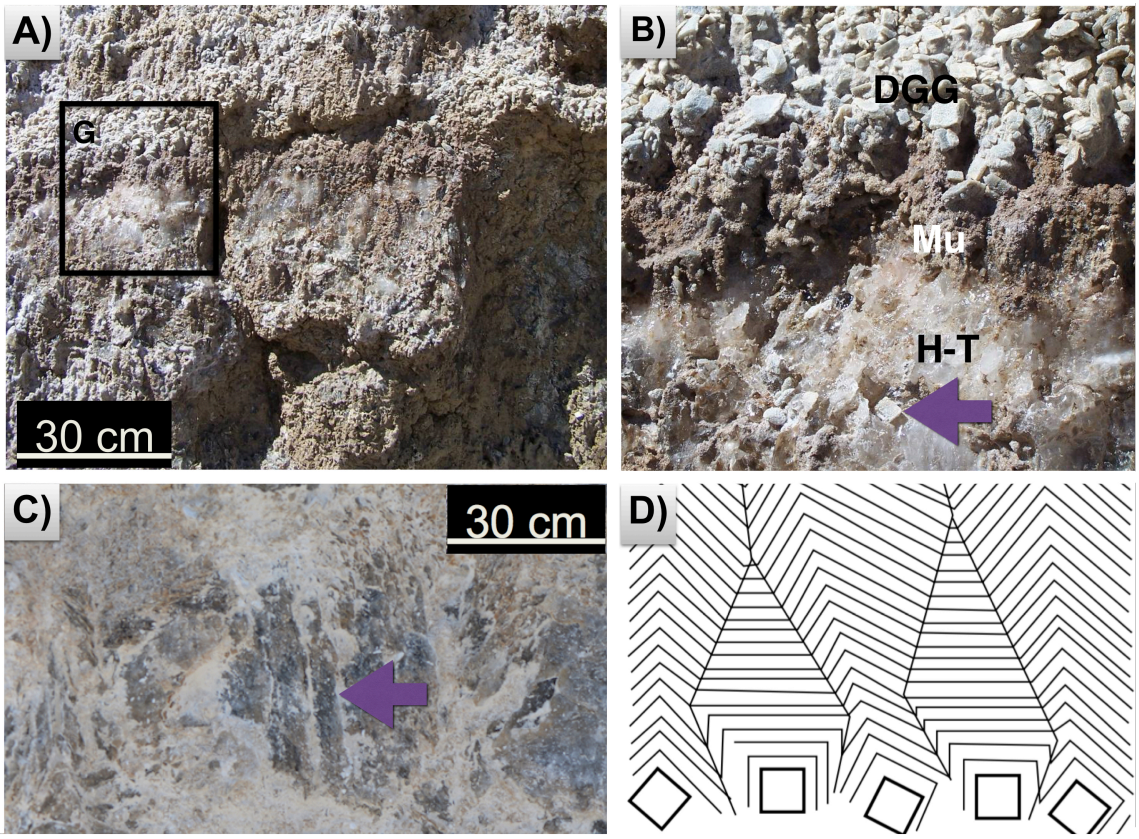

Figure 2.9. Pod outcrop images. **(A-B)** Outcrop observations of the pods revealed a matrix containing horizons of bottom-nucleated gypsum having undergone compaction and being interbedded with mudstone ("Mu") and halite-thenardite ("H-T") units. The box in (A) is magnified in (B). **(B)** The arrow points to a bottom-nucleated, growth-aligned, cubic halite crystallite. (**C**) Another example of bottom-nucleated, growth-aligned halite (arrow) is seen in the center of a halite-thenardite pod with powdery thenardite alteration visible on the surface. The features in (B) and (C) can be compared to the image in (**D**) from Warren (1999) illustrating typical bottom-nucleated halite chevron fabric in a salt crust.

2.3.5. Efflorescent Crust Subfacies

Samples were also collected from white, powdery, efflorescent crusts that had formed along the margins of a shallow channel that had incised the quarry floor (Figure 2.2F; Table 2.1). Microscopy and XRPD analyses of strew mount thin sections from these crusts revealed the presence of thenardite with minor contributions from gypsum (with evidence of cation substitution present, as well; Table 2.2).

Mirabilite has been documented in efflorescent crusts in the Verde Fm. evaporites (i.e., Wadell, 1972; Anthony et al., 1982; Phillips, 1987), but was not identified in our study, likely because of its instability. The chrysanthemum-like aggregates observed in strew mounts (Figure 2.10) imply that thenardite may have formed from dehydration of mirabilite (Tursina et al., 1980). Mirabilite is stable at cooler temperatures, but quickly dehydrates to thenardite, the more stable phase at warmer temperatures, either *in situ*, or in the lab, during thin section preparation.

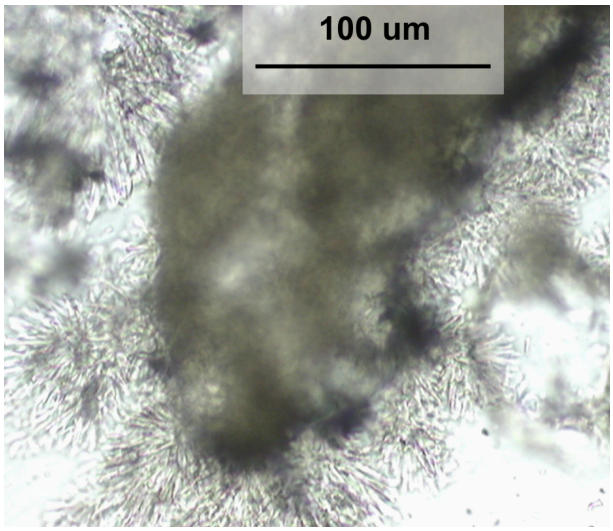

Figure 2.10. Efflorescent Crust Photomicrograph. This plane-polarized photomicrograph shows chrysanthemum-like thenardite aggregates visible around the mudstone (gray region in the center), consistent with mirabilite dehydration.

2.3.6. Organic Preservation

Many fossil occurrences have been documented in the Verde Fm. (Wadell, 1972; Nations et al., 1981; Donchin, 1983). However, Verde Fm. is generally unfossiliferous, except in the uppermost carbonate units where some fossils have been found (Wadell,

1972). This is consistent with our lack of morphological microfossil detections in thin sections and at the outcrop scale of the Verde evaporites.

Biosignatures in our samples occur as particulate kerogen, seen in thin sections as opaque, microscopic grains (10 - 100 μm) and in EPMA (Figure 2.11A). In our samples, kerogen was preserved exclusively within mudstones (Figure 2.11A). This was true even for the halite-thenardite and DGG subfacies, where kerogen-containing muds had been entrapped within the matrixes as they crystallized. EPMA results suggested kerogen based on elemental composition and confirmation that that epoxy was not falsely mimicking kerogen, showing that it was rich in C and O, low in Cl (Figure 2.11A-D), and low in all other elements.

Raman spectroscopy of the mudstone failed to provide useful organic detections due to fluorescence. For this reason, we resorted to bulk sample methods that were less resolved spatially, in order to obtain Total Organic Carbon (TOC) abundances for each subfacies. TOC results (Figure 2.11E) revealed that measurements clustered into two distinct groups. Mudstones and the modern efflorescent crust subfacies showed higher TOC values, while DGG and halite-thenardite pod subfacies showed similar, but lower values for TOCs.

All mudstones analyzed showed similar TOCs (0.11 ± 0.01 wt % average for gray mudstones; 0.14 ± 0.02 wt % average for red mudstones). This result is consistent with TOC values of <1% reported for near-surface, bioturbated evaporitic carbonate muds (Warren, 1986). Efflorescent crust TOC values were similar to the mudstones (0.16 ± 0.02 wt % average), despite their ephemeral nature.

The lowest TOCs in this study were obtained from the DGG clusters and the halite-thenardite pod samples. TOCs for DGG samples averaged 0.04 ± 0.04 wt %, while red mudstone DGG sample TOCs were 0.01 ± 0.02 wt % on average. The average DGG TOC values of all DGG TOC values fall into the lower TOC group, both in DGG samples collected from red and gray mudstone subfacies. TOC values for the DGG subfacies are consistent with those of Barbieri et al (2006), who obtained TOCs of <0.1wt %, using similar methods, for the organic-rich laminations of a lacustrine gypsum deposit in Tunisia. Halite-thenardite pod samples revealed TOC values comparable to those of gypsum: 0.04 ± 0.01 wt % on average.

Values for $\delta^{13}C_{org}$ ranged from -27.94 to -21.04‰ (VPDB) for all results (Figure 2.11E). Although exact input sources of the C_{org} are unknown, these $\delta^{13}C$ results are consistent with a biogenic origin. They are also consistent with the organisms that are commonly associated with lacustrine carbonates, including sedimentary organic matter, terrestrial OM, with the C3 carbon fixation pathway, lacustrine algae, as well as evaporite sediments rich in aquatic autotrophs in Miocene marls ($\delta^{13}C_{org}$ ranging from -15 to -35‰; Meyers, 1994; Des Marais, 2001; Schouten et al., 2001).

If $\delta^{13}C$ values were within the ranges expected for inorganic carbonates, they would invalidate organic C interpretations. The obtained $\delta^{13}C$ values are not consistent with an inorganic carbonate interpretation, whose values range from +12 to -15‰ for environments similar to those reported here (e.g., shallow lacustrine basins, hydrologically open and closed Miocene-aged lakes, and Miocene-age environments; hypersaline, playa lake carbonate-rich settings; Talbot, 1990; Bellanca et al., 1992; Utrilla et al., 1998; Aiello et al., 2001; Melezhik et al., 2001).

It is unclear why there is one outlier in both TOC and $\delta^{13}C$, in the DGG sample group (average TOC of 0.10 ± 0.04 wt % and $\delta^{13}C$ of -27.9 ± 1.87). It was one of two replicates of #04152015.14; Table 2.2. One possibility is that there may have been acid-organic or acid-sulfate interactions that skewed that data.

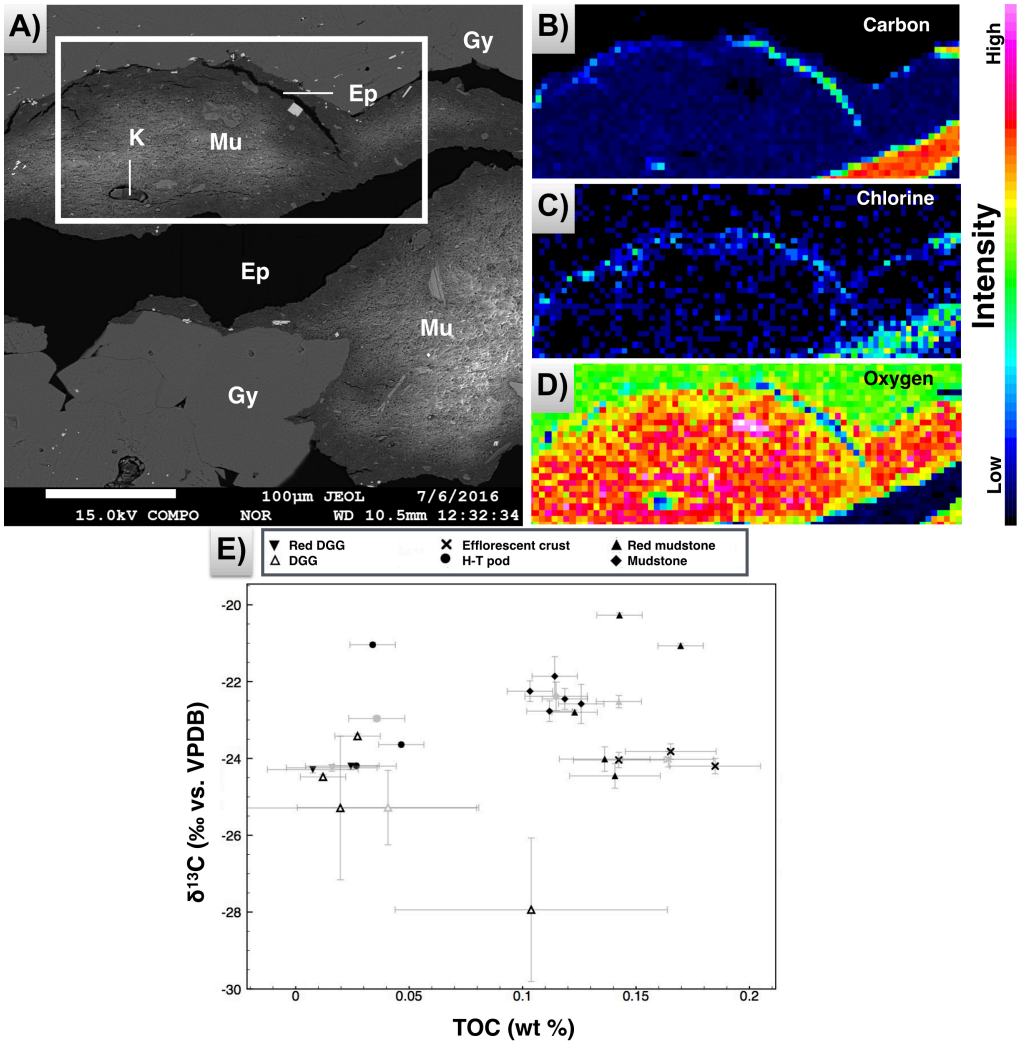

Figure 2.11. Organic analyses. (**A**) Kerogen ("K") was disseminated within fine-grained mudstone ("Mu"), shown in this backscattered electron mode EPMA image. Epoxy ("Ep") and gypsum ("Gy") regions are denoted. EDS elemental maps of the boxed region in (A) are shown for (**B**) carbon, (**C**) chlorine, and (**D**) oxygen, confirming that kerogen is distinguishable from epoxy by its low Cl abundance. (**E**) Plot showing $\delta^{13}C$ vs. TOC with associated uncertainties. Gray values represent the average values of each subfacies. For uncertainty calculations, see Methods. Abbreviations are as in previous figures and text.

2.3.7. Diagenetic Pathways in Verde Fm. Evaporites

Results and observations were integrated with models of basin brine evolution developed by previous researchers (Hardie and Eugster, 1970; Jankowski and Jacobson, 1989) to reconstruct an empirical model of playa evaporite diagenesis in Old Indian Salt Mine quarry. Addressing our study's first goal, our model outlines the four major pathways of diagenesis based on our analyses of the five main subfacies sampled (see sections 2.3.1- 2.3.5). Fig. 12 summarizes this model. In the Discussion section, the pathways model is integrated with TOC data as a proxy for BPP to infer a taphonomic model of selective preservation of organic matter across the diagenetic pathways recognized in the evaporite playa system.

Initial Depositional Environment

To provide a context for the diagenetic pathway model, it is first necessary to establish the initial depositional context of the playa environment (see Figure 2.12A).

After damming of the Verde River, the playa evaporites of Verde Basin formed from a continental basin with ionic proportions of Mg, Na, Ca, SO_4^{-2}, and Cl in parent waters (Hardie and Eugster, 1970). Mg and SO_4 may have been introduced into the system as a result of weathering of volcanic sources (Warren, 1999) or mafic rocks of Proterozoic basement in the Black Hills. During the late Miocene to early Pliocene, fine-grained, clay- to silt-sized muds and sediments were deposited onto ephemeral playas from distal alluvial fan sources from the south. It should be noted that in this study, the Verde Basin is assumed to have been an open basin, not hydrologically closed, as in the models by Hardie and Eugster (1970) and Jankowski and Jacobson (1989).

The abundant phyllosillicates seen in mudstones may have been transported to the playa surface by the alluvial fan system that developed along the southern basin margin during basin formation. Or, they may have formed authigenically during diagenesis. XRPD data could not confirm whether clays within mudstones originated authigenically or detritally, a dilemma also relevant to clays found recently in Martian mudstones (Bristow et al., 2015 and references therein). However, petrographic observations revealed the widespread distribution of detrital mica grains (Figure 2.5C) that were poorly sorted, and angular, as well as unweathered silicate minerals in mudstones, which experienced limited grain rounding during transport or alteration after deposition. These observations suggest that a detrital origin was likely the dominant origin for clays present in mudstones. This is consistent with the conclusions of Wadell (1972) that clays and gravels were transported into the basin from nearby alluvial sources.

Detrital carbonate deposition in such environments is common, but evidence for this was not observed our in thin section analyses. (Carbonate paragenesis is detailed in Pathway C0.)

Pathway A0: DGG Crystallization within Muds

DGG was the primary sulfate to precipitate within muds, consistent with the findings of Wadell (1972). Early DGG within muds characterizes Pathway A0. DGG formed by capillary-driven evaporation of $CaSO_4$-enriched bottom sediments in the restricted hypersaline environment after evaporative processes formed concentrated brines that accumulated below playa surfaces and above the zone of saturation. Gypsum

nucleation on organic substrates could have played a role in the cluster growth (Warren, 1999 and refs therein).

Pathway A1-A5: Later Stage DGG Alteration

DGG was altered in four processes, Pathways A1-A5 (Figure 2.12B). The lenticular form of the gypsum crystals (Figure 2.5) indicates that they crystallized in shallow brine pans subject to periodic short-term dissolution and regeneration (Warren, 1999 and refs therein). In Pathway A1, during periods of lower salinity, DGG experienced partial or full dissolution, leaving behind external crystal cavities in the host mudstone (Figure 2.5). Pathway A2 represents cavities that were partially infilled with secondary bladed gypsum crystals (Figure 2.5). In other cases, represented by Pathway A3, gypsum cavities were fully filled by secondary gypsum, which then recrystallized to form a mosaic of replacing crystals (Figure 2.5). In Pathway A4, gypsum may have experienced dehydration (Figure 2.6). This would be expected to occur when gypsum dehydrated at burial temperatures of ~35°C, shallow depths, and with a pore-fluid salinity of halite saturation (Warren, 1999).

Diagenesis can create cation-replaced domains within gypsum (e.g., Sr-rich gypsum; Kasprzyk, 2013). Pathway A5 shows Na-Ca-Sr cation-substitution (Figure 2.6). Data shows that Sr-substitution proceeded toward celestine in some cases, but the pure celestine endmember was only confirmed in DGG samples from the red mudstones (Figure 2.6A; Table 2.2). Celestine in red mudstones could have resulted when Sr-rich brines later came into contact with the dissolution fluids and secondary recrystallization of the primary sulfate, gypsum. The Na-Ca sulfate endmember, glauberite, was also

observed in some pod samples but not in DGG gypsum clusters, possibly as a replacement phase (Table 2.2; see Pathway B1).

Pathway A5, Na-Ca-Sr cation-substitution, was discovered with Raman analyses. Previous known analyses of Ca- and Na-sulfates with Raman have reported only rare cation substitutions (e.g., Dharmasena and Frech, 1993), implying that the general effects of cation substitutions on Raman-based sulfate phase identification need additional study. Systematic studies of this topic (as exemplified by the carbonate analyses of Rividi et al., 2010) are particularly important, especially for the range of sulfates that have been identified as present on Mars. Such studies could significantly increase the reliability in Raman database phase matching and the use of cation substitutions as paleoenvironmental proxies (i.e., Donovan and Rose, 1992; Baker and Bloomer, 1988; Butler, 1973). Such work might also provide additional insights into diagenetic impacts on BPP.

It remains unclear if Pathways A1-A5 occurred concurrently with other pathways, or were time-independent (represented as occurring at the same time interval, Time 1, in Figure 2.12B). This is because the sulfate phases and their alteration pathways described in our study were observed in association with all subfacies (Table 2.2).

Pathway B0: Halite Pod Formation

Ca consumption by gypsum would have led to the progressive enrichment of Na and Cl in ponded brines, with major contributions from Na, Mg, and Ca (Jankowski and Jacobson, 1989). Pathway B0 is characterized by halite precipitation within localized brine ponds, visible today as exposed pods at midslope elevations on the quarry wall

(Figure 2.2). Halite pods are and semi-aligned laterally, suggesting that their formation occurred midway during the stratigraphic time sequence preserved in the quarry walls. Pods tend to be elongated vertically (perpendicular to bedding), suggesting that they persisted over time, creating a vertically elongated geometry in the outcrop.

Based on outcrop observations and textural relationships visible in thin sections, halite pod formation is attributed to local karstification of older evaporites within the host gray mudstone through subsurface dissolution of soluble salts. This would have occurred during the circulation of supersaturated pore waters. Bottom-nucleated halite and gypsum growth occurred in localized brine-filled depressions on the playa surface.

Several observations lead to the conclusion that haloturbation was likely widespread during playa deposition and diagenesis. Periodic depositional events often on playas lay down fine beds or laminations. Depositional layering can be destroyed during dissolution and precipitation of salts on the playa surface between events where freshwater floods the playa surface and subsequently evaporates. The absence of primary lamination in the playa mudstones suggests extensive haloturbation occurred within the playa sediments. Such processes may also account for the irregular bedding seen in the pods. During halite precipitation and recycling, clasts observed within mudstones (Figure 2.3B) may have become deformed after diagenetic burial of evaporite beds were flushed by under-saturated subsurface waters (Warren, 1999 and references therein). These features were likely to be associated with haloturbation since they often originate from lithologies overlying or entrained within dissolving salt beds.

It remains unconstrained when pods formed with respect to Pathway A0. (This is represented as occurring at the same time interval as that pathway in Figure 2.12B.)

Pathway B1: Na-Sulfate Replacement

After halite precipitation, Ca, Cl, and alkalinity depletion of brines can cause molar Mg and SO_4 to became abundant relative to other cations (Jankowski and Jacobson, 1989). In the case of Verde Fm. evaporites, it is possible that when Mg concentration exceeded SO_4 concentration, neutral C1-SO_4 brines, along with Na and Mg (the major cations present) dominated brines, leading to the precipitation of Na-sulfates, which characterizes Pathway B1.

The main Na-sulfate present in the pods, thenardite, is thought to have formed after halite, since halite is always included within thenardite crystals in thin sections of pod samples and also in the outcrop where exposed thenardite rims are always external to halite-gypsum pods. In pods, thenardite formation is attributed halite replacement. This is based on thin section petrography showing an abundance of thenardite crystals with corroded replacements of halite domains in pod samples (Figure 2.8C-D). Thenardite is unlikely to have formed as a pseudomorph after halite; textures expected from such processes were not observed.

Cyclical evaporation of the lake to near dryness could have deposited small amounts of other Na-rich phases (i.e., glauberite, mirabilite) within the deepest parts of the basin (Wadell, 1972). Mirabilite reportedly appears during cooler seasons in efflorescent crusts (Figure 2.2; Wadell, 1972) but was not found in our samples. Crusts sampled in this study were thenardite-rich and likely formed by evaporation-driven precipitation of salts when complete dehydration of subsurface brine was drawn to the surface by capillary action (Warren, 2010). Efflorescent crusts were likely haloturbated and recycled throughout the quarry, both in the past and at present.

Pathway C0: Magnesite Cementation of Playa Sediments

During the Pleistocene, an extensive phase of lake formation occurred, depositing perennial lacustrine carbonates in the basin (Donchin, 1983). Burial, basin filling, and carbonate sedimentation occurred during basin flooding, as circulation of freshwater persisted (Donchin, 1983), characterizing Pathway C0. Primary sedimentary structures are likely to have been continually disrupted by haloturbation.

Carbonate present abundantly in mudstones, plus its texture and characteristics in thin section observations, suggests pervasive cementation by magnesite. Carbonate cements lithified into the magnesite-rich mudstone cement. The source for carbonates, whether detritally from limestone sources from nearby distal alluvial fans as carbonate muds, or authigenic, remains unconstrained. No evidence for detrital carbonates was observed in thin sections.

Pathway D0: Fe-rich Oxidation

During the playa period of the Verde Basin, a system of prograding alluvial fans developed along the southern margin of the basin, delivering fine-grained detrital silicate-rich sediments from the Black Hills in the south. During the last stage of playa history, alluvial fan channels began to prograde over the playa mudstones, depositing gravels on top of the fine-grained playa sediments. This is preserved as a pebbly conglomerate unit at the top of the quarry section (Figure 2.2) that contains metamorphic and volcanic clasts. These alluvial gravels were deposited unconformably on the top of the playa sequence in the red mudstone unit (Figure 2.7).

A change in depositional conditions is apparent as a shift from gray mudstones to interbedded gray and red mudstones at upper quarry (Figure 2.2G). The red color is attributed to the cementation of the red playa mudstones by Fe-oxides. This unit records a late stage diagenetic event that marks a shift in pore fluid compositions to oxidizing conditions, characterizing Pathway D0. The interbedded nature of red and gray mudstones (Figure 2.2G) implies that the environmental change from more reducing conditions (in gray mudstones) to more oxidizing Fe-oxide pore fluids (in red mudstones) was cyclic.

The red mudstones were likely coarser (Figure 2.7) and slightly more permeable, providing favorable conditions of the entry of oxidizing surface water. Oxidizing fluids could have been sourced from alluvial fan run-off to the playa surface and downward percolation into playa sediments.

Chemical weathering by oxygen-rich groundwater interaction may have produced authigenic Fe-oxides seen in samples (Figure 2.4; i.e., hematite, goethite, etc.) and possibly clays, as well. The presence of both weathered (e.g., alteration rims developed on some Fe-rich clasts) and unaltered (e.g., coarser angular grains) detrital materials seen in mudstones, along with the presence of Fe-oxide cements, implies that Fe oxidation occurred during transport to the playa and/or *in situ* within sediments, following deposition. Similarly, oxidation of mafic silicates formed Fe-rich alteration rims during or after transport, and *in situ*.

Cross-cutting relationships in thin sections of the red mudstone subfacies indicate that Fe-oxide cementation post-dated the displacive growth of gypsum in the red mudstones, since DGG aggregates in red mudstone units are always coated with red Fe-

oxide cements. However, the exact timing of Fe cementation remains unclear. The alternation of the two mudstone subfacies also implies that F oxidation overlapped in time with selective cementation dominated by Fe-oxides in the red mudstone subfacies and by magnesite in gray mudstone subfacies.

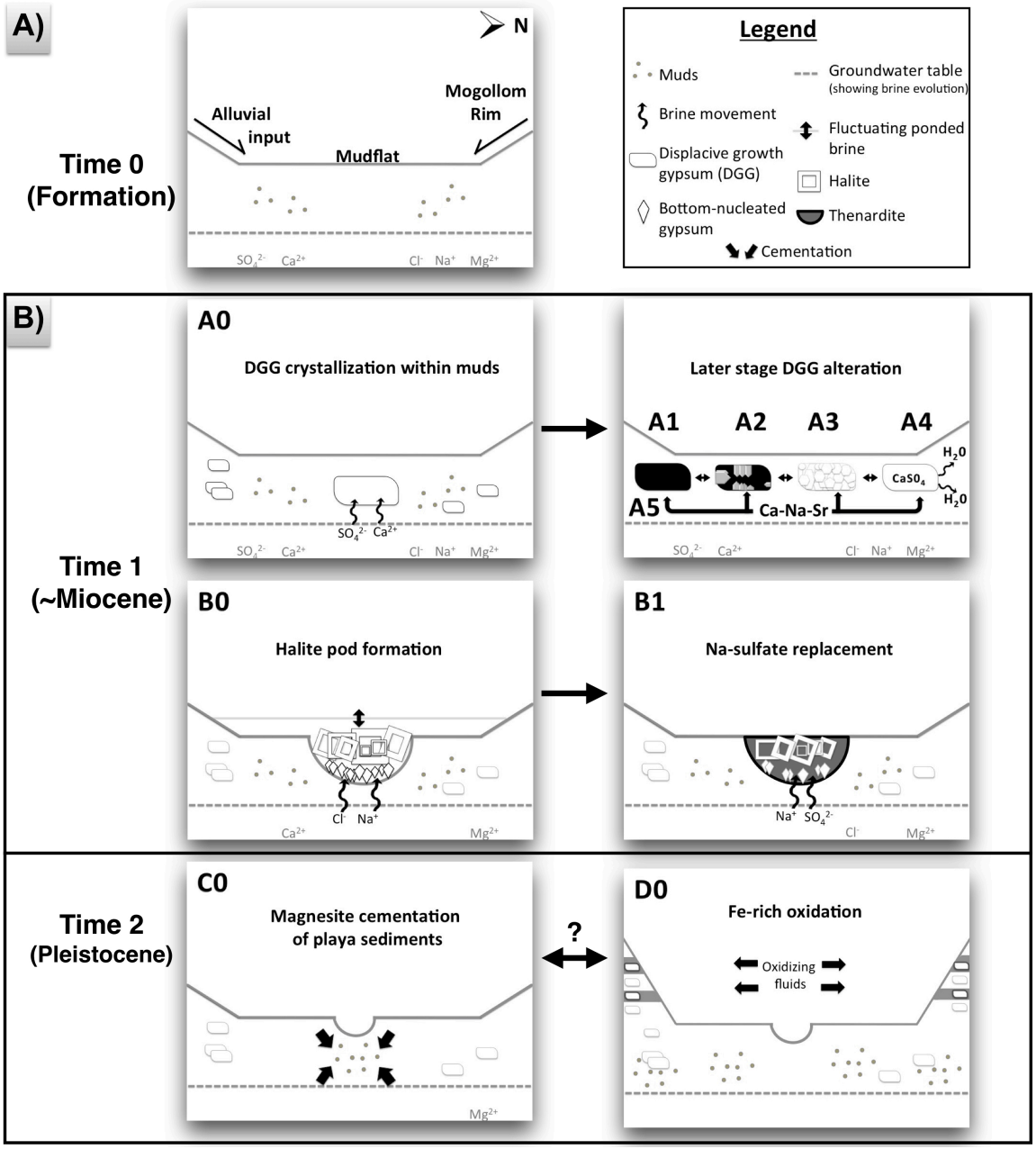

Figure 2.12. Model of diagenetic pathways through time in Verde Fm. playa evaporites. See Discussion text for description. **(A)** A diagram of the initial depositional playa environment is shown for context, hence it begins at Time 0. A legend is also shown. **(B)** A simplified illustration of inferred diagenetic pathways is shown and arranged through progressing time and diagenesis. The four major diagenetic pathways events are denoted A0-D0. Numbers after letters denote later pathway alteration events associated with those of the same letter. Pathways A0 and B0 may have co-occurred. The timing of Pathways C0 and D0 remains unconstrained.

2.4. DISCUSSION

2.4.1. Diagenetic Pathways Model

In this study, five diverse subfacies in the Old Indian Salt Mine quarry were sampled and empirically observed, and a diagenetic model for Verde Fm. evaporites was inferred. This model is an open basin and considers hydrologic conditions which changed during lacustrine conditions in the later history of the Verde Basin. Despite these two factors, our diagenetic sequence is consistent with the predictions from Hardie and Eugster (1970) and Janowski and Jacobson (1989), whose models predict the brine evolution of a Mg–Na–Ca–SO_4–Cl brine type in a closed hydrological system. This adds to the confidence of the model presented (and previously reported in Shkolyar and Farmer, 2015; 2016).

2.4.2. Taphonomic Model of BPP across Diagenetic Pathways

The Salt Mine playa evaporite outcrop studied here was expected to have high BPP for the reasons addressed in section 1. This study identified five subfacies within the Verde Fm. playa sequence and documented TOC abundances in subfacies studied, as proxies for kerogen abundance, based on the assumption that TOC can be used as a reliable indicator of BPP. Although a few studies (i.e., Wadell, 1972; Donchin, 1983) have documented diagenetic processes at several Verde Fm. localities, ours is the first study to present an integrated view of diagenesis (summarized in Figure 2.12) across the five subfacies recognized, and previously reported in Shkolyar and Farmer (2015; 2016). This information was used to create the first known taphonomic model for long-term BPP in the Verde Fm. evaporites, addressing this study's second goal.

The earliest stage of biosignature capture and highest BPP in relationship is inferred to have occurred in the earliest depositional phase of the playa. The starting TOCs of the Verde playa system cannot be directly measured as the samples collected represent later diagenetic stages in the history of the playa deposits. However, similar modern environments can provide a starting proxy for the TOC values, and by extension, BPP, expected for this system. Modern saline and hypersaline sediments, marine carbonate-rich evaporites, and hypersaline evaporative facies of freshwater, and suboxic environments are all known to have TOCs between 0.2 – ~30 wt % (Warren, 1986 and references therein; Carroll and Bohacs, 2001; Schreiber et al, 2001), up to three orders of magnitude higher than the mudstone TOC values reported here. Thus, this range of TOC values can be taken as an approximated starting point for the system studied.

The five subfacies sampled in our study represent two regimes of BPP based on TOC data: highest in mudstone subfacies, and lower in the DGG and halite-thenardite pod subfacies. (Efflorescent crusts are excluded from this preservation model because they are expected to have low TOCs and by extension, low BPP, due to constant recycling and haloturbation of evaporite surface layers. However, their TOC values were comparable to mudstone values. This is interpreted to be due not to fossil biosignature preservation but rather their association with underlying mudstone, contamination from abundant surrounding vegetation, as shown in Figure 2.2, or a more active biota accompanied by less complete diagenetic degradation as compared to the ancient deposits.)

Mudstone subfacies had the highest BPP as compared to all of the evaporite salts. Three factors explain the high BPP of the mudstone subfacies. The potential of

clays to trap and preserve organics is well known (e.g., Farmer and Des Marais, 1999). This is especially true for smectites (Kennedy et al., 2002), which all of our mudstones contained in significant abundances (as montmorillonite and saponite; see Table 2.2). In addition, fine-grained carbonate cementation was pervasive in the playa. If mudstones underwent early burial and lithification, entombed OM could have been protected against degradation. Burial by fine-grained, low permeability, and clay-rich sediments is known to enhance preservation (Farmer, 1995; Farmer, 1998; Farmer and Des Marais, 1999; Westall and Cavalazzi, 2011), especially in carbonate-rich sediments, since they are among the most common lithotypes for the Precambrian microfossil record (Farmer and Des Marais, 1999). On the other hand, disruption by halite recycling (i.e., haloturbation) and by living mobile microorganisms (i.e., bioturbation) altered primary muds before cementation and likely reduced what was an initially higher BPP (inferred based on modern analog TOCs discussed above) and relative to the modern, diagenetically altered mudstones sampled.

Fe-rich oxidation did not affect mudstone BPP. Fe-oxidation, pervasive in red mudstones, was expected to reduce BPP (Allison and Briggs, 1991; Farmer and Des Marais, 1999; Westall and Cavalazzi, 2011) relative to gray mudstones. However, results showed that TOCs of both mudstones were similar. Perhaps Fe oxidizing fluids were not abundant, or did not come into contact with the deposits prior to their cementation, which could have protected organic matter from oxidation. The timing of Fe-oxide cementation during red mudstone diagenesis, in relationship to carbonate cementation, remains unconstrained in our model.

DGG and halite-thenardite pod subfacies exhibited similar and low BPPs compared to mudstones. The DGG subfacies sampled represent the present, ongoing evolution following multiple diagenetic events (Pathways A1-A5). During the displacive precipitation of gypsum, host muds (and associated organics) were captured inside gypsum and halite crystals. The pathways that followed (A2-A4) likely reduced the BPP of DGG and halite-thenardite pods relative to host mudstones. During these pathways, secondary gypsum recrystallization could have reduced BPP (Allwood et al., 2009; Farmer, 1999). During Pathway A4, partial or complete dehydration could have reduced BPP, since dewatering of gypsum can flush out organic films (Warren, 1986). During Pathway A5, diagenetic fluids could have flushed out and possibly oxidized previously captured OM and preserved it in early DGG, when Na or Sr cations were exchanged. The causes of low BPPs in DGG subfacies sampled from both red mudstone and the unoxidized, gray mudstone are likely similar, since Fe-oxide cementation post-dated displacive growth of gypsum in the red mudstones.

In the case of the halite-thenardite pods, when ponded brines reached halite saturation, natural waters must have approached anaerobic conditions (Warren, 1999). Bottom-nucleated halite formed in shallow brine ponds. Both factors should have enhanced initial BPP within pods. However, any OM entombed in halite likely did not remain well preserved during repeated cycles of dissolution and re-precipitation of halite. Unsurprisingly, BPP was found to be low (with respect to mudstones) and similar in the halite-thenardite pod subfacies and DGG subfacies. The lower TOC values in DGG and halite-thenardite pod samples are consistent with observations by Katz et al. (1987). Many studies cite saline evaporite basins with high BPP (Powell, 1986; Warren, 1986,

and references therein). However, Katz et al. (1987) are among the few researchers to recognize that evaporite subfacies rarely yield higher OM quantities when compared to their associated claystone and carbonate members, for three reasons: (1) Density contrast between hypersaline brines and suspended OM retards its settling rate and prolongs its exposure to oxidation; (2) Concentrated brines and diagenetic fluids support oxidizers that can degrade labile organics; (3) Rapid rates of evaporite precipitation may dilute OM which reaches the sediment-water interface. It is concluded that the low BPP of both the DGG and pod subfacies was caused by a combination of localized brine-rich environments, oxidizing fluids, and constant recycling of evaporites present within pore spaces of muds and in shallow ponded environments.

2.4.3. Limitations of Methods

Carbon isotope values alone should not be taken at face value when examining biogenicity (i.e., Summons and Hallman, 2014). They are bulk measurements, which do not represent an *in situ*, non-destructive way of characterizing BPP. In our study, for instance, it is unknown how preservation of early DGG compares to altered, secondary DGG. That is because protocols for TOC and EMPA analyses do not allow the isolation of cation-exchanged or dehydrated domains within bulk samples. Instead, BPP trends revealed in our TOC data represents the BPP of the bulk DGG subfacies, averaged between all Pathways (B-B5). Microscale, nondestructive analyses may be the best way to define BPP, as per the recommendations of the astrobiology and Mars communities (i.e., Des Marais et al., 2008; MEPAG, 2015).

Consistent with these recommendations, an EPMA method was investigated to quantify BPP across subfacies *in situ*, at a microscale, and nondestructively. This method could have entailed making 2D carbon elemental maps of regions containing kerogen across all samples. A pixel-counting algorithm was created (in MATLAB) to calculate an area of kerogen coverage based on elemental carbon intensities. The carbon-bearing areas in all maps within one subfacies could be statistically averaged, defining a "preservation coefficient" within that subfacies. This coefficient could then be used to quantify BPP across subfacies.

However, many limitations prevented this protocol from being implemented within the scope of the present study. Issues that needed to be addressed included: (1) difficulties finding acquisition settings that provide an acceptable trade-off between sample damage (which could volatilize carbon using high energy X-rays and therefore reduce its intensity in carbon maps); (2) acceptable resolution; (3) challenges obtaining proper carbon standards (epoxy could not be used since its composition was not homogenous and other carbon standards were unable to be Ir-coated); and (4) sampling issues (i.e., manually targeting 2D regions may not be representative of the sample volume; and kerogen properties were not consistent across samples, etc.). Further studies are recommended to develop more robust, quantifiable, and nondestructive methods for examining BPP in analog samples considered high-priority targets for MSR.

A final limitation in this study is related to assumptions made in the diagenetic pathway model. This model did not consider whether groundwater flow occurred through the evaporite deposits after the sequence described here, and if so, whether evaporite units were re-buried or flooded. This hypothesis could be further tested with Sr isotope

studies, which may provide proxies for different environmental conditions during deposition or diagenesis and aid in environmental reconstruction. Cations in solution have been shown to influence brine composition, evaporation pathways, flow characteristics of groundwater, the permeability of sediments, and the precipitation sequence of evaporites (Warren, 2010). In sulfates and carbonates, Sr cation concentrations and ratios (e.g., with Mg) could give insight into the composition of the sediment-brine interface in which Verde Fm. sulfates accumulated (Warren, 1999). Measuring Sr cations is recommended to gain further insights into groundwater flow and hydrology history of Verde Basin evaporites. One method that should be investigated to collect such data (at ~ppb concentrations) is Inductively Coupled Plasma Mass Spectrometry (ICP-MS) [Stephen Romaniello, personal communication].

In addition, nonlinear combinations of diagenetic events described in our model (whose combined effects are unknown) may have affected the BPP at any pathway. Still, this model provides a starting point for future efforts to understand principles of selective preservation in evaporitic environments originating from Mg-Na-Ca-SO_4-Cl brines.

2.4.4. Complimentary Analyses to Understand BPP

The method presented here demonstrates the importance of using a suite of instruments, each with different and complimentary capabilities, to enhance overall understanding of an environment and where high BPP sampling targets might exist. (For example, Raman could not identify halite because it lacks Raman-active vibrational modes. EPMA was needed to confirm halite presence. XRPD could not detect Fe-oxides due to its limit of detection. Raman and VNIR confirmed Fe-oxides.) Mars 2020 payload

instruments may obtain data sets similar to those presented here. For instance, Mastcam-Z, or WATSON (Novak et al., 2015) could provide data sets analogous to petrographic microscopy; PIXL (Allwood et al., 2015) may yield elemental data sets comparable to those obtained with EPMA; and SHERLOC (Beegle et al., 2015) or SuperCam (Maurice et al., 2015) should yield mineral and organic Raman spectral data sets, but with additional instrument enhancements (e.g., fluorescence mitigation through wavelength optimization; see Chapter 4 and Shkolyar et al., submitted, for details).

2.5. CONCLUSIONS

Playa evaporites are examined from the Miocene-Pliocene Verde Fm. of central AZ and identified as potentially valuable Martian analogues. This study demonstrated one approach for addressing NASA's priorities for upcoming Mars exploration efforts to characterize past habitable environments and favorable sampling targets based on their BPP.

Outcrop observations were integrated with data from a suite of laboratory techniques to identify five distinct subfacies comprising the evaporite playa sedimentary system. A model was inferred for the diagenetic history of the Verde evaporites based on the five recognized subfacies, consisting of four main diagenetic pathways (A0-D0) and six associated later stage alterations (Pathways A1-A5, B1). The environment formed during the Miocene, when fine-grained sediments derived from alluvial fan sources to the south were deposited onto playa surfaces. In the shallow subsurface, early displacive growth gypsum (DGG) precipitated within playa muds (Pathway A0). DGG experienced five later-stage alteration events (Pathways A1-A5). Gypsum dissolved and formed

external cavities within the playa muds. Dissolution cavities were infilled with secondary gypsum and in some instances, recrystallized to coarser crystallite sizes. Gypsum also dehydrated to form Ca-sulfates with an intermediate hydration state, or experienced Na-Ca-Sr cation substitution. Another subfacies environment formed on the playa surface by evaporite dissolution. This process created surface depressions where brine pans formed, supporting the growth of bottom-nucleated halite in localized shallow brine ponds (Pathway B0) accompanied by later thenardite replacement (Pathway B1). During the Pleistocene, a perennial lake system developed in the Verde Basin, precipitating extensive deposits of Mg-carbonate and emplacing carbonate cements (Pathway C0). During the Pliocene, cyclic oxidization of pore fluids precipitated, selectively cementing playa muds (Pathway D0).

This study proposes a model of long-term BPP within each subfacies across the diagenetic pathways outlined above, assuming that TOC values obtained from bulk samples for each subfacies are a proxy for BPP. Initial sedimentation of fine-grained muds onto ephemeral playas from alluvial fan sources was inferred to be the earliest stage of biosignature capture, with the highest BPP. The mudstone subfacies (both gray and red, Fe-oxide rich types) was found to have a high BPP, compared to the DGG and halite-thenardite pod subfacies, which showed comparable, but lower BPPs. The higher BPP in mudstones is likely due to the abundance of smectitic clays, low permeability and fine-grained carbonate cements. Analyses of the red mudstones and red DGG samples showed that Fe-rich oxidation did not play a major role in reducing BPP. Low BPP in DGG and halite-thenardite pod subfacies was attributed to later stage alteration events in DGG, as well as localized brine-rich environments, oxidizing fluids, and recycling of evaporites

within ponded environments. These results may help refine taphonomic models for BPP in evaporite environments originating from Mg-Na-Ca-SO_4-Cl brines in basins.

For similar habitable environments on Mars, this observational framework may guide the identification of samples that have the highest BPP for both *in situ* analysis and sample selection for MSR. Two upcoming missions, Mars 2020 (NASA) and ExoMars (European Space Agency), will usher in a new era in Mars exploration: the rover-based search for potential biosignatures based on BPP. To enhance the success of *in situ* sampling strategies employed on these missions, further studies are warranted to refine and quantify the definition of BPP, especially studies that employ *in situ*, non-destructive, and micro-scale techniques.

CHAPTER 3

VISIBLE EXCITATION RAMAN SPECTROSCOPY FOR FOSSIL BIOSIGNATURE AND MINERAL IDENTIFICATION: CHALLENGES AND RECOMMENDATIONS FOR MARS SAMPLE RETURN

3.1. INTRODUCTION

NASA's 2011 Decadal Survey (NRC, 2011) emphasized searching for life on Mars as its highest priority flagship class mission for the coming decade. The 2008 NASA Astrobiology Roadmap (Des Marais et al., 2008) included a goal to "determine how to recognize signatures of life on other worlds…[by identifying]… biosignatures that can reveal and characterize past or present life in ancient samples from Earth, [and] extraterrestrial samples measured *in situ* or returned to Earth…."

Determining whether life ever existed on Mars is likely to come by searching for biosignatures in samples analyzed in laboratories on Earth (Farmer and Des Marais, 1999). Mars Sample Return (MSR) is a logical next step in this endeavor, provided the returned samples are selected *in situ* based on their (1) association with past habitable environments and (2) potential to preserve biosignatures (Farmer, 2012). An important first step towards MSR is the 2020 Mars rover mission, detailed in Chapter 1. The 2020 mission highlights the need to develop *in situ* techniques for sample selection and MSR that can meet these two objectives.

3.1.1. Assessing the Preservation Potential of Aqueous Sedimentary Deposits

On Earth, the most abundant form of fossilized organic matter is kerogen, a degraded, macromolecular form of fossilized organic matter found in aqueously formed sedimentary rocks. Sedimentary kerogen is a major carbon sink in the global carbon cycle and represents the largest pool of organic matter on Earth: $\sim 10^{16}$ tons of C compared to $\sim 10^{12}$ tons present as living biomass (Vandenbroucke and Largeau, 2007). With progressive burial, kerogen typically undergoes thermal maturation, which results in the loss of its volatile components. This maturation process is accompanied by the progressive cross-linking of polymers and a change in the optical properties of kerogen from amber-colored, transparent forms of immature kerogen, to mature forms that are dark brown and opaque. Kerogen represents the most abundant type of biosignature on Earth and is therefore a logical target in the exploration for a Martian fossil record.

On Earth, aqueous lithologies that commonly capture and preserve fossil organic matter include evaporites (i.e., sulfates), cherts, carbonates, and clay-rich shales. Spectral signatures of these lithotypes have been identified on Mars orbit by the orbiters such as the CRISM (Compact Reconnaissance Imaging Spectrometer for Mars) instrument, onboard NASA's Mars Reconnaissance Orbiter (MRO), and by the OMEGA VIMS (Visual and Infrared Mapping Spectrometer) on the Mars Express orbiter. The same lithologies have also been detected by rovers, including the Mars Science Laboratory (MSL) "Curiosity" rover and the Mars Exploration Rover (MER) missions, Spirit and Opportunity. These lithotypes have long been considered high-priority targets in the search for a Martian fossil record and provide a logical focus for this study (Farmer and Des Marais, 1999).

For example, sulfates are aqueous minerals that form in the presence of water. Recent work has shown that the common hydrated calcium sulfate, gypsum, preserves a diverse kerogenous microfossil record, making it a promising target in the search for past life on Mars (Schopf et al., 2012). Previous investigations on Mars, both ground-based (Glotch et al., 2006; Squyres et al., 2004; Squyres et al., 2012) and orbital (Gendrin et al., 2005; Bibring et al., 2006; Glotch and Rogers, 2007), have repeatedly confirmed the presence of hydrated sulfates and cation compositions, including gypsum ($CaS0_4 \cdot H_2O$). Sulfates occur on Mars as components of soils and as evaporite deposits. Sulfates also occur as subsurface vein fill deposits at Yellowknife Bay, Gale Crater, (Grotzinger et al., 2014) and at Endurance Crater, in Meridiani Planum (Squyres et al., 2012).

In surface environments on Earth, amorphous (opaline) silica is metastable. It transforms during diagenesis (post-depositional alteration processes) through intermediaries to its ordered polymorph, quartz. The dense crystalline structure of quartz enhances its resistance to weathering and erosion. It has a prolonged residence time in the crust, making it effective for preserving fossil biosignatures (Farmer and Des Marais, 1999). Chert is a dense, highly silicified (>95% silica), fine-grained sedimentary rock, whose dense crystalline structure resists chemical weathering (Hesse, 1990), formed by aqueous depositional processes. It is the most common lithotype for well-preserved microbiotas in the Precambrian record on Earth. On Mars, silica has been detected as the amorphous form, Opal-A, in surface outcrops at Home Plate, in the Columbia Hills of Gusev Crater, using instruments on the Spirit rover (Ruff et al., 2011). Silica enrichment at Home Plate was attributed to hydrothermal spring activity (Squyres et al., 2004; Ruff et al., 2011). Near IR orbital detections from CRISM uncovered localized hydrated silica

deposits in the Syrtis Major volcanic caldera, suggesting a possible volcanically driven hydrothermal system (Skok et al., 2010). Quartz was also recently detected by MSL, as a minor phase in an aeolian sand ripple at Rocknest (Bish et al., 2013). Chert's precursor opaline silica, and a low-pressure, high-temperature polymorph, tridymite, have all been detected recently at Mars rover landing sites (Skok et al., 2010; Ruff et al., 2011; Morris et al., 2016). However, chert has not yet been detected on Mars.

Another important aqueous mineral group detected on Mars is carbonate. Limestones and dolomites are common host lithologies for the Precambrian fossil record on Earth (Farmer and Des Marais, 1999). The precipitation of carbonate minerals is favored under alkaline pH and can occur over a broad range of temperatures. Detections of Martian carbonates (including the possible detection of the Mg-carbonate, magnesite, dolomitic magnesite, and as the hydrated form, hydromagnesite) suggest that ancient aqueous solutions on Mars included neutral to alkaline pH (Brown et al., 2010; Ehlmann et al., 2008a; Morris et al., 2010). Acidic conditions have also been suggested, but in conjunction with sulfates attributed to acid-sulfate weathering (Banin et al., 1997; Golden et al., 2005; Madden et al., 2004).

Other lithotypes that are a common target for organic biosignatures on Earth are fine-grained mudstones and shales, particularly those that contain hydrated aluminum phyllosilicates (i.e., clays). Adsorption of organic compounds as molecular monolayers on clay surfaces and the reduction of permeability during compaction and cementation help protect organic matter against degradation during diagenesis, thus promoting preservation. Unsurprisingly, most petroleum source rocks on Earth are shales. Clays on Earth are produced by the aqueous weathering of pre-existing rocks, or by authigenic

precipitation during diagenesis. Phyllosilicate-rich rocks on Mars have been given a high potential for capturing and preserving organic materials (Farmer and Des Marais, 1999; Ehlmann et al., 2008a). Numerous examples of clays have been found on Mars, including detections by CRISM of Fe/Mg smectite at Endeavour Crater (Noe Dobrea et al., 2012) and Jezero crater (Ehlmann et al., 2008a), and MSL detection of saponite in the Sheepbed mudstone at Yellowknife Bay (Vaniman et al., 2014).

3.1.2. Raman Spectroscopy

When MSR occurs, the sample mass returned will likely be restricted to ~30 samples and a total mass of <500 grams (Mustard et al., 2013). Thus, there is great need for *in situ* instruments that can accurately pre-select the most promising samples for return to Earth.

Raman spectroscopy is a favored method for identifying aqueous samples with high preservation potential. It is a light scattering vibrational spectroscopy technique that provides information about molecular vibrations and structures for a wide range of mixed phase materials (Sharma et al., 2003).

Raman can also identify kerogen and other carbonaceous matter present in samples. The technique requires minimal sample preparation (usually grinding to flatten the rock surface enough to reduce laser scatter). Raman spectroscopy has a long history of *in situ* analyses of both organic and inorganic compounds in geological samples on Earth. For example, Raman spectroscopy has been employed for non-destructive, *in situ* detection and characterization of biomarker organic materials, such as photosynthetic (chlorophyll) and sunscreen (carotenoid) pigments in Antarctic microbial endoliths

(Wynn-Williams and Edwards, 2000) and other extremophilic communities (Dickensheets et al., 2000; Edwards et al., 2012; Jorge-Villar and Edwards, 2013).

Raman spectroscopy has also been used for lab identification of microfossils and their mineral matrices in the Archean-aged Apex Chert of the Pilbara region, Western Australia (Schopf, 1993; Schopf et al., 2002; Brasier et al., 2002; Marshall et al., 2011; Marshall et al., 2012). These analyses highlight an important misconception about the detection of kerogenous spectral signatures with Raman: detection alone does not prove biogenicity. Spectral features of biologically-derived kerogen can be similar to poorly ordered carbonaceous materials of abiotic origin (Brasier et al., 2002; Pasteris and Wopenka, 2003; Marshall et al., 2010). Proving the biogenicity of terrestrial kerogen is very difficult, as illustrated by ongoing debates over the origin of the carbonaceous signatures from 3.46 Ga Apex Chert and the ~3.8 Ga meta-sedimentary rocks of the Isua Supracrustal Belt in Greenland (Schidlowski et al., 1979; Schidlowski, 1988; Schidlowski, 2001; Mojzsis et al., 1996; van Zuilen et al., 2003). Proving the biogenicity of organic matter could be equally challenging for samples returned from Mars.

The "earliest fossil" debates have shown that understanding the detailed petrogenetic context of kerogen is crucial for assessing potential biogencity. For accurate petrogenetic interpretations, it is a well-established fact that information about *both* mineralogy and microtexture is necessary. This was recognized by the NASA Mars 2020 Rover Science Definition Team who specified combined capabilities of a payload to identify both minerals and organic matter in samples and place them in a microtexural framework (Mustard et al., 2013). Raman analysis does not require powdering a sample and is a non-destructive surface technique. Thus, compositional information from Raman

spot analyses may be easily placed within a spatial context provided by microscale imaging. Consistent with this strategy, samples were characterized at the microscale by thin section petrography to interpret how paragenesis (time-ordered sequence of environmental processes) and diagenesis (post-depositional alteration processes) affect mineralogy, microtexture, and kerogen preservation. This framework provided a context for selecting optimal locations for Raman analyses.

3.1.3. Kerogen in the Raman Spectrum

In Raman spectroscopy, kerogen is identified by two disordered carbon bands representing diagenetically mature or maturing (i.e., graphitizing) carbon macromolecular phonon modes. Spectral features consist of a "D band," or disordered carbon-carbon lattice stretching mode, at 1350 cm^{-1}, and an sp^2 in-plane carbon-carbon stretching mode, the "G band," or graphitized carbon mode, at 1600 cm^{-1} (Pasteris and Wopenka, 2003; Marshall et al., 2010). The detection of the D and G bands in a sample on Mars would be considered strong evidence for caching a sample for return to Earth where additional analyses could be used to determine biogenicity.

3.1.4. Raman Instruments for Mars

Although no Raman instrument has yet flown to Mars, the European Space Agency (ESA) and NASA Mars programs have been developing Raman as a tool for near-future *in situ* missions.

The Mars Microbeam Raman Spectrometer, or MMRS (Wang et al., 2003), was developed as a flight instrument to identify minerals *in situ* and to assist in sample

selection for MSR. It was designed to use line-scanning capability with a 532 nm excitation laser. The Mars Microbeam Raman Spectrometer (MMRS) was proposed (but not selected) for the NASA Mars Exploration Rovers (MER), MSL, and 2020 missions.

ESA's Raman Laser Spectrometer (RLS), also with a 532 nm excitation laser, is currently being developed for the ExoMars mission. ExoMars is scheduled for launch in 2018 (Rull, 2014) and will carry the first Raman flown to another planet.

NASA's Mars 2020 rover will carry two Raman instruments. One will be an arm-mounted, Deep UV (DUV; 248.6-nm) resonance Raman and fluorescence spectrometer called SHERLOC, or Scanning Habitable Environments with Raman & Luminescence for Organics & Chemicals instrument (Beegle et al., 2014). The second will be the mast-mounted SuperCam, an integrated Laser-Induced Breakdown Spectroscopy (LIBS), Raman Spectroscopy, and time-resolved fluorescence spectroscopy instrument. SuperCam will perform time-gated (see next section for details) 532 nm excitation Raman measurements (Clegg et al., 2015).

3.1.5. Fluorescence Challenges in the Interpretation of Raman Spectra

Fluorescence is a major issue in the development of Raman systems for both Earth and Mars. When light interacts with matter, the resulting Raman process (a type of inelastic photon scattering) is a weak process that has to compete with absorption effects, such as fluorescence (Frosch et al., 2007). Fluorescence originates from two effects: (1) long (>10 ns - ms) lifetime effects arise from inorganic sources, such as lattice defects and impurities in the mineral lattice (trace metals or rare Earth elements; Bozlee et al.,

2005; Wang and Mullins, 1997) and (2) short (<1-10 ns) lifetime effects that arise from chromophores in the organic matter (Bozlee et al., 2005).

Persistent problems with high background fluorescence have been widely recognized in Raman spectroscopy in the identification of minerals (Bartholomew, 2012), kerogen (Marshall et al., 2006; Marshall et al., 2010; Schopf et al., 2012), and other potential biosignature materials (Dickensheets et al., 2000; Som and Foing, 2012), both in the lab and in field-deployed Raman systems (Jehlicka et al., 2010). Many approaches have been developed to reduce fluorescence for commercial systems not developed for flight. They include resonance Raman (Frosch et al., 2007), confocal Raman (Brasier et al., 2002), optimizing the wavelength of the laser (Bartholomew, 2012; Som and Foing, 2012), and shifted-excitation Raman difference spectroscopy, or SERDS (Shreve et al., 1992).

Here, the dual problems of mineral and kerogen fluorescence in Raman spectra for aqueous lithologies relevant for MSR are investigated, and the application of time-resolved Raman (TRR) to reduce fluorescence is explored. TRR has a history of successfully reducing fluorescence in Raman spectra in material science and high temperature and pressure geophysics applications, especially at the same laser wavelength excitation used in this study, 532 nm (e.g., Yaney, 1972; Goncharov et al., 2005), or near it, at 514.5 nm (Mulac et al., 1978) or 526.5 nm (Slotznick & Shim, 2008; Zucker and Shim, 2009). This study aimed to extend the application of TRR for fluorescence reduction to geological Martian sample analogs for rover-based Raman investigations.

The TRR system used in the present study has been undergoing development at the NASA-CalTech Jet Propulsion Lab (at the time of this writing). The JPL team has been optimizing this miniaturizable prototype laser Raman system for fluorescence rejection to enhance capabilities for *in situ* mineralogy on planetary surfaces and for astrobiology-relevant applications for future missions to Mars (Blacksberg et al., 2010; Blacksberg et al., 2011; Maruyama et al., 2013; Maruyama et al., 2014). The TRR uses time gating to eliminate longer-lifetime fluorescence with a solid-state sensor single photon avalanche diode (SPAD) detector (for details, see Blacksberg et al., 2010; Blacksberg et al., 2011; Maruyama et al., 2013; Maruyama et al., 2014). The SPAD collects the instantaneous Raman signal, while gating out the response of the unwanted fluorescence (which has a longer, exponentially decaying lifetime). Time-resolved detection with the JPL Raman instrument is enabled by a 500 ps, 40 KHz pulsed laser and a SPAD detector. The SPAD detector is synchronized with the laser, opening during the pulsed laser signal delivery. See Figure 3.1 for details. SPADs are similar to conventional CCDs, but are preferable for missions because they provide lower power consumption and operation voltage, smaller size, higher durability, and detection sensitivity (Maruyama et al., 2013).

In a gated Raman system, short gate times increase signal and decrease background fluorescence. The basic principles involved in gating using the SPAD investigated in this study are illustrated in Figure 3.1. In a gated Raman system synchronized with a pulsed laser, signal improvement can be can be quantified by considering photon counting statistics (Mulac et al., 1978; Slotznick and Shim, 2008; Zucker and Shim, 2009). According to this principle, acquisition time for a measurement

can be calculated as signal^2/background (Mulac et al., 1978). Additionally, uncertainty in measuring the emitted photons can be approximated with a Poisson distribution in time. Considering these principles, photon detection can be shown to have increased signal and reduced background when acquisition time is very short, and gate width and pulse repetition frequency are decreased (Slotznick and Shim, 2008; Zucker and Shim, 2009).

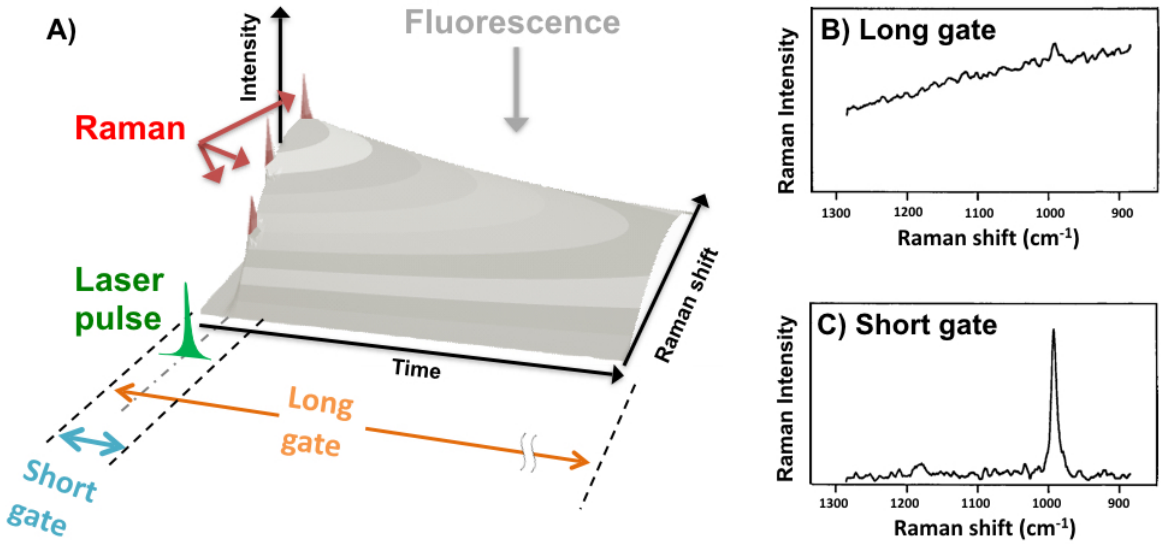

Figure 3.1. Fluorescence rejection with Time-Resolved Raman (TRR). **(A)** Raman and fluorescence signals occur at the same start time after the laser pulse but are different in lifetime and magnitudes. The SPAD detector collects the signal which falls within a chosen time gate. Gate widths (long vs. short) are separated by a customizable gate delay. The optimal gate opens for the time allowing the majority of the instantaneous Raman signal to be delivered to the detector, while gating out much of the longer lifetime fluorescence signal. The gate width and delay can be chosen by the user. Fluorescence has an exponentially decaying lifetime, which depends on the source (organics vs. minerals; see Section 3.1.5). The small portion of the fluorescence signal that overlaps with the Raman signal is detected because it is captured in the open gate detection. Note that the signal intensities pictured are arbitrary. (**B**) In this example of a fluorescent Raman signal, when a long gate is chosen, the sloping fluorescence signal overwhelms a potential Raman band weakly visible around 990 cm^{-1}. (**C**) When a shorter gate is chosen, fluorescence is largely reduced, bringing out a flatter signal with the Raman band in the same location as in (B) visible with high confidence. (Note that it is conventional to display the wavenumber axes in either increasing or decreasing order in Raman spectra.) Image courtesy Y. Maruyama.

3.2. METHODS

To better understand the challenges of sample selection for MSR using Raman spectroscopy, natural geological samples were analyzed using a variety of methods, including microscopy, X-ray powder diffraction (XRPD), and two Raman systems, a CW (continuous wave), or conventional system, and a time-resolved Raman (TRR) system. The goals of the study were to:

1. Evaluate sample selection capabilities of Raman to successfully cache a sample for MSR, assuming a diverse sample suite;

2. Identify sample- and technology-specific issues (including fluorescence) that are likely to arise during MSR scenarios with Raman systems currently being developed for flight; and

3. Provide recommendations for improving the success of sample selection for MSR using Raman spectroscopy.

The following data sets were collected for each of the 6 samples comprising this study suite (summarized in Table 3.1 and discussed in the Results section, 3.3).

1. Petrographic thin sections were acquired from each sample and digital images were acquired under transmitted, cross-polarized, and reflected light illumination. Detailed petrographic analyses provided a basis for petrogenetic interpretations to establish the depositional setting, to document diagenetic processes, and to develop a paragenetic (time-ordered) framework for microtextures, minerals, and carbonaceous materials.

2. Microscopic screening of samples allowed the identification of regions of interest for Raman spot analyses. Markers were placed on thin sections to target the locations of representative kerogen grains and minerals for interrogation. Markers allowed the same grains to be mapped and tracked consistently from thin section microscopy, through Raman analyses with both Raman systems (detailed in the next sections).
3. Two different 532 nm excitation wavelenght Raman systems, a laboratory CW system and a TRR system, were used to obtain point spectra for the kerogen and mineral grains mapped in thin sections.
4. XRPD analyses of bulk, powdered samples were obtained as an independent confirmation of mineralogy and for comparisons to optical microscopy and Raman analyses.

3.2.1. Samples and Preparation

Six samples were selected from Jack Farmer's research collections to cover a broad range of depositional environments, ages, diagenetic histories, kerogen maturities, and modes of preservation. Sample selections focused on aqueous mineral compositions and environments that are considered important exploration targets for fossil biosignatures (Farmer and Des Marais, 1999), and which have been previously identified as being present on Mars (Bibring et al., 2005; 2006; Bish et al., 2013; Brown et al., 2010; Glotch et al., 2006; Grotzinger et al., 2014; Ehlmann et al., 2008a; 2008b; Murchie et al., 2009; Ruff et al., 2011; Skok et al., 2010; Squyres et al., 2004; 2012). Table 3.1

provides a summary of sample localities, ages, and compositions. Samples are discussed under Results.

Standard (30 µm-thick) petrographic thin sections (obtained from Spectrum Petrographics Inc.; http://www.petrography.com) were used for both microscopy and Raman analyses.

For XRPD, bulk samples were chipped with a hammer, crushed in a Plattner mortar, ground to a fine powder using a quartz mortar and pestle, and passed through a 150-µm sieve. To confirm that grain size or the 150-µm sieve did not produce an effect or skew diffractograms, the Green River carbonate sample was sieved to 38 µm, and reanalyzed by XRPD. Both diffractograms were indistinguishable.

3.2.2. Microscopy

Thin sections were analyzed using a Nikon Eclipse E600 POL polarizing microscope. Digital images were captured with an Optronix digital camera system. For each field of view, photomicrographs were obtained under transmitted light (both plane- and cross-polarized), as well as reflected light illumination. Major and minor mineral components were documented, along with representative microtextural features. Primary and secondary (authigenic) mineral components were distinguished. Spatial relationships between minerals and fabric elements were used to develop a paragenetic framework for reconstructing diagenetic processes. A persistent effort was made to track all minerals identified by XRPD back to thin sections, in order to establish their place in paragenesis. Identifications of minerals were based on common optical properties. However, not in all minor phases could be identified in thin section.

Kerogen and opaque mineral grains (e.g., Fe-oxides) are sometimes difficult to distinguish in thin section. To help separate these phases during the kerogen mapping phase, representative grains were examined under reflected and cross-polarized illumination and those having the best optical fit with kerogen were targeted for further analysis. Adhesive markers attached to uncovered thin sections were used to identify suspected grains. Compositions were confirmed by Raman analysis. This method resulted in the successful targeting of a representative kerogen grains in each sample, and the successful relocation of the same regions for analysis with both Raman systems.

3.2.3. Raman Spectroscopy

Raman data were obtained using two different systems: a continuous wave (CW) system at ASU's Center for Solid State Science and the time-resolved Raman (TRR) system at NASA's Jet Propulsion Laboratory

For CW measurements, a custom-built CW laboratory micro-Raman system was used with a Princeton Instruments liquid nitrogen cooled detector and Acton spectrometer. This system uses a 532 nm laser. A range of 12 power settings (0.4 uW to 74 mW) were available and were set manually for each analysis. The system has a spectral resolution of ~2 cm^{-1}, spatial resolution of ~0.5 μm, and a 1200 lines/mm grating. Power settings and integration times used for each spectrum are noted in image captions.

The TRR system uses a 532 nm excitation Arctic Photonics 500 ps-pulsed microchip laser at 40 KHz which delivers ~1 μJ/pulse. The sensor is a solid-state, single photon avalanche diode (SPAD) detector. Spectra were integrated for 5 minutes or less.

All data were taken at either 4 mW or 10 mW delivered to the thin section surface. The gate width used was 1 ns and the gate delay shift was 250 ps. Each spectral acquisition was optimized for the gate delay setting on the SPAD, which allowed for the largest Raman signal (and highest fluorescence rejection) to be obtained.

For both Raman systems, analyses were acquired from clean, uncovered thin sections as point spectra of the kerogen and mineral grains of interest. Raman shift position calibrations were performed using a cyclohexane standard. Both Raman systems had a built-in transmitted light microscope for locating and imaging the laser spots on samples where spectra were obtained. The Raman laser spot was manually focused on the surface of the thin section at the location of interest. Spectra were acquired at the optimal integration time, power setting, and interrogation depth below the surface of the thin section. No background correction was applied during analysis. Mineral identifications were obtained using CrystalSleuth (Downs, 2006), which includes a reference library of minerals obtained using a 532 nm laser.

Care was taken to avoid organic contamination during Raman analyses. Epoxy (EPOTEK 301 resin from Epoxy Technology), as well as the immersion oil (non-drying type B from Cargille Laboratories, Inc.) was used in preparing thin sections interrogated with Raman. No spectral features from epoxy or immersion oil were seen in the Raman spectra from samples. Since the locations of regions for Raman analyses were identified with stickers, the Raman laser beam was carefully positioned to miss the markers. This was enabled on both Raman systems with transmitted light microimaging system. Contamination from the sticker adhesive was avoided by cleaning each thin section with 95% ethanol and distilled water prior to analysis.

It is important to note that this study was not designed to compare the functionalities (i.e., laser properties, etc.) of the two Raman instruments, nor was it intended to make comparisons between a CW laboratory system not designed for space flight and the TRR prototype which is undergoing optimizations for fluorescence reduction, acquisition speed, higher S/N, among other features. Such comparisons would require the same functionalities for both systems, which was not the case.

3.2.4. XRPD

A Siemens D5000 X-ray Diffractometer with a Ni-filtered Cu radiation source was used to identify minerals present in bulk samples. Sample powders were mounted on zero background quartz crystal holders (i.e., on a plane that does not diffract X-rays) and scanned from 5° to 81.759° with a step size of 0.016303. Operating conditions were 40 KV at 30 mA using CuKα ($\lambda_{\alpha 1}$ = 1.5060 Å; $\lambda_{\alpha 2}$ = 1.54439 Å), with an 8 second dwell time, for a total analysis time of 12 hours per sample. Data reduction and mineral identifications were performed using *JADE*™ software V9 (www.materialsdata.com), by matching to diffractograms in the International Centre for Diffraction Data (ICDD) library database.

3.3. RESULTS

Results reported here are for analyses of the following sample types: a lacustrine calcareous oil shale; a laminated sulfate-carbonate evaporite; a siliceous mudstone; a hydrothermal chert; a lacustrine stromatolitic limestone; and a carbonate-cemented

fluvial-marine sandstone. Sample analyses, details, and components are detailed briefly below and summarized in Table 3.1, which follows the below sample descriptions.

3.3.1. Eocene Calcareous Oil Shale, Green River Formation, Wyoming

The calcareous oil shale analyzed in this study was collected from a fossiliferous member of the Eocene (56 - 34 MYA) Green River Formation (Eugster and Surdam, 1973). The Formation is a lacustrine deposit that accumulated in three major basins now exposed along the Green River in portions of Utah, Wyoming, and Colorado. The sediments are varved, consisting of alternating light and dark laminae. The formation includes a diverse range of lithotypes. The sample analyzed for this study was rich in alternating organic-rich (dark) and calcite-rich (lighter) laminae (Figure 3.2A).

The main constituent of the rock is fine-grained calcite ($Ca[CO_3]$). The sample is described as a micritic (rich in microcrystalline calcite) mudstone, showing patchy recrystallization to form areas consisting of interlocking crystals of sparry calcite. Lighter laminae were dominated by microspar (crystal mosaics of calcite formed by re-crystallization). Calcite was identified by Raman and polarized light microscopy. The sample analyzed was a thin section with no accompanying hand sample, thus no XRPD analysis was performed on it.

Thin section microscopy revealed an unknown honey-colored phase. High background fluorescence of this phase prevented its identification using CW Raman (Figure 3.6C-F) and TRR.

Our thin sections of the Green River Formation contain abundant kerogen. However, multiple CW Raman analyses were required for definitive identification. CW

Raman could not confirm most kerogen because of strong fluorescence (see Figure 3.2B). TRR analyses required multiple attempts for kerogen identification but resulted in spectra showing weak but still visible kerogen bands on a high fluorescence background.

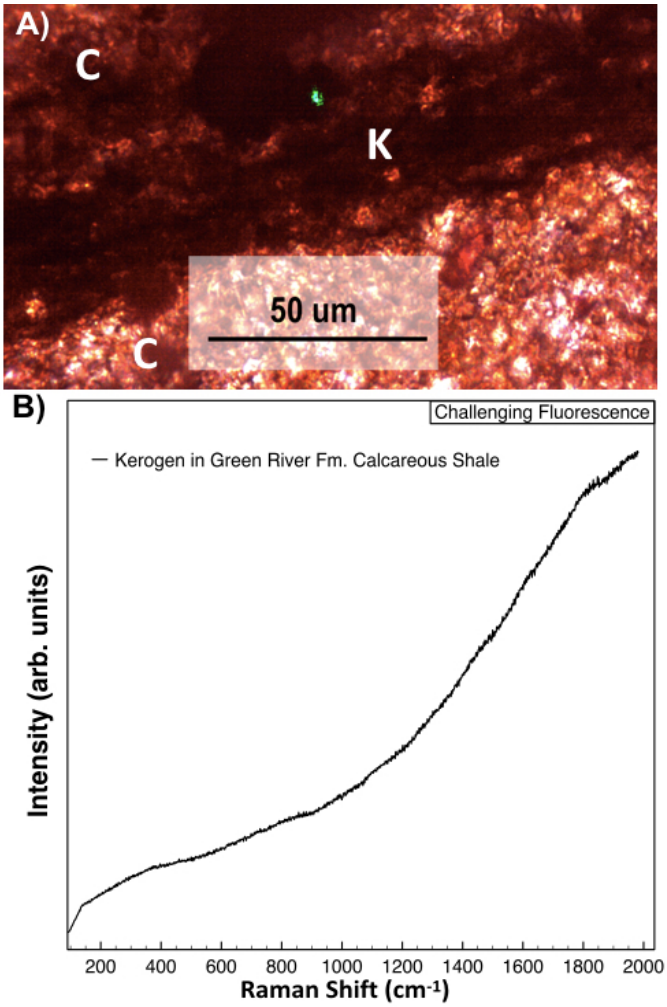

Figure 3.2. Green River Fm. (GRF) shale. **(A)** A transmitted light image is shown of a kerogen grain between two laminations of the GRF shale. The dark lamination, labeled "K," is rich in kerogen and other organics. The lighter, calcite-rich laminations are labeled "C". The green Raman laser spot is on a dark grain interpreted to be kerogen using microscopy analyses. **(B)** The dark grain in (A) was interrogated multiple times with CW Raman. No kerogen bands were visible due to high fluorescence. Settings for the kerogen spectrum were ten, 10-sec. exposures at 1.3 mW, but all powers, integration times, and focus depths attempted for this region produced a similar, highly fluorescent spectrum.

3.3.2. Permian Sulfate Evaporite, Castile Formation, Delaware Basin, Texas

The Castile Formation (Permian; 300 – 250 MYA) is a calcium sulfate evaporite deposit that underlies the Delaware Basin of northwest Texas (Anderson et al., 1972). The formation was deposited as a deep-water evaporite, with primary anhydrite ($CaS0_4$) nucleating in the water column, then settling to the bottom of the basin to form a laminated (varved) sulfate-carbonate deposit. Subsequent uplift along the margins of the Delaware Basin exposed the primary anhydrite to near-surface fresh groundwater. Hydration of the anhydrite formed gypsum ($CaS0_4 \cdot H_2O$), seen in surface outcrops. Formation of gypsum was accompanied by a volume change that caused compressional folding of laminae. Dark laminae are composed of fine-grained, organic-rich carbonate mud (micrite), typically as dolomite, but including calcite. Light laminations are composed of euhedral crystals of gypsum and anhydrite. Dolomite was identified using all techniques except XRPD. Figure 3.3 shows a kerogen grain surrounded by fine-grained dolomite. Gypsum and calcite were identified by microscopy, CW Raman, and XRPD. Anhydrite or gypsum were suspected but indistinguishable in thin section microscopy, but anhydrite was confirmed with CW Raman and gypsum with XRPD. Other trace mineral components identified with XRPD are listed in Table 3.1.

Fine-grained kerogen was abundant in the Castile Fm., mostly occurring in the carbonate-rich laminations, as illustrated in Figure 3.3 and also reported in previous studies (Lockard, 2009). Kerogen was identifiable using both CW (Figure 3.3) and TRR methods. However, multiple attempts with elevated power settings were required with CW Raman due to high background fluorescence.

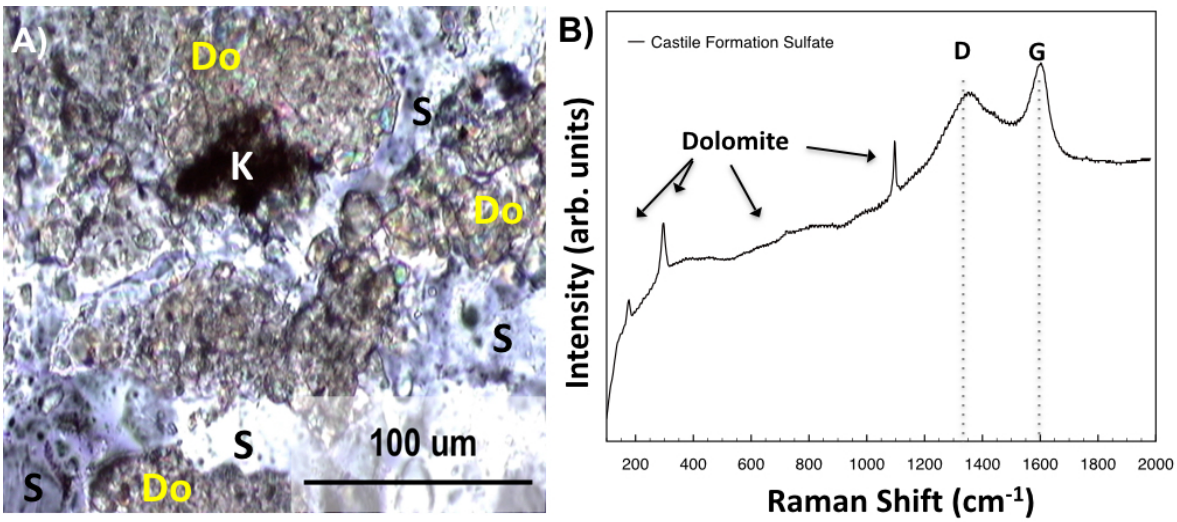

Figure 3.3. Castile Formation sulfate evaporite. **(A)** A cross-polarized light photomicrograph is shown of a kerogen grain ("K"). This grain was interrogated with CW Raman to produce the spectrum in (B). Dolomite ("Do") surrounds the kerogen, as indicated by the Raman spectrum in B of this same region. Sulfate ("S") is visible, based on optical properties but not detected with CW Raman at the spot analyzed. **(B)** A Raman spectrum of the kerogen grain shown in (A) is seen. This kerogen grain exhibited high, but non-prohibitive fluorescence, allowing the detection of both kerogen and its surrounding matrix carbonate minerals, captured in the laser's sampling volume. The D and G band kerogen bands are clearly visible, along with dolomite (at 176, 297, 724, and 1098 cm^{-1}). This spectrum was obtained with twenty 10-sec. exposures at 6 mW.

3.3.3. Tertiary Siliceous Mudstone, Wind Mt. Mine, Gerlach, Nevada

The Wind Mt. mine, near Gerlach NV, exposes a dark grey to black, siliceous mudstone (Wood, 1991; Eneva et al., 2011). The age of the formation is poorly constrained as Tertiary (<65 MYA). In thin sections, ghosts of angular mudstone clasts are present in a structureless mudstone matrix, all replaced by microcrystalline quartz (Figure 3.4A). Quartz was detected using all four techniques (Table 3.1; Figure 3.4C). The mudstone shows evidence for pervasive hydrothermal silicification. The host rocks at Wind Mt. mine were subject to intense geothermal activity associated with pervasive silicification and the emplacement of shallow epithermal gold deposits (Wood, 1991; Eneva et al., 2011). Mineralization included the precipitation of a number of sulfide

minerals. Pyrite (FeS_2) was identified with microscopy (Figure 3.4A), CW Raman, and XRPD. (Pyrite precipitates under reducing conditions, often in association with organic matter, as seen in this sample in Figure 3.4A). Sphalerite, or (Zn,Fe)S, was identified in CW Raman and XRPD.

The sample contains abundant plant fossils and organic matter. Kerogen occurs as both morphologically distinct, permineralized plant fragments, and as particulate grains and clumps (Figure 3.4A). The sample displays moderate to low fluorescence, but kerogen was always easily detected with CW Raman (Figure 3.4D) and TRR.

3.3.4. Archean Hydrothermal Chert, Strelley Pool Formation, Pilbara, Australia

The Archean (~3.4 Ga) Strelley Pool Fm. near the Trendall locality, Pilbara, northwest Australia is a stratiform limestone-chert sequence that hosts the oldest known coniform stromatolites (Hofmann et al., 1999; Allwood et al., 2006). The sample analyzed here was collected from a large vein of black chert that is part of a dike system that cross-cuts the Strelley Pool Fm. at the Trendall locality. Microscopy revealed that this sample is dominated by a fine-grained matrix of microcrystalline quartz grains surrounding abundant, particulate kerogen (Figure 3.4). Quartz was identified with all four techniques (Table 3.1; Figure 3.4C). Carbonate was suspected based on thin section microscopy and confirmed to be dolomite by CW Raman. Dolomite was observed both in the matrix as small patches associated with kerogen and as secondary vein fills. During diagenesis, a coarsening of microcrystalline quartz occurred, forming localized patches of megaquartz (>20 μm grains; Figure 3.7B). In thin section microscopy observations, carbonate appears to have been replaced by silica (and vice versa) suggesting that the pH

of the fluids remained alkaline during diagenesis. Other components identified are listed in Table 3.1.

Most kerogen in this sample was concentrated within regions dominated by microcrystalline quartz (Figure 3.7B). Due to the low fluorescence of the Strelley Pool hydrothermal chert, kerogen was easily identified using both CW Raman (Figure 3.4D) and TRR.

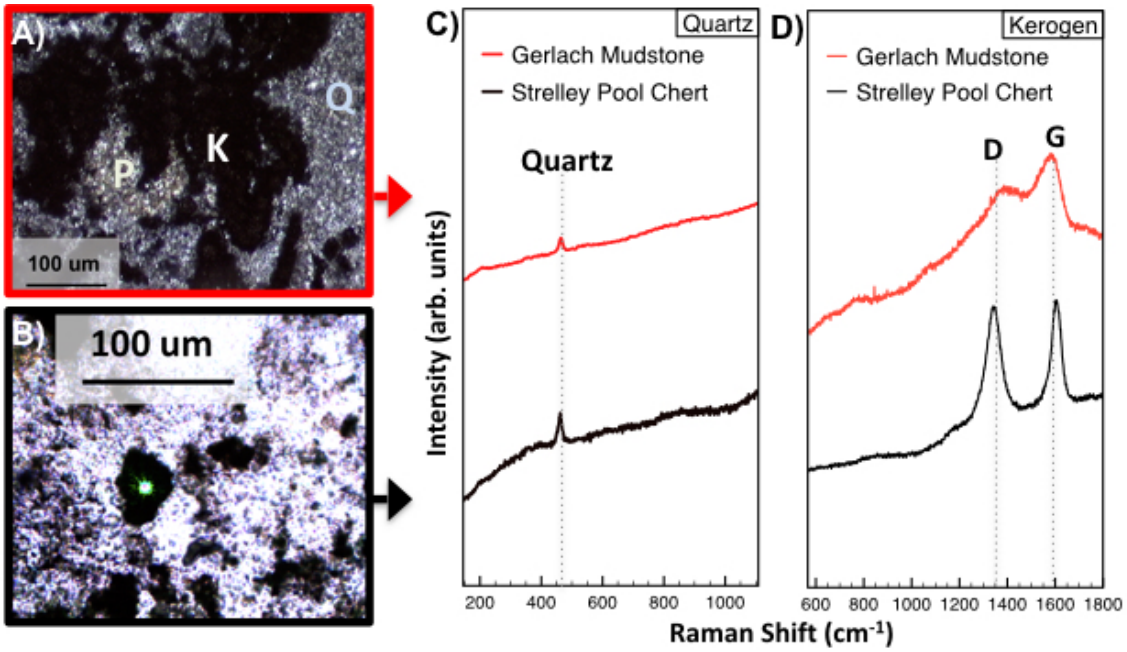

Figure 3.4. Gerlach siliceous mudstone and Strelley Pool chert. **(A)** A photomicrograph taken under cross-polarized light is shown of the Gerlach sample. "K" identifies a region of black, opaque, morphologically indistinct kerogen. A fine-grained matrix of microquartz ("Q") surrounds the kerogen. Patches of brassy pyrite ("P") are also visible in the quartz matrix. **(B)** A photomicrograph is shown of Strelley Pool, taken by the CW Raman transmitted light imaging system. Black kerogen grains are visible, surrounded by a quartz matrix. (See Figure 3.7B for a description of Strelley Pool chert's matrix in polarized light). The kerogen grain in the center of the image shows the position of the green laser spot where the two black spectra in (C) and (D) were acquired. Spectra in (**C**) and (**D**) show representative Raman spectra for Gerlach (red spectra) and for Strelley Pool (black spectra). The low background fluorescence of these samples allowed the detection of both the microquartz matrix ("Q") present, as well as kerogen ("K") in both samples. Quartz, was identified by its main band at 464 cm^{-1}. Kerogen bands were identified by the D band (~1350 cm^{-1}) and the G band (1600 cm^{-1}). The 1350 cm^{-1} band in Gerlach is visible, but is much broader and more fluorescent than that in Strelley Pool. Settings for the CW spectra were: one 10-sec. exposure at 0.75 mW for the Gerlach mudstone kerogen spectrum, one 10-sec. exposure at 6 mW for the Gerlach mudstone quartz spectrum, and five 10-sec. exposures at 6 mW for both Strelley Pool Chert spectra.

3.3.5. Holocene Stromatolitic Limestone (Carbonate), Walker Lake, Nevada

The stromatolitic limestone analyzed was collected from a shoreline terrace (Holocene, <10,000 years) along the western shoreline of Walker Lake, NV. The stromatolitic sediments show well-defined columnar morphologies (Osborne et al., 1982)

consisting of alternating dark and light laminae of microcrystalline calcite (Figs. 5A and 5C). The carbonate mineralogy was confirmed using microscopy; calcite ($CaCO_3$) was identified as the major phase using both Raman analyses and XRPD. Isolated angular, sand-sized grains of quartz and plagioclase feldspar (largely as albite, $NaAlSi_3O_8$) were also present throughout the laminated carbonate matrix, particularly between stromatolite columns. Quartz was observed during microscopy; albite was identified by all techniques (Table 3.1).

Stromatolitic laminae contain well-preserved filamentous microfossils (Figure 3.5B) and irregular patches of particulate kerogen. Kerogen was highly fluorescent, but identifiable (sometimes after multiple tries and elevated laser power), using CW Raman (Figure 3.5C). TRR provided reduced fluorescence, which resulted in consistently clear kerogen identifications.

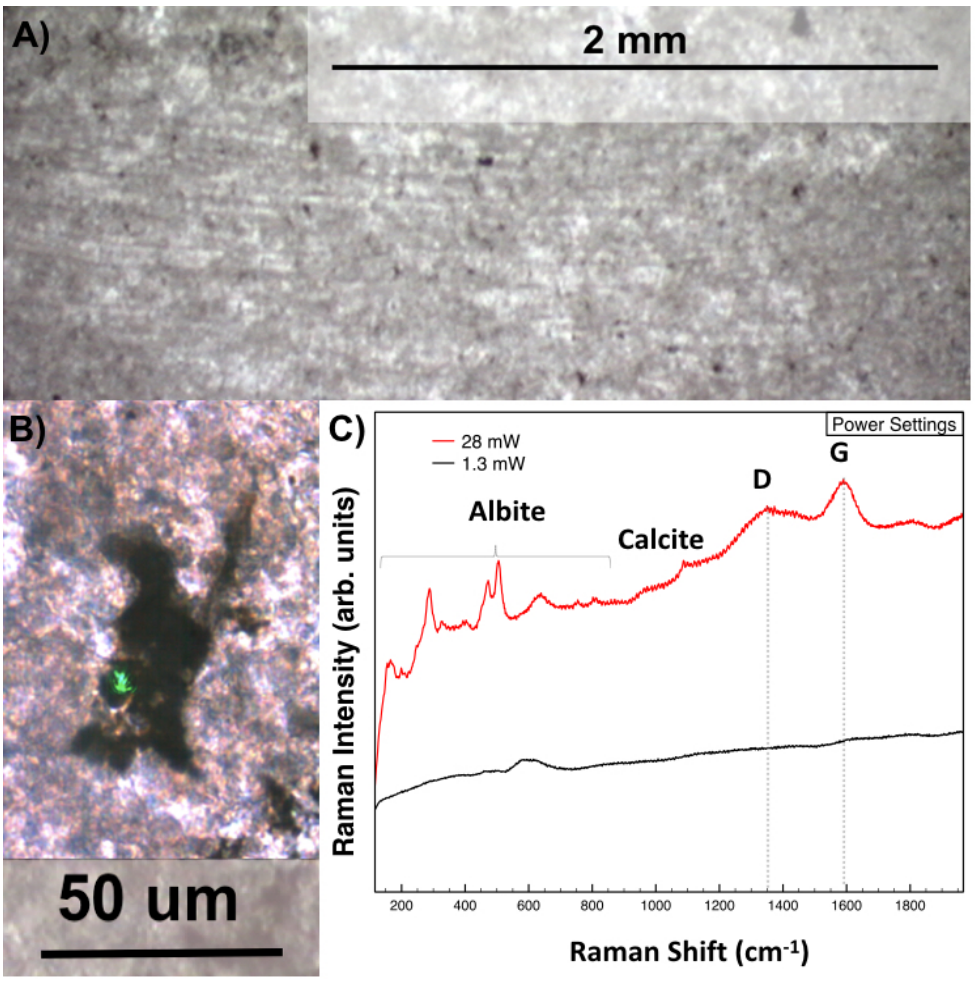

Figure 3.5. Walker Lake stromatolitic limestone. **(A)** Photomicrograph acquired under plane-polarized light illumination showing fine laminations. **(B)** A filamentous kerogen grain preserved in calcite is shown. The image shows the location of the green laser spot where spectra in (C) were obtained. **(C)** Spectra were acquired for the kerogen grain shown in (B) with progressively increasing power settings. The spectrum shown is for the lowest power setting attempted (1.3 mW). This power level did not allow kerogen bands for either the D band at ~1350 cm^{-1} or the G band at ~1600 cm^{-1}, nor the associated mineral matrix to be seen. (The broad band around 600 cm^{-1} in the low power spectrum was unidentified.) The same location was interrogated with systematically increased power settings. At the highest power setting (28 mW), albite (with bands at 162, 200, 291, 327, 403, 479, 507, 635, 762, and 815 cm^{-1}) and calcite (at 1086 cm^{-1}) were visible, along with both kerogen bands (at ~1350 and ~1600 cm^{-1}). The 1.3 mW spectrum was taken with ten 10-sec. exposures. The 28 mW spectrum was taken with ten 1-sec. exposures.

3.3.6. Cambrian Carbonate-Cemented Fluvial Sandstone, Alum Formation, Öland, Sweden

The Alum Fm. is Cambrian in age (~500 MYA; Muller et al., 2009). The sample analyzed is a fine-grained quartzo-feldspathic sandstone, cemented by carbonate. Pyrite was detected using XRPD and CW Raman. In the sample analyzed here, pyrite (FeS_2) primarily occurs as framboids in grains of kerogen, visible in reflected light. Some authors have suggested that framboidal pyrite is biomediated (Popa et al., 2004).

Several phyllosilicates were identified in the Alum Sandstone sample. Glauconite, an authigenic phyllosilicate with the formula $(K, Na)(Fe^{3+}, Al, Mg)_2 (Si, Al)_4O_{10}(OH)_2$, occurs as rounded grains in primary pore spaces within sandstone layers. Glauconite is diagnostic of marine depositional environments, forming under reducing conditions in organic-rich sediments. It is a common component of near-shore sands. Glauconite was initially identified in thin sections based on its distinctive pistachio green color (Figure 3.7B), birefringence, and friability. XRD did not identify this phase, due to its low abundance. CW Raman did not identify it due to high fluorescence. However, glauconite was identified using TRR (Figure 3.7). Micas were present in moderate abundance in thin sections, showing evidence of grain folding during compaction (Figure 3.7). Muscovite, $KAl_2(AlSi_3O_{10})(F,OH)_2$ appeared to be a good match for this mica by both petrographic analysis and XRPD. However, in TRR (Figure 3.7), mica was identified as a mix of muscovite and phlogopite, $KMg_3(AlSi_3O_{10})(F,OH)_2$, the Mg end-member of the biotitie solid solution series. In general, the phyllosilicates present in the Alum Formation sample exhibited high, often prohibitive fluorescence, using CW Raman. When successfully detected, ambiguities in Raman identification of this phase may be explained by cation

substitutions in a solid solution series that are not well captured in existing spectral libraries. Phyllosilicates in this sample generally did not meet the two-band minimum rule for confident identifications with Raman (Som and Foing, 2012). Other phases present in this sample are listed in Table 3.1.

The Alum sandstone contains abundant organic matter. This includes transparent, amber-colored grains of what appears to be immature kerogen, surrounded by halos of dark, mature kerogen, in microscopy analyses (Figure 3.6A-B). Mature kerogen was usually confirmed in both Raman analyses with moderate fluorescence that did not prohibit identifications. Immature kerogen was unconfirmed with CW Raman due to high fluorescence (Figure 3.6C).

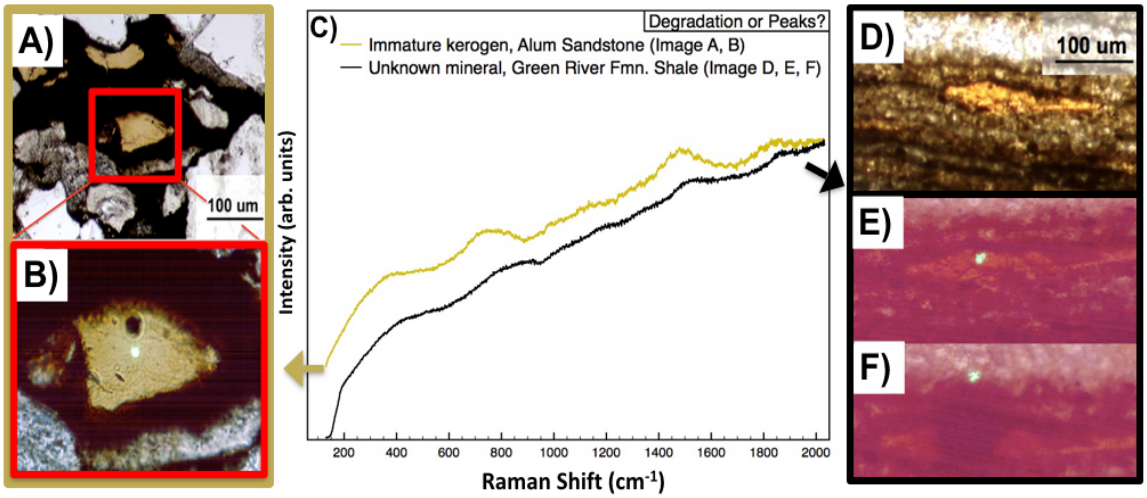

Figure 3.6. Alum Fm. sandstone and Green River Fm. shale. **(A)** A thin section photomicrograph of the Alum Fm. sample is shown, taken under cross-polarized light. Amber-colored, immature, as well as black, mature kerogen is visible. The amber grain outlined by the red box in (A) was interrogated with CW Raman. **(B)** A magnified view of (A) shows the laser spot positioned just below the black spot interrogated and was damaged by the beam. This burn spot appeared after interrogation at medium power (13 mW). **(C)** Spectra acquired at the dark spot in (B) is shown using CW Raman. Spectra are shown for the amber-colored grain in the Alum Fm. (in A, B) and in Green River Shale (in D-F). Both spectra provide Raman information that cannot be interpreted with high confidence. The broad region around 1450 – 1500 cm^{-1} seen in the Alum spectrum may be attributable to several potential sources, discussed in the text. The region around 700 cm^{-1} is unidentified. The Alum sandstone spectrum shown was produced with one 2-sec integration. Settings for GRF spectrum were one 1-sec. integration, although multiple settings produced similar spectra in both cases. **(D)** This plane-polarized light photomicrograph of a Green River Fm. thin section shows an unknown phase that could not be identified with Raman (spectrum in C). **(E)** The same grain as shown in (D) is shown; the location of the green laser spot is visible where the spectrum in (C) was obtained. **(F)** The sample was interrogated over a wide range of power settings (up to 28 mW). This caused dark degradation spot on the sample, visible as a large, dark area under the green laser spot in this image. The fluorescent spectrum in C was seen after this damage appeared.

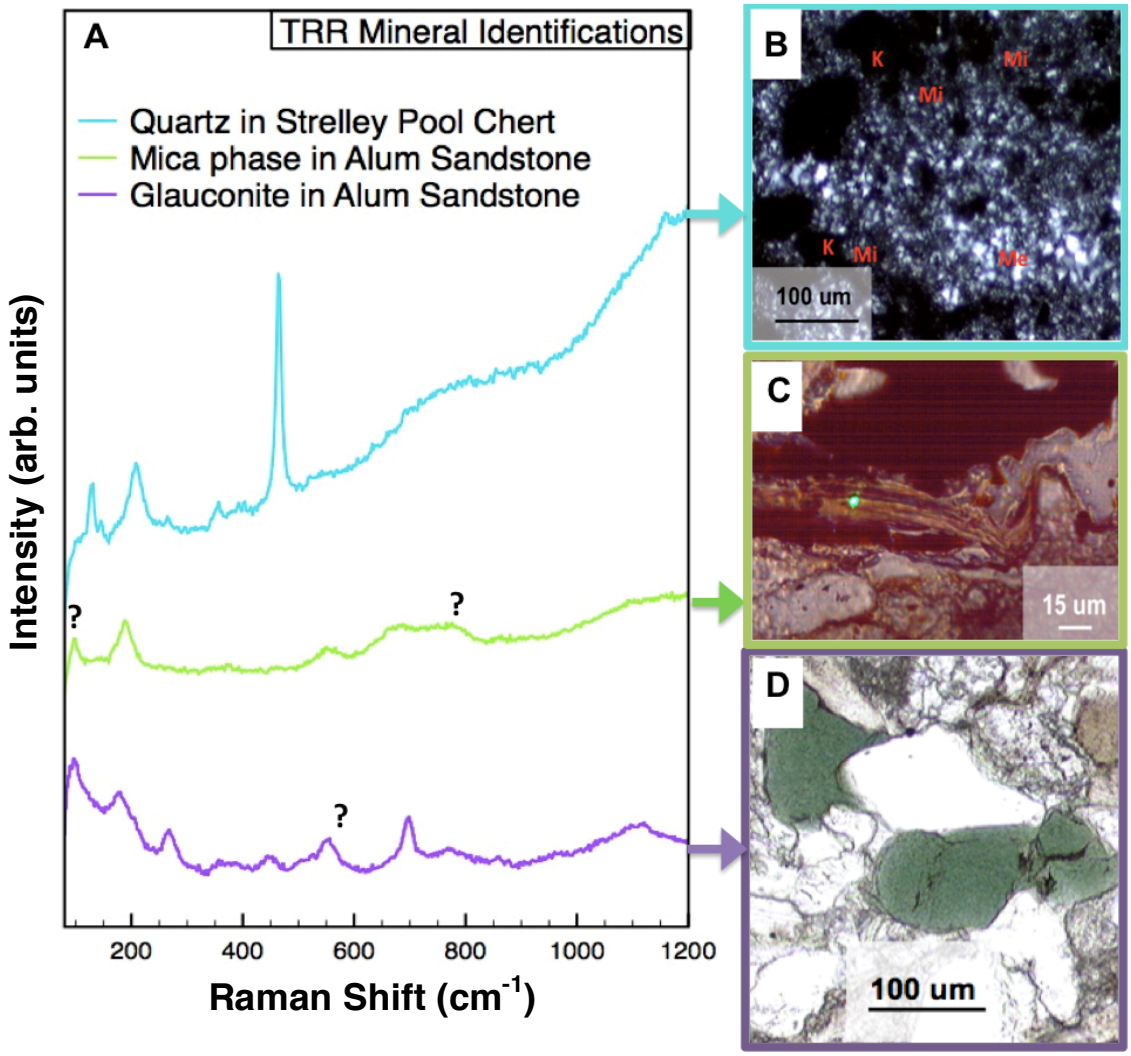

Figure 3.7. Mineral identifications with TRR. **(A)** TRR spectra of three minerals are shown, including quartz from the Strelley Pool chert in the teal spectrum, a mica phase in the Alum sandstone in the green spectrum, and glauconite from the Alum sandstone in the purple spectrum. **(B)** An image of the Strelley Pool chert is seen here in cross-polarized light. Kerogen grains (black patchy areas seen throughout section, labeled "K") are surrounded by microquartz ("Mi"), which appears grey. Patches of megaquartz ("Me") appear lighter. Kerogen was usually associated with microcrystalline quartz, while zones of patchy megaquartz showing less kerogen. (**C**) An image of the sandstone is seen under the TRR's transmitted light imaging system. The image shows a mica grain (see the Table 3.1 for composition details) which has undergone compaction. The Raman laser is on the grain which was interrogated with the TRR instrument to produce the mica spectrum in (A). **(D)** A plane-polarized image is seen here from the Alum sandstone. The green grains were but thought to be glauconite. Their identification was confirmed in TRR, shown by the purple spectrum in A. All unlabeled Raman bands correspond to the identifications given in the legend. Bands with question marks remain unidentified.

Table 3.1

Sample Descriptions and Compositions

Sample	Age	Locality	Component	M	CWR	TRR	XRPD
Calcareous Oil Shale	~56 –34 MYA	Green River, WY	**Calcite**	X	X	X	NP
			Kerogen	X	X	X	
Sulfate Evaporite	~260 – 250 MYA	Castile Fm., Delaware Basin, TX	**Gypsum**	X	X	--	X
			Dolomite	X	X	X	
			Calcite	X	X	--	X
			Anhydrite	X	X	--	
			Nitratine	/	--	--	X
			Sylvite	/	--	--	X
			Kerogen	X	X	X	
Siliceous Mudstone	<65 MYA	Gerlach, NV	**Quartz**	X	X	X	X
			Pyrite	X	X	--	X
			Sphalerite	/	X	--	X
			Kerogen	X	X	X	
Hydrothermal Chert	3.43 BYA	Strelley Pool Fm., Pilbara, W. Australia	**Quartz**	X	X	X	X
			Dolomite	X	X	--	
			Pyrite	X	--	--	
			Alunite	X	--	--	
			Kerogen	X	X	X	
Stromatolitic Limestone	<10,000 YA	Walker Lake, NV	**Calcite**	X	X	X	X
			Quartz	X	--	--	
			Albite	X	X	X	X
			Volcanic glass	X?	--	--	
			Kerogen	X	X	X	
Carbonate-Cemented Fluvial Sandstone	~490 to 488 MYA	Alum Fm., Öland, Sweden	**Quartz**	X	--	--	X
			Feldspar (Plagioclase)	X	--	--	X
			Calcite	X	--	--	X
			Pyrite	X	X	--	X
			Glauconite	X	/	X	
			Mica phase*	X	/	X	X
			Illite	X	/	--	X
			Li- and Na-silicates	/	--	--	X
			Alunite	X?	/	--	X?
			Kerogen	X	X	X	

Table 3.1. Instrument abbreviations: “M” denotes microscopy. “CWR” denotes CW Raman. “TRR” denotes time-resolved Raman. “XRPD” denotes X-Ray Powder Diffraction. Detections: “X” denotes a detection; a “/” denotes attempted identification, with resulting non-detection; a “--“ denotes that phase was not targeted with a particular analysis. “Np” indicates not performed. **Bolded** mineral components are relevant to minerals targeted for astrobiology-relevant targets on Mars and which make up the most abundant minerals in the samples studied. *See section 3.3.6 for details on mica phase identification.

3.4. DISCUSSION

The results of this study can be summarized into four findings, addressed below.

Finding 1: Fluorescence often challenges kerogen identifications using CW Raman, especially for carbonate lithotypes.

On Mars, the inability to identify kerogen in carbonate lithotypes (e.g., due to high fluorescence) could lead to errors in the prioritization of samples for MSR. On earth, carbonates, are considered one of the most important targets for preserving a fossil record and on this basis may be regarded as high-priority targets for MSR. Improvements to reduce fluorescence in Raman spectra of carbonates would have importance for improving the fidelity of sample selection for MSR in carbonate lithotypes on Mars. In the carbonate samples studied, high fluorescence often resulted in the failure to identify kerogen (with some exceptions, as in Figure 3.3; (Shkolyar et al., 2012; 2013; 2014a; 2014b; Shkolyar and Farmer, 2013). In the Green River shale sample, fluorescence prevented kerogen identification by CW Raman (Figure 3.2). In this sample, fluorescence may have been contributed by the carbonate matrix (Wang and Mullins, 1997), by the kerogen (Bertrand et al., 1986; Senftle et al., 1987), or by both. Using CW Raman, no D or G band kerogen bands were seen even after varying laser settings for power, integration time, and focus depth. The Green River shale is known to preserve abundant kerogen (Robinson, 1969), and in this sample, optical properties of the grain analyzed were consistent with kerogen, yet this identification was unconfirmed. Fluorescence was also a challenge for kerogen analyses in another carbonate sample, the Walker Lake stromatolitic limestone (Figure 3.5; Shkolyar et al., 2012; 2013; 2014a; 2014b; Shkolyar and Farmer, 2013). (In that case, kerogen was independently suggested by the

filamentous morphology of many grains, consistent with a biological origin.)

This is not surprising, as fluorescence, especially in carbonates, has been long known (Nichols et al., 1918). What these examples illustrate is the importance of investigating effective ways to reduce the impact of background fluorescence in Raman systems being developed for future missions. It is recommended that instrument performance during the development of these systems be evaluated using natural, highly fluorescent samples, such as the organic-rich carbonates discussed here.

Finding 2: The most successful Raman identifications occurred in the quartz-rich, chert lithotypes, which showed low fluorescence.

In contrast to the carbonates in Finding 1, the two quartz lithotypes (Tertiary siliceous mudstone and the Archean chert) showed low fluorescence, providing ideal cases for identification of kerogen and minerals with high confidence.

First, microcrystalline quartz was the best mineral matrix for kerogen and mineral identification by Raman in this study (Shkolyar et al., 2012; 2013; 2014a; 2014b; Shkolyar and Farmer, 2013). This was true despite the different ages and geological environments of the two samples. (Both consisted of a dense microcrystalline quartz matrix, precipitated under hydrothermal conditions.) In both samples, low mineral fluorescence allowed quartz to be easily identified by its main band at 464 cm^{-1} (Figure 3.4C)

Second, both the D and G kerogen bands were also consistently visible in these samples (Figure 3.4D). Comparing the results of kerogen analysis for these two samples also illustrates another important finding: fluorescence also depends on kerogen maturity. Mature kerogen exhibits a low level of laser-induced fluorescence (Schopf et al., 2012;

Bertrand et al., 1986; Wang and Mullins, 1997). In diagenetically mature kerogen, increased concentrations of poly-cyclic aromatic hydrocarbons (PAHs) quench fluorescence (Bertrand et al., 1986). Thus, the high maturity of the Archean chert sample permitted the clearest Raman identifications in both cases (Figure 3.4D).

Further research is recommended to investigate strategies for fluorescence reduction in Raman studies guided by (1) sample-dependent considerations (such as those identified in Findings 1 and 2 above), and (2) science-driven instrument development protocols that optimize designs around results obtained from natural samples (Shkolyar et al., 2012; 2013; 2014a; 2014b; Shkolyar and Farmer, 2013). The previous literature on Raman spectroscopy suggests that so far, the design of Raman systems has not strongly engaged the challenges of natural geological samples (Bartholomew, 2012; 2014). Studies investigating Raman for astrobiology applications often use unrealistic Mars analog samples, such as pure organics mixed with ground rock (e.g., Hooijschuur et al., 2014) or organics isolated from natural mineral matrixes (which are likely to behave differently than kerogen interacting with its matrix). While analog samples are useful in preliminary studies and instrument tests, Raman systems for future astrobiology missions should be optimized to address sample-dependent issues obtained from natural samples, such as those highlighted in this study (Shkolyar et al., 2012; 2013; 2014a; 2014b; Shkolyar and Farmer, 2013).

Finding 3: High Raman laser power and prolonged laser exposure result in unpredictable outcomes in analyses of kerogen and minerals.

In the Raman study presented here, one strategy used to overcome fluorescence in samples was to increase the laser power. While this sometimes enhanced the spectral

signature of phases that were otherwise overwhelmed by fluorescence, the outcome was unpredictable and sometimes caused spurious results such as sample degradation or alteration (Figures 3.5, 3.6; Shkolyar et al., 2012; 2013; 2014a; 2014b; Shkolyar and Farmer, 2013).

CW Raman spectroscopy detection of kerogen in the stromatolitic limestone was difficult and inconsistent, requiring many attempts and settings to identify it successfully (Figure 3.5C). In this case, microscopy clearly showed abundant kerogen was present (Figure 3.5B). Figure 3.5 illustrates the enhancement of kerogen detection in a highly fluorescent sample by increasing laser power. In this case, a filamentous kerogen grain spot was interrogated, beginning with exposures at 1.3 mW. The resulting spectrum showed only a high fluorescence background with no kerogen bands. The same spot was then interrogated with gradually increased powers, again resulting in spectra showing only fluorescence. At 28 mW, both kerogen bands appeared, along with mineral bands for albite and calcite, captured in the laser's sampling volume. This result is attributed to a combination of high laser power and prolonged laser exposure from multiple interrogations of the same spot which burned away the source of the fluorescence (known as photo-quenching; Bozlee et al., 2005). Such sample alteration is common in carbonates containing thermally immature organic matter [C. Marshall, personal communication], such as the stromatolitic limestone.

Figure 3.6 illustrates two cases of sample degradation during Raman spectroscopy analyses: one of kerogen, the other of a mineral. Two grains were targeted with CW Raman spectroscopy based on microscopy analyses: an immature kerogen grain in the sandstone (Figure 3.6A-B) and an unidentified grain in the shale (Figure 3.6D-F). In both

instances, degradation occurred during spectral acquisition. The Raman spectrum of the damaged spot in the sandstone (Figure 3.6C) showed a broad band around 1450 – 1500 cm^{-1} of ambiguous origin, attributed to either kerogen, a degradation product, or a fluorescence artifact. This band was first thought to be attributable to CH_2, CH_3, or COH stretch modes in immature kerogen (Brody et al., 2001; Edwards and Farwell, 1996). However, when viewed together with the spectrum from the shale, that band seemed more likely to be an artifact of either thermal degradation or fluorescence because of its broadness and similar band shape in both spectra. Due to this ambiguity in identification, the identity of both grains in Figure 3.6 remained undetermined, even after many Raman analysis attempts (Shkolyar et al., 2013; 2014a; 2014b; Shkolyar and Farmer, 2013).

Results obtained in this study (Figures. 3.5 and 3.6) highlight the fact that no clear relationships exist between increased power, prolonged laser exposure, Raman band intensity, and organic or mineral thermal decomposition. These relationships are likely to be sample-dependent (Shkolyar et al., 2013; 2014a; 2014b; Shkolyar and Farmer, 2013). (Thermal decomposition with Raman lasers also depends on other factors besides laser power, not discussed here.) Further studies are recommended to understand these relationships to increase confidence in interpreting Raman spectra.

Finding 4: TRR showed a reduction in fluorescence in all cases where it was used, enabling occasional clear identifications of kerogen and minerals in high-priority analog lithotypes for MSR.

Our preliminary results showed that TRR is a promising approach for reducing fluorescence to allow the identification of fluorescent minerals, including minor phases

(Figure 3.7), and kerogen. In every case examined, TRR also achieved the 2-band rule (Som and Foing, 2012) for Raman spectral identification with high confidence.

In the Alum Fm. sandstone, many bands were visible for both the mica phase and glauconite (Figure 3.7A). Glauconite was confirmed with TRR, but not XRPD (due to low abundance) or CW Raman spectroscopy (due to high fluorescence). If glauconite were identified in a Martian rock interrogated using Raman spectroscopy, and if the 1350 cm^{-1} and 1600 cm^{-1} kerogen bands were also present in that sample (which was the case; see Table 3.1), this would be an ideal sample for MSR: indicating both a habitable environment (with a hydrated phyllosilicate) and organic matter as kerogen.

This study and others by Blacksberg et al. (2013; 2014a; 2014b) have developed a growing science case for the continued investigation of TRR spectroscopy for planetary missions to enable identification of minerals and kerogen in diverse, though sometimes challenging, natural samples. An additional Raman-based fluorescence reduction strategy that may be useful to explore further is Raman laser excitation wavelength optimization. Particularly, UV wavelength excitation separates Raman and fluorescence signals (Tarcea et al., 2007), and has been shown in other studies to increase Raman sensitivity (Gaft and Nagli, 2009). Further work should be performed to better understand the potential role of TRR for planetary applications with continued prototype improvements to optimize collection volume, increase sensitivity, and achieve sub-ns time gating (Shkolyar et al., 2013; 2014a; 2014b; Shkolyar and Farmer, 2013).

To quantify the exact gating needed for fluorescence rejection, fluorescence lifetime imaging microscopy (FLIM) may be useful. This technique is commonly used in cell biology (Esposito and Wouters, 2004). However, little is known about the

fluorescence lifetimes for Mars-relevant lithotypes, which vary from sample to sample and between organics (<1-10 ns) and minerals (>10 ns-ms). If the technique can be adapted to petrographic thin section analyses, it may provide quantitative decay lifetimes for kerogen and minerals in geological samples. Such studies could not only inform the TRR gating requirements needed to eliminate fluorescence, but also help characterize matrix minerals and organics present in kerogen in fluorescent samples. FLIM may even prove useful as a fluorescence-based biosignature detection technique.

3.5. CONCLUSIONS

Raman spectroscopy is an effective, non-destructive, *in situ* method for identifying minerals and organics in rocks. This study highlighted the use of Raman spectroscopy in characterizing four major lithotypes that have been given a high-priority for Mars astrobiology and MSR. Sample-dependent issues that can affect data acquisition and analysis were also highlighted. It is important to understand sample-dependent considerations ahead of time and use this information to improve the design of instruments to ensure effective outcomes during missions. The conclusions of this study may help identify practical science-driven requirements for developing any Raman systems for future missions.

This study revealed four major findings that can inform the future development of Raman systems for space missions. First, background fluorescence is challenging for many of the lithotypes considered important for Astrobiology and MSR. In this study, high background fluorescence often challenged confident kerogen identifications in carbonate lithotypes analyzed using CW Raman spectroscopy. In prioritizing samples for

MSR based on Raman spectroscopy, this could lead to false conclusions about the value of a sample for MSR (Finding 1). Some high-priority lithotypes, such as the microcrystalline quartz (chert) samples, showed inherently low fluorescence, allowing for highly confident kerogen and mineral identifications with CW Raman (Finding 2). In this case, kerogen detectability was enhanced by the samples' high diagenetic maturity. Where fluorescence prevented Raman identification, success was sometimes achieved by increasing laser power. This ad hoc strategy proved unreliable, sometimes quenching fluorescence, and other times, beam-damaging samples (Finding 3).

This study recommends continued investigations of sample-dependent issues and science-driven approaches in Raman instrument development for planetary missions. Further studies of fluorescence rejection techniques in Raman systems should aim to understand relationships between Raman laser power, exposure time, Raman band intensity, and the impacts of organic and/or mineral thermal decomposition. Further studies should focus on fluorescence reduction techniques in realistic, challenging natural samples that have a high-priority for MSR, such as wavelength optimization techniques and continued studies with time-gating. Time-resolved Raman has potential to reduce fluorescence in such samples, enabling clear identifications of both kerogen and aqueous minerals in high-priority lithotypes for Mars (Finding 4). Additional studies could also explore wavelength optimization in time-gated Raman systems for fluorescence rejection in challenging, natural Mars analog samples.

CHAPTER 4

FINDING BIOSIGNATURES IN MARS ANALOG SAMPLES USING VISIBLE AND UV-GATED RAMAN SPECTROSCOPY, AND UV TIME-RESOLVED FLUORESCENCE SPECTROSCOPY

4.1. INTRODUCTION

The 2011 Planetary Science Decadal Survey (NRC, 2011) and the 2008 NASA Astrobiology Roadmap (Des Marais et al., 2008) have assigned a high-priority to the goal of searching for past or present Martian life. These documents recommend that the highest priority for the coming decade should be to send a mission to Mars in order to cache a suite of samples containing potential biosignatures of past or present life and return them to Earth. Previous chapters of this dissertation discuss the community's motivations for MSR and biosignature detections.

Detecting evidence of life occur in samples returned to Earth using sophisticated laboratory tools. To maximize the chances of finding biosignatures in collected samples, it is crucial to develop a strategy for *in situ* selection of samples, based on their contextual association with past habitable environments and potential to preserve biosignatures (Farmer and Des Marais, 1999; Farmer, 2012). As a first step toward this goal, NASA's Mars 2020 rover (Mustard et al., 2013) will select and cache samples for later return to Earth. This step highlights the need for studies to develop *in situ* techniques that can meet MSR goals using realistic terrestrial analog samples.

4.1.1. Sample Types Relevant to the Search for Fossil Life

On Earth, the most widespread and abundant biosignature is kerogen, a degraded, macromolecular form of fossilized organic matter. Sedimentary kerogen represents the largest pool of organic matter on Earth: ~10^{16} tons of C compared to ~10^{12} tons as living biomass (Vandenbroucke and Largeau, 2007). Kerogen is commonly captured and preserved in aqueous lithologies, such as silica (cherts), carbonates, sulfates, and mudstones. These lithotypes have long been considered high-priority targets in the search for a Martian fossil record (Farmer and Des Marais, 1999) and provide a logical focus for this study.

Chert is a dense, highly silicified (>95% silica), fine-grained sedimentary rock, whose dense crystalline structure resists chemical weathering (Hesse, 1990). Chert has a prolonged residence time in the crust, making it one of the most common lithotypes for well-preserved microbiotas in the Precambrian record on Earth (Farmer and Des Marais, 1999). Chert, its precursor opaline silica, and a low-pressure, high-temperature polymorph, tridymite, have all been detected recently at Mars rover landing sites (Skok et al., 2010; Ruff et al., 2011; Morris et al., 2016).

Carbonates such as calcite ($CaCO_3$) are also common host minerals for Earth's Precambrian fossil record (Farmer and Des Marais, 1999). Carbonates have been detected on Mars both from orbit (Ehlmann et al., 2008b) and from the ground (Madden et al., 2004; Morris et al., 2010). Detections of various Martian carbonates, including Mg-carbonate, or magnesite ($MgCO_3$), suggest that ancient aqueous solutions on Mars included a range of pH conditions, some of which may have been habitable.

Hydrated calcium sulfate (gypsum; $CaSO_4 \cdot H_2O$), another common lithotype preserving a kerogenous microfossil record, is considered a promising target in the search for past life on Mars (Schopf et al., 2012). Gypsum and other hydrated sulfates have been observed both from orbit (Bibring et al., 2006; Glotch and Rogers, 2007) and *in situ* by rovers (Squyres et al., 2004; Glotch et al., 2006; Squyres et al., 2012) in various forms, including components of soils and evaporite deposits.

Fine-grained mudstones, particularly those containing hydrated aluminum phyllosilicates (clays), are another lithotype commonly targeted for organic biosignatures on Earth. Clays are produced by the aqueous weathering of preexisting rocks or by authigenic *in situ* precipitation. Phyllosilicate-rich rocks have a high potential for capturing and preserving organic matter (Farmer and Des Marais, 1999; Ehlmann et al., 2008b) because on Earth, organic compounds adsorb as molecular monolayers on clay surfaces. Clays, including smectites, have been identified on Mars from orbit (Ehlmann et al., 2008b; Noe Dobrea et al., 2012) and by rovers (Vaniman et al., 2014; Bristow et al., 2015).

4.1.2. Raman Spectroscopy

According to the report of the Mars 2020 Science Definition Team, or SDT (Mustard et al., 2013), material returned from Mars will likely be restricted to ~30 samples with a total mass of <500 grams. *In situ* instrument analyses will select the most promising samples for Earth return. One such instrument is Raman spectroscopy. This light-scattering, vibrational spectroscopy technique is discussed further in Chapter 3.

Raman spectroscopy has a long history of terrestrial analyses of both organic and

mineral compounds. These include non-destructive, *in situ* assessments of extant endolithic biomarkers (Dickensheets et al., 2000; Jorge-Villar and Edwards, 2013), kerogenous microfossils in ~3.5 Ga cherts (Brasier et al., 2002; Schopf et al., 2002; Marshall et al., 2011), and carbon in ~3.87 Ga samples (Schidlowski et al., 1979; Mojzsis et al., 1996). See Chapter 3 for additional information. Debates about these analyses have emphasized that the detection of kerogen with Raman alone does not prove biogenicity. This is because Raman features of biogenic kerogen can be similar to disordered abiotic carbonaceous materials (Brasier et al., 2002; Pasteris and Wopenka, 2003; Marshall et al., 2010).

Such debates indicate that assessing the biogenicity of organic matter may be as challenging for samples returned from Mars and that understanding sample context is crucial for assessing potential biogencity. For accurate interpretations, information about both mineralogy and microtexture is necessary, as recognized by the Mars 2020 SDT (Mustard et al., 2013). Compositional information from Raman spot analyses may be placed within a spatial context provided by microscale imaging. Consistent with this strategy, samples were characterized at the microscale by thin section petrography to interpret how paragenesis and diagenesis affect mineralogy, microtexture, and kerogen preservation. This micro-spatial framework provided context for selecting optimal spots for Raman analyses.

In the Raman spectrum, kerogen is identified by two bands that represent the phonon modes (quantized vibrational modes that depend on the arrangements of atoms in condensed matter) of diagenetically mature or maturing macromolecular carbon. Spectral features consist of a “D band,” and “G band,” discussed in Section 3.1.3. D and G bands

can be deconvolved to many sub-bands, both in UV (Czaja et al., 2009) and visible (Marshall et al., 2010) Raman spectra. When D and G bands are present, additional low-intensity features can be present in the 2400–3300 cm^{-1} region. Such bands represent second-order sp^3 C-H_x stretch modes of bands in the 1100–1800 cm^{-1} region (Ferrari and Robertson, 2001 and references therein). Detecting combinations of these bands in a Martian sample would provide evidence that this sample bears organic matter, making it a strong candidate for caching and MSR. After return to Earth, detailed laboratory analyses would then be used to assess the biogenicity of samples.

One main challenge with Raman spectroscopy is interfering fluorescence, often several orders of magnitudes stronger than the Raman scattering signal. Fluorescence is discussed in more detail in Chapter 1 and Chapter 3 section 3.1.5. Many minerals and complex organics exhibit fluorescence at overlapping wavelengths with their Raman signatures.

Strategies to mitigate fluorescence interference include resonance Raman (Frosch et al., 2007), confocal Raman (Brasier et al., 2002) and shifted-excitation Raman difference spectroscopy, or SERDS (Shreve et al., 1992). One strategy explored in this study, as well as in Chapter 3, is time-gating (hereafter, gating). Gating uses pulsed laser excitation and gated detection (i.e., detection of only those photons scattered or emitted during the laser pulse) to capture the ~instantaneous Raman-scattered photons and gate out the long lifetime fluorescence signal in the time domain (Martyshkin et al., 2004; Gaft and Nagli, 2009). This is contrasted by continuous wave, or CW, Raman in which the laser continuously irradiates the sample without laser pulsing or gating.

Another strategy to reduce fluorescence which is explored here is application-specific optimization using laser excitation wavelength (λ_{ex}) in the UV. UV λ_{ex} causes Raman and fluorescence signals to become energetically and spatially separated (Tarcea et al., 2007), and the Raman sensitivity to become increased (Gaft and Nagli, 2009). Depending on the wavelength and targeted compound, UV λ_{ex} also has the advantage of inducing resonance within electronic bands of certain organics classes including biogenic carbon (Hug et al., 2005; Marshall et al., 2010 and references therein) and complex organics such as kerogen (Czaja et al., 2009). Resonance can increase scattering efficiency by orders of magnitude, from ppm (Beegle et al., 2015) to ppb levels (Storrie-Lombardi et al., 2001), resulting in organics detection with higher confidence. This also means that organic surface (~10s of nm) contamination signals can be amplified (Ray et al., 2000; Ferrari and Robertson, 2001).

On the other hand, laser-induced time-resolved fluorescence can present advantages for organic analysis. When examined in spectral and temporal domains (Gaft and Panczer, 2013), decay lifetimes can provide useful information about the nature of the sample (Figure 4.1). Fluorescence can arise from inorganic sources, such as lattice defects, trace metals, or rare-Earth impurities with lifetimes >1 μs, or from organic chromophores, with lifetimes of ≲100 ns (Sharma et al., 2003; Bozlee et al., 2005). Complementary gated, UV Raman and fluorescence data sets can be obtained on the instrument at the same micro-scale regions of a sample, without moving the sample from the stage. This is possible by interchanging spectrometer gratings, each optimized for a particular wavelength range.

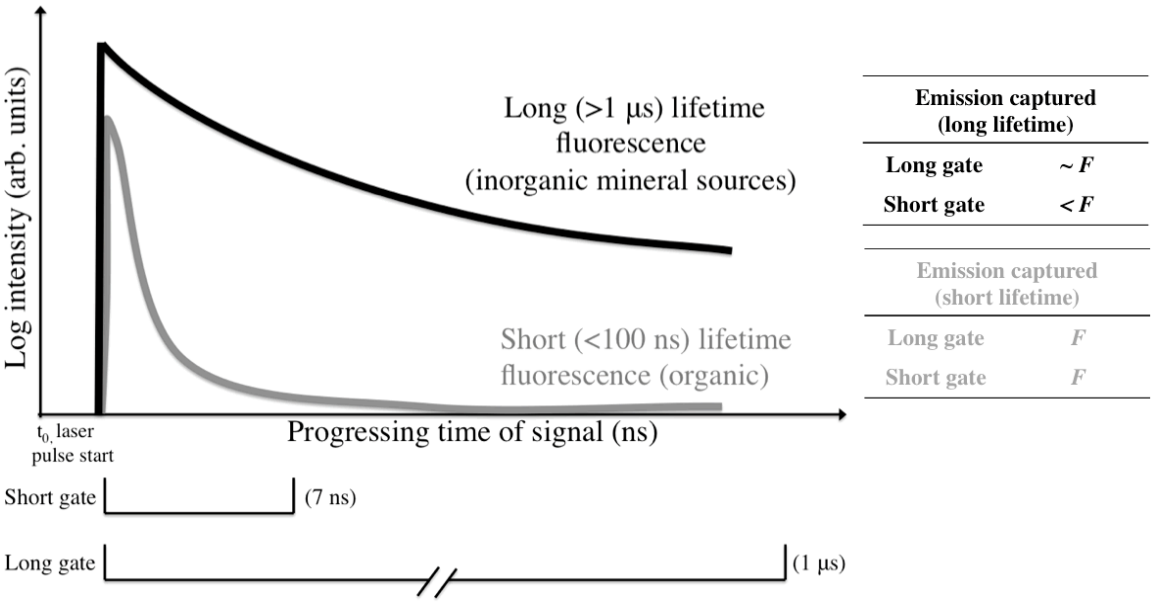

Figure 4.1. Principles of time-resolved fluorescence. Fluorescence emission is exponential for a single excited state. *F* is the arbitrary fluorescence emission of a sample after interaction with one laser pulse, measured by the detector, represented as a function of detector gate width. Inorganic materials emit long-lifetime fluorescence (shown in black); a long gate would capture almost the full emission (~*F*), but a shorter gate would capture less than the full emission (< *F*). Organics emit short-lifetime fluorescence (shown in grey). Both long and short gates would capture the majority of the signal (*F*). The gate widths shown here were used in this study's experimental setup.

Neither UV/VIS Raman nor fluorescence spectroscopy have not yet flown to Mars, but the European Space Agency (ESA) and NASA Mars Program are both planning to include payloads using these technologies in upcoming missions. ESA's ExoMars mission, scheduled for launch in 2018, includes a 532 nm CW Raman Laser Spectrometer (RLS) to perform *in situ* biosignature analyses (Bost et al., 2015). The payload of NASA's Mars 2020 rover includes two Raman and fluorescence instruments. One is the Scanning Habitable Environments with Raman & Luminescence for Organics & Chemicals instrument (SHERLOC), an arm-mounted, resonance Raman (810-3600 cm^{-1} range) and fluorescence (245-360 nm range) spectrometer, with a deep UV 248.6 nm laser source (Beegle et al., 2015). The second is SuperCam, an integrated suite of four

instruments, including a stand-off spectrometer with gated (≲100 ns) excitation at λ_{ex} = 532 nm for Raman (between 50 - 4400 cm^{-1}) and fluorescence (between 534-850 nm) measurements (Clegg et al., 2015). A priority of both SHERLOC and SuperCam is to identify samples containing potential organic biosignatures for caching and sample return. This study is motivated by the need to inform biosignature caching strategies by obtaining visible and UV Raman and fluorescence data sets similar to what is obtainable with these two instruments. Raman-based fluorescence reduction is explored in this study using similar techniques as those implemented by SHERLOC and SuperCam (i.e., gating and UV λ_{ex} optimization).

Several studies have assessed the capabilities of Raman and fluorescence instruments for biosignature detection, including the system used in this study (Eshelman et al., 2014; 2015; Skulinova et al., 2014). However, few have examined complex biosignatures expected on Mars, such as non-extracted kerogen in natural samples. In light of upcoming missions to seek signs of past life on Mars, it is crucial that Raman performance be tested and methods optimized using naturally occurring samples representative of what could be encountered on Mars.

4.1.3. Objectives of this Study

This study is motivated by the need to inform biosignature caching strategies using visible Raman, UV Raman, and UV fluorescence data sets. A diverse suite of samples representing habitable environments and known to favor biosignature preservation (discussed above) is explored in this study in order to address three goals:

1. *Assess the effectiveness of time-gating compared to UV laser excitation wavelength optimization as a Raman-based fluorescence reduction strategy to enable successful caching of samples for MSR.*
2. *Identify sample-specific issues which could challenge identifications of samples using the two Raman spectroscopy systems discussed above; and*
3. *Assess the capabilities of UV laser-induced time-resolved fluorescence spectroscopy for detecting kerogen in the sample suite studied.*

This study is organized as follows. In Section 2, methods are described which used two Raman-fluorescence spectrometer instruments: a CW Raman (V-CW) with λ_{ex}=532 nm and a UV gated (UV-G) Raman and UV laser-induced time-resolved (UVLITR) fluorescence combined system with λ_{ex} = 266 nm. This study's methods were guided by petrographic microscopy interpretations of mineralogy, microtextures, and kerogen preservation. In Section 3, results for each sample and analytical data are summarized. In Section 4, the impacts of fluorescence interference on the ability to characterize minerals and kerogen and sample-dependent issues encountered with both Raman systems are discussed. Also discussed are the capabilities of fluorescence spectroscopy to detect organics in samples. Section 4 concludes with a table (Table 4.2) which summarizes this study's results corresponding to the above three goals. Section 5 concludes with a discussion of how these findings may impact the Mars 2020 Raman and fluorescence instruments and offers recommendations for continued work on Raman and fluorescence biosignature studies for MSR.

4.2. METHODS

4.2.1. Instrument Analyses

Seven samples were selected to represent a broad range of depositional environments, ages, and diagenetic histories. All samples contained natural, non-extracted kerogen of diverse maturities and modes of preservation within their host matrices. Samples included a hydrothermal chert; a siliceous mudstone; a carbonate-cemented marine sandstone; a laminated sulfate-carbonate evaporite; a lacustrine stromatolitic limestone; a lacustrine micritic carbonate; and a clay and magnesite-rich evaporitic mudstone. Sample localities, ages, and compositions are summarized in Table 4.1. For each sample, five data sets were collected using polarizing light microscopy, V-CW Raman spectroscopy, UV-G Raman spectroscopy, UVLITR fluorescence spectroscopy, and X-ray powder diffraction (XRPD).

4.2.1.1. Petrographic microscopy

For polarizing light microscopy and 532 nm Raman analyses, standard (30-µm thick) petrographic thin sections were prepared by Spectrum Petrographics, Inc. Samples were vacuum-embedded in EPOTEK 301 epoxy. Thin-section microscopy provided a basis for identifying the depositional setting, and documenting diagenetic processes. This included the reconstruction of a paragenetic (time-ordered) framework for minerals, microtextures, and organic matter. Thin sections were imaged using a Nikon Eclipse E600 POL polarizing microscope and an Optronix digital camera system. For each field of view, photomicrographs were obtained under transmitted (plane- and cross-polarized)

and reflected light illumination. Rock chips were used for UV-G Raman and fluorescence analyses and imaged under reflected light.

Identifications of minerals and kerogen were based on a process involving alternating between optical illumination settings to identify mineral phases and kerogen in thin sections. For instance, dark to black kerogen can be mistaken for Fe-oxides in plane- or cross-polarized light, but only an Fe-oxide is reflective in reflective light. Kerogen grains were targeted in regions expected to preserve abundant kerogen (i.e., in microcrystalline quartz regions in the chert sample, detailed in Figure 4.2). Major and minor mineral components were documented, along with representative microtextural features (i.e., kerogen-rich, darker laminations). Primary and secondary (authigenic) mineral components were distinguished based on paragenetic relationships (i.e., later-stage recrystallization textures). Cross-cutting relationships in petrographic observations were used to reconstruct paragenetic relationships.

Optical screening of samples allowed the location of features and phases which were then targeted for Raman and fluorescence spectroscopy spot analyses. Small markers were adhered onto thin section and on rock chip surfaces to mark the locations of kerogen and mineral grains for interrogation with Raman and fluorescence spectroscopy. This allowed the tracking of the regions of interest identified under microscopy to precise locations for spectroscopy analyses. Using this iterative approach, the identities of marked kerogen and mineral regions based on microscopy could be confirmed by Raman point analyses. This approach also enabled the placement of minerals, microfabrics, and

kerogen grains into a petrogenetic and paragenetic framework for assessment of preservation potential and caching priorities.

4.2.1.2 V-CW Raman spectroscopy

A laboratory V-CW Raman spectroscopy system at ASU's Center for Solid State Science was used to obtain point spectra for the kerogen and mineral grains. This micro-Raman system uses a 532 nm Coherent Sapphire SF laser source and a Princeton Instruments liquid nitrogen cooled CCD detector and Acton 300i spectrograph. The laser was focused onto the sample using a 50X APO Mitutoyo objective. The system has a spectral resolution of ~2 cm^{-1}, spatial resolution of ~0.5 μm, a 1200 lines/mm grating, and an acquisition window from 70-2000 cm^{-1}. Data were acquired using a 180° geometry.

Raman point spectra were acquired from uncovered thin sections on previously identified mapped kerogen and mineral grains as described above. Raman shift positions were calibrated using a cyclohexane standard. A built-in transmitted light microscope was available, making it possible to locate regions of interest and markers on samples for interrogation (as shown in Figure 4.6B). The Raman laser spot (<5 μm diameter) was manually focused on the sample surface. Spectra were acquired over a range of integration times, power settings, and depths below the thin section surface to obtain the optimal signal (with the least fluorescence, the highest signal to noise ratio, and the most Raman bands visible). Acquisitions ranged from one to twenty 10- to 15-second integrations at 0.75- 6 mW power for each analysis (unless otherwise noted in figure captions). Powers were manually controlled using a neutral density filter wheel.

Sampling depths were 1-20 μm below thin section surfaces. No background correction was applied. Mineral identifications were obtained using the *CrystalSleuth* software (Downs, 2006).

Care was taken to avoid contamination during Raman analyses. Non-fluorescent thin section epoxy was used in preparing thin sections. Contamination from epoxy was dismissed because no spectral features from the epoxy-embedded samples were seen in Raman data. Contamination from the adhesive markers on samples was avoided by cleaning each thin section with 95% ethanol and distilled water. In addition, the Raman optical imaging system was used to position the laser beam to miss the markers.

4.2.1.3. 266 nm gated Raman and UVLITR fluorescence spectroscopy

UV radiation absorption from thin section components (glass slides and embedding epoxy) significantly weakens the Raman signal. For this reason, polished sample chips were used instead for UV-G Raman and UVLITR fluorescence analyses. To prepare sample surface for analysis, the surface interrogated was ground flat using aluminum oxide abrasive paper (400 grit, Northon St. Gobain Premium #2612) to avoid surface organic contamination for all but the hardest samples (chert and siliceous mudstone). Microscopy confirmed that no abrasive paper contaminants were present on the ground surfaces analyzed. Thin sections are unlikely to be used on upcoming missions, so abraded rock surfaces represent an analogous sample preparation scenario for what will be possible on Mars using a RAT (Gorevan et al., 2003).

A 266 nm pulsed laser Raman and laser-induced, time-resolved fluorescence spectroscopy system with a gated, intensified CCD (iCCD) detector was used to obtain time-resolved Raman and fluorescence point spectra on all samples.

Four data sets were obtained on representative regions in each sample on targeted kerogen and matrix mineral locations without moving samples from the stage: (1) Raman spectrum, long gate (to mimic a non-gated 266 nm CW Raman system); (2) Raman spectrum, short gate (to understand the effectiveness of gating as compared to non-gating); (3) fluorescence spectrum, long gate; (4) fluorescence spectrum, short gate. Short and long gate widths were 7 ns and 1 μs, respectively. Raman measurements were acquired with a 2400 lines/mm grating, allowing an acquisition window from 286-3805 cm^{-1}. Raman spectra were acquired for 10 min.

Before each sample acquisition, a dark current spectrum (with the input to the spectrometer blocked) was acquired, followed by a calibration spectrum of an alanine powder standard. A flat field correction was performed using a NIST deuterium lamp standard (which had a linear response between 266 and 300 nm in the Raman data presented here) to remove the effect of any CCD irregularities (as well as the edge filter irregularities). (This method was used since a wavelength dependent florescence standard was unavailable from NIST.)

For fluorescence measurements, the Raman spectrometer grating was interchanged with a 300 lines/mm grating with a window from 268-528 nm. Time-resolved fluorescence spectra were obtained by acquiring fluorescence in the wavelength, time, and intensity domains, at 0.1 ns gate steps and 10 s integration times over 20 ns.

The laser spot size was measured to be ~25 x 35 μm. Other system details are given in Eshelman et al (2015).

UV-G Raman and fluorescence data sets were acquired on the following mineral standards: Silica sand standard (Barco 49, 99.7% SiO2); gypsum (Sigma Aldrich lot #SLBC4109V); dolomite (Wards research grade, 49-5871 Selasvann, Norway); and calcite (Wards research grade, 49-5860 Chihuahua, Mexico). For a kerogen standard, 1 mg of extracted kerogen (94% C) was used, courtesy of R. Summons' group (MIT).

4.2.1.4. X-Ray powder diffraction

For XRPD analyses, bulk, powdered samples were obtained for each sample for confirmation of mineralogy determined by the other analyses. (Kerogen cannot be identified using XRPD.) Bulk samples were chipped, crushed, ground using a quartz mortar and pestle, and sieved to 150 μm.

A Siemens D5000 X-ray Diffractometer with a Ni-filtered Cu radiation source was used to identify minerals present in bulk sample powders. Powders were scanned from 5° to 81.759° with a step size of 0.016303º. Operating conditions were 40 kV at 30 mA using CuKα ($\lambda_{\alpha 1}$ = 1.5060 Å; $\lambda_{\alpha 2}$ = 1.54439 Å) with an 8-second dwell time, for a total analysis time of 12 hours per sample. Background subtraction and mineral identifications were performed using the *JADE*™ software, version 9 (Materials Data, Inc.), with the International Centre for Diffraction Data (ICDD) database.

4.2.2. Analytical Methods

UV Raman excitation has the potential to induce resonance within aromatic carbon compounds at low abundances in samples, including contaminants (Ray et al., 2000; Ferrari and Robertson, 2001; Asher, 1993). The G band seen in UV-G Raman spectra may be attributed to either kerogen or aromatic contaminants. Addressing goal 1 of this study required the differentiation between kerogen signals and contamination. For this, a *S/N* thresholding method was developed. Kerogen regions were defined and marked with a sticker based on evidence for kerogen in microscopy. Both matrix regions and suspected kerogen grains were interrogated using UV-G Raman. Raw spectra were baseline-flattened according to Dyar et al. (submitted). The *S/N* of the G band was computed using a custom MATLAB routine such that:

$$S/N = I/\sigma \quad (1)$$

where I is the intensity of the G band and σ is the standard deviation of the 3742-3842 cm^{-1} range in each spectrum (were Raman bands were absent). Spectra which contained kerogen bands that may have been confused for contaminants were omitted from this analysis to avoid skewed results.

To address goal 3, fluorescence decay lifetimes were extracted on a subset of samples using a partial least-squares regression method detailed in Eshelman et al. (2015).

4.3. RESULTS

4.3.1. Summary of Each Sample

Details for each sample are summarized below. Table 4.1 summarizes all phases found in each sample with the techniques used.

Table 4.1

Sample Compositions With Ages, Localities, and Phases Detected.

Sample	Approx. Age	Locality	Component	M	V-CW	XRPD	UV-G
Hydro-thermal Chert	<3.43 BYA	Strelley Pool Fm., Pilbara, Australia	**Quartz**	X	X	X	X
			Dolomite	X	X		
			Pyrite	X			
			Alunite	X			
			Kerogen	X	X		X
Siliceous Mudstone	≤ 65 MYA	Gerlach, NV	**Quartz**	X	X	X	X
			Pyrite	X	X		
			Sphalerite	X?	X	X?	
			Kerogen	X	X		X
Marine Sandstone	~490 to 488 MYA	Alum Fm., Öland, Sweden	**Quartz**	X		X	
			Feldspar (Plagioc.)	X		X	
			Dolomite				X
			Calcite	X		X	
			Pyrite	X	X	X	
			Glauconite	X			
			Mica*	X		X	
			Illite	X		X	
			Kerogen	X	X		X
Sulfate Evaporite	300–250 MYA	Castile Fm., Delaware Basin, TX	**Gypsum**	X	X	X	X
			Dolomite	X	X		
			Calcite	X	X	X	X
			Anhydrite	X	X		
			Sylvite			X	
			Kerogen	X	X		X
Stromato-litic Limestone	<10,000 YA	Walker Lake, NV	**Calcite**	X	X	X	X
			Quartz	X			
			Albite	X	X	X	
			Kerogen	X	X		X
Lacustrine Carbonate	~56 –34 MYA	Green River, WY	**Calcite**	X	X	X	X
			Dolomite			X	
			Volcanic ash?	X?			
			Kerogen	X	X		X
Evaporitic Mudstone	7.5-2.5 MYA	Verde Valley, AZ	**Magnesite**	X		X	
			Feldspars (Na, Ca, K)	X	X		
			Quartz	X	X	X	
			Gypsum	X	X	X	
			Thenardite	X	X	X	
			Glauberite	X	X		
			Arzakite	X	X		
			Iron oxides**	X	X		
			Muscovite	X	X	X	
			Montmorillonite			X	
			Saponite (Fe, Mg)			X	
			Kerogen				

Table 4.1. Abbreviations are as follows: Transmitted light microscopy (M); visible CW Raman (V-CW); X-ray Powder Diffraction (XRPD); and gated UV Raman (UV-G).

Bold minerals are high-priority astrobiology-relevant targets on Mars (Farmer and Des Marais, 1999) and the most abundant phases in the sample.
*Ambiguities in identification of this phase is attributed to intermediates not well captured in existing Raman spectral libraries (i.e., muscovite/phlogopite in this case).
**Near-IR spectroscopy confirmed the presence of hematite, goethite, and lepidocrite (Shkolyar and Farmer, in preparation; see Chapter 2.).

4.3.1.1. Archean hydrothermal chert, Strelley Pool Fm., Pilbara, Australia

The Strelley Pool Formation is a stratiform, limestone-chert sequence that hosts the oldest known coniform stromatolites. It is thought to have been deposited in a shallow marine environment during the Archaean (Lowe, 1980; Hofmann et al., 1999; Van Kranendonk et al., 2003; Allwood et al., 2006). The sample analyzed for this study was collected from a vein of black chert that is part of a younger system of dikes that cross-cuts the Strelley Pool Fm. at the Trendall locality. This sample is dominated by a fine-grained matrix of microcrystalline quartz grains, confirmed by all techniques (Figure 4.2; Table 4.1), surrounding abundant, particulate kerogen (Figure 4.2A). During diagenesis, microcrystalline quartz coarsened, forming localized patches of megaquartz (>20 μm grains; Figure 4.2A). During diagenesis, syngenetic carbonate was replaced by silica (and vice versa). Other mineral phases identified are listed in Table 4.1. Most kerogen in this sample was found within regions dominated by microcrystalline quartz, while zones of megaquartz showed a lower kerogen abundance (Figure 4.2A).

Using V-CW Raman, kerogen in this sample was confidently identified due to its low overall fluorescence (Figure 4.2B). UV gated Raman identified quartz and the kerogen D band, plus second-order kerogen bands, with high confidence (Figure 4.2B). It also confirmed kerogen and quartz in all attempts with both Raman instruments, even when only one was targeted.

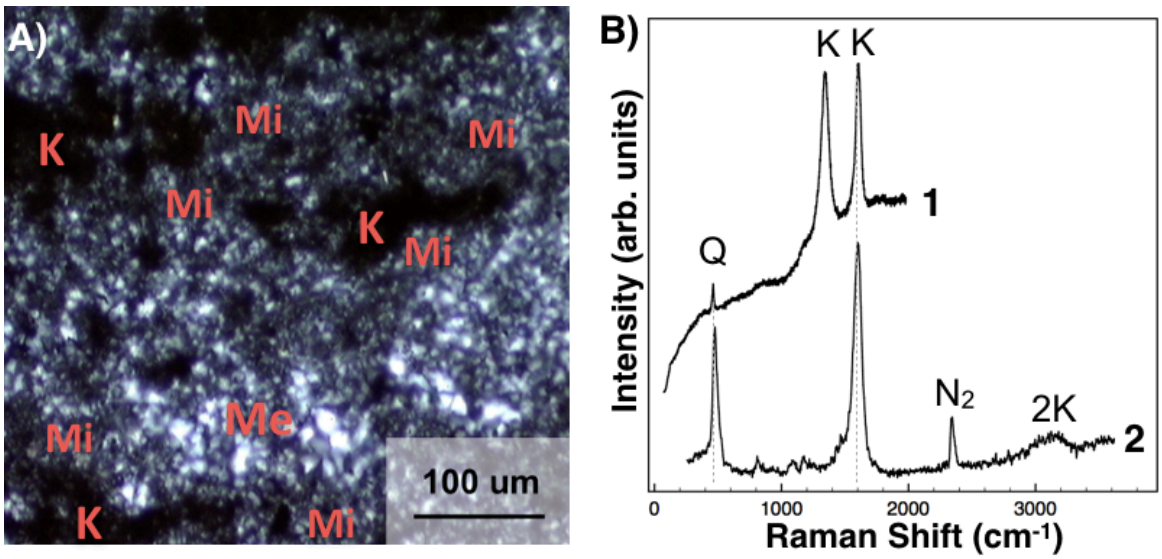

Figure 4.2. Hydrothermal chert analyses. **(A)** Cross-polarized photomicrograph of the Strelley Pool chert. Black kerogen grains ("K") are surrounded by greyish micro-crystalline quartz ("Mi"). Patchy megaquartz ("Me") regions appear white. **(B)** Spectrum 1 shows low background fluorescence which allowed the detection of both the main quartz band ("Q") at 464 cm^{-1}, as well as kerogen (D and G bands) preserved within it. A UV gated Raman spectrum (short gate) is shown of a similar region (Spectrum 2). Spectrum 2 shows a G band and a second-order band for kerogen ("2K") in the 2900–3300 cm^{-1} region, as well as a quartz band. N_2 indicates atmospheric nitrogen at 2331 cm^{-1} (Hug et al., 2005).

4.3.1.2. Tertiary siliceous mudstone, Wind Mt. Mine, Gerlach, Nevada

The Wind Mt. mine exposes a dark grey to black, siliceous mudstone. The host rocks at Wind Mt. mine were subject to intense geothermal activity associated with pervasive silicification and the emplacement of shallow epithermal gold deposits (Wood, 1991; Eneva et al., 2011). Mineralization included the precipitation of sulfide minerals. For example, pyrite (FeS_2) was identified with several techniques, often associated with kerogen (Figure 4.3, Table 4.1).

Microscopy revealed that a structureless mudstone matrix was replaced by micro-crystalline quartz (Figure 4.3A). Quartz, the most abundant phase, was detected using all techniques (Figure 4.3; Table 4.1). The sample contained abundant organic matter and

plant fossils. Microscopy revealed kerogen as particulate grains (Figure 4.3A) as well as morphologically distinct plant fragments (Figure 4.3B). The well-preserved morphology of the fossil plant biota contrasts with the amorphous, opaque, mature kerogen.

Using V-CW Raman, the presence of kerogen, quartz, and pyrite were confirmed in most spectra, despite some moderate fluorescence (Figure 4.3C, spectra 1 and 2). The ambiguous evidence for kerogen in spectrum 2 is due to fluorescence and the fact that quartz, not kerogen, was targeted for spot analysis. With UV-G Raman, first- and potentially second-order bands associated with kerogen were identified, as well as the main quartz vibrational band (Figure 4.3C, spectrum 3). Overall, the association of kerogen with the quartz-rich matrix was visible in all UV-G Raman spectra and in some V-CW Raman spectra.

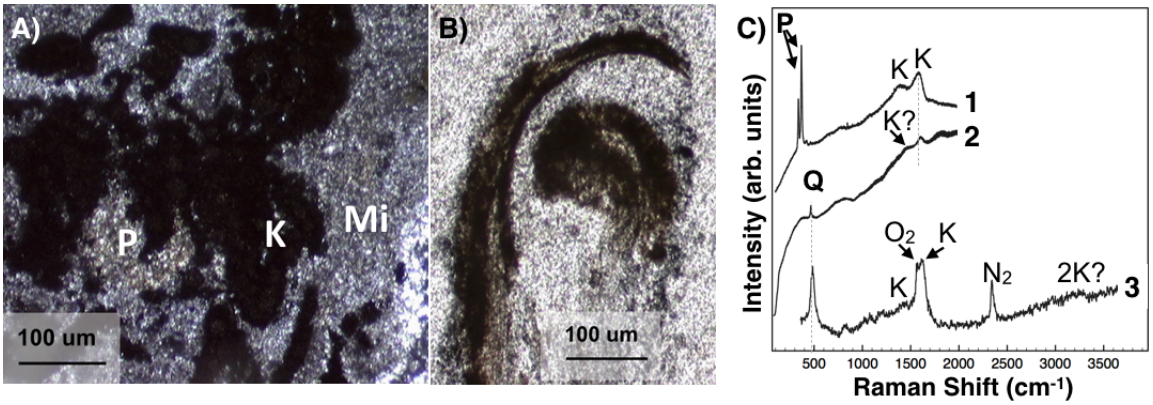

Figure 4.3. Siliceous mudstone analyses. **(A)** Cross-polarized light photomicrograph with a region of black kerogen and brassy pyrite ("P"), surrounded by microcrystalline quartz. **(B)** Plane-polarized light photomicrograph showing a possible plant fragment. **(C)** V-CW Raman spectra (1 and 2) and a UV gated Raman spectrum (spec. 3) are shown. Kerogen is associated with pyrite (spectrum 1). A quartz-rich matrix is also shown with weak kerogen bands (spectrum 2). The UV short gate Raman spectrum of a region targeting the matrix shows kerogen (D and G band plus a possible second-order band) preserved in a quartz-rich matrix. The 1556 cm^{-1} ("O_2") band is attributed to atmospheric oxygen (Hug et al., 2005) and convolved with a kerogen band. Abbreviations are as noted previously.

4.3.1.3. Upper Cambrian carbonate-cemented marine sandstone, Alum Formation, Öland, Sweden

The sample analyzed here is a fine-grained quartzo-feldspathic Cambrian age sandstone cemented by carbonate from the Alum Formation (Maeda et al. 2001). Several phyllosilicates, (see Table 4.1) such as glauconite $(Fe^{3+},Al,Mg)_2(Si,Al)_4O_{10}(OH)_2$, were identified in this sample. Various micas (see Table 4.1 for details) were also present in moderate abundance, often associated with kerogen as deformed grains due to compaction (Figure 4.4A). Microscopy revealed that the sandstone contains abundant kerogen (Figure 4.4A-B), usually identifiable in V-CW Raman analyses using high power, with moderate fluorescence (Figure 4.4D). Pyrite (FeS_2) occurred primarily as framboids (Figure 4.4B-C), which some studies suggest are biomediated (Popa et al. 2004). In this sample, pyrite is often detected in association with kerogen (Figure 4.4C and D), confirmed by V-CW Raman (Figure 4.4B) and XRPD (Table 4.1), and seen in similar samples (Thickpenny, 1984).

With UV-G Raman, first-order kerogen bands were detected with high confidence and second-order kerogen were also captured but with less certainty (Figure 4.4D). Even though UV-G Raman data were taken on kerogen and a matrix region including kerogen in its sampling volume, fluorescence seemed higher in the kerogen-rich spot versus in the matrix region (Figure 4.4D). Second-order kerogen bands were less clearly visible due to their weak intensity and fluorescence past 2000 cm^{-1}. Dolomite $[CaMg(CO_3)_2]$, present as the cementing phase, was weak but detectable with UV-G Raman.

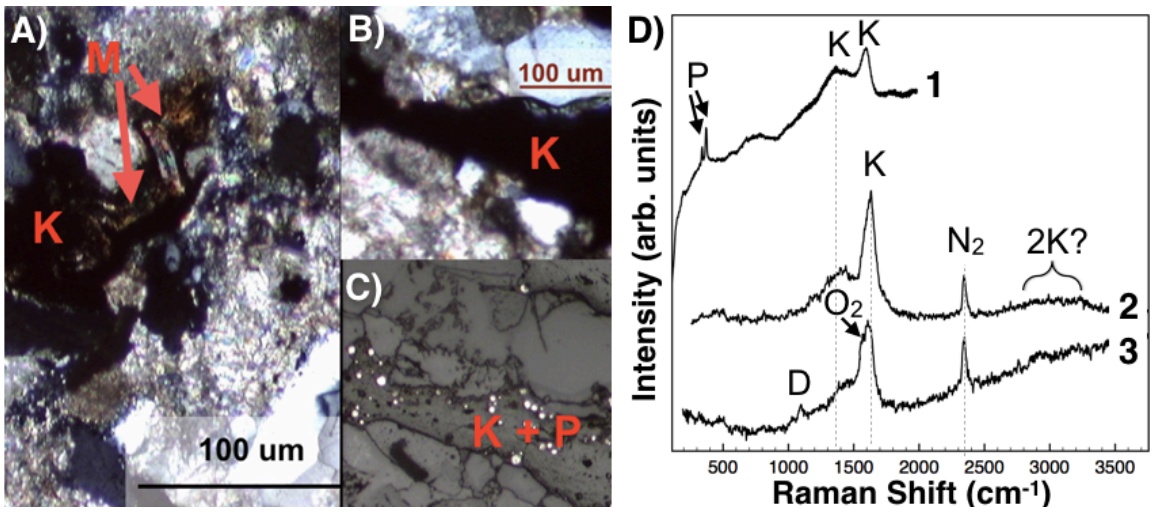

Figure 4.4. Marine sandstone analyses. **(A)** Kerogen ("K") was associated with an unidentified mica phase ("M"), evident by its high birefringence colors and platy appearance, seen here in cross-polarized light. **(B)** A large region of kerogen is seen in between a quartz-rich and feldspar-rich matrix, cemented by carbonate, seen in plane-polarized light. **(C)** In reflected light, the same kerogen-rich region as in (B) is rich in pyrite, which appears shiny. **(D)** A representative V-CW Raman spectrum is shown (spectrum 1), taken at 12 mW power. A moderately fluorescent Raman spectrum confirms the association of kerogen with pyrite. Two UV gated Raman short gate spectra are also seen (spectra 2 and 3), obtained on matrix and kerogen-rich regions, respectively. First and ambiguous second-order kerogen features are indicated in both spectra. A weak dolomite band ("D") was seen at 1093 cm^{-1} (spec. 3). Abbreviations are as noted previously.

4.3.1.4. Permian sulfate evaporite, Castile Formation, Delaware Basin, Texas

The Castile Fm. is a calcium sulfate evaporite deposit exposed in the Delaware Basin. The formation was deposited during the late Permian as a deep-water evaporite, with primary anhydrite ($CaSO_4$) nucleating in the water column then settling to the bottom of the basin to form a laminated (varved) sulfate-carbonate deposit (Anderson et al., 1972). Subsequent uplift of the Basin exposed primary anhydrite to near-surface groundwater, where it hydrated to form secondary gypsum. This resulted in a volume change and compressional folding of laminae. Dark laminae are composed of fine-grained, organic-rich carbonate mud (micrite) as dolomite and calcite; lighter laminations

are composed of coarser, euhedral crystals of gypsum and anhydrite (Figure 4.5A). Additional phases are listed in Table 4.1.

In thin sections analyses, dark, carbonate-rich laminae contain abundant fine-grained kerogen surrounded by dolomite (Figs. 5C). Kerogen was sometimes identified using V-CW Raman, along with anhydrite and dolomite (Figure 4.5C). Due to high fluorescence, multiple attempts using very high power settings (up to 28 mW) were required for clear kerogen identification with V-CW Raman. In contrast, with UV-G Raman, kerogen and the matrix minerals (gypsum and/or calcite) were confidently identifiable in dark laminae (Figure 4.5B).

UV-G Raman spectra in matrix regions of dark laminae where kerogen grains were not targeted often produced a weak, broad G band. This is attributed to surface or airborne organic contaminants high in aromatic components. This was determined after quantifying *S/N* for kerogen across all samples (Methods section 2.2; Figure 4.9). See Sections 4.3.2 and 4.4 for details.

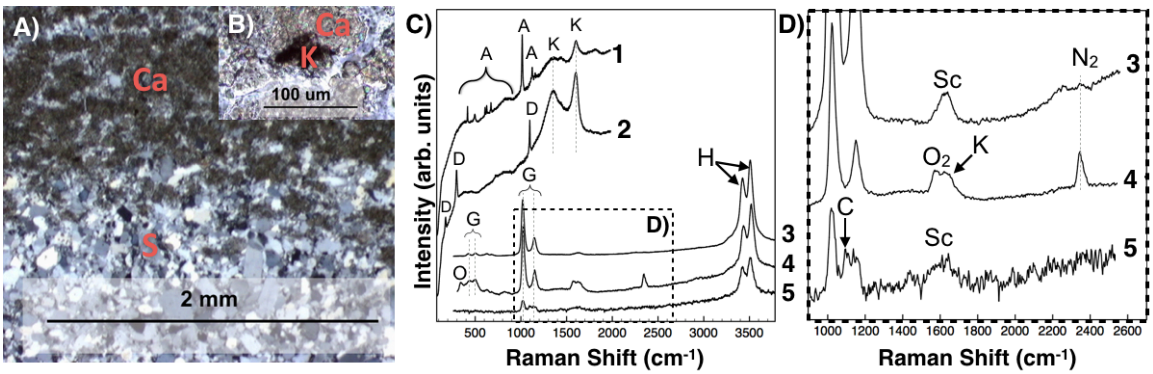

Figure 4.5. Sulfate evaporite analyses. **(A)** Cross-polarized light photomicrograph. A carbonate- ("Ca") and sulfate-rich laminations ("S") are shown. Sulfate grains appeared black, grey, or white depending on their extinction. **(B)** Cross-polarized light photomicrograph of a kerogen grain preserved in carbonate interrogated with V-CW Raman (spectrum shown in C). **(C)** V-CW Raman spectra of sulfate (spectrum 1) and a carbonate laminations (spectrum 2). Both laminations show the D and G bands when kerogen was targeted. Dolomite (175, 299, and 1095 cm^{-1}) surrounds the kerogen grain pictured in (B). Anhydrite ("A") was detected at 415, 497, 608, 625, 672, 1017, 1128, and 1160 cm^{-1} in sulfate laminations. Spectrum 1 was taken with 28 mW power. Three UV-G Raman spectra are shown: a short gate gypsum ("G") lamination (spectrum 3), a short gate kerogen region (spectrum 4), and a long spectrum with both calcite ("C") and gypsum bands identified (spectrum 5). "H" indicates H_2O stretch modes (3430 and 3500 cm^{-1}), common in hydrated sulfates (Wang et al., 2006). **(D)** Dashed plot: region magnified in (C). "O" indicates Raman quartz objective interference. "Sc" denotes a surface contaminant (see Figure 4.9). Other symbols are as noted previously.

4.3.1.5. Holocene stromatolitic limestone (Carbonate), Walker Lake, Nevada

The stromatolitic limestone analyzed was collected from a terrace along the western shoreline of Walker Lake (Osborne et al., 1982). It consists of alternating dark and light laminae of microcrystalline calcite (Figure 4.6A). Dark laminae contained more kerogen than lighter laminae, which appeared well-preserved as irregular patchy aggregates and filamentous microfossil forms (Figure 4.6B). Carbonate presence was inferred with microscopy; calcite was confirmed as the main phase with both Raman and XRPD (Table 4.1). Detrital grains of quartz and plagioclase feldspar were also present abundantly in carbonate (light-toned) laminae.

V-CW Raman caused highly fluorescent kerogen to be detectable but with ambiguity and difficulty, often after multiple experimental tries and elevated laser powers (Figure 4.6C). UV gated Raman detected calcite and kerogen in all attempts (Figure 4.6C).

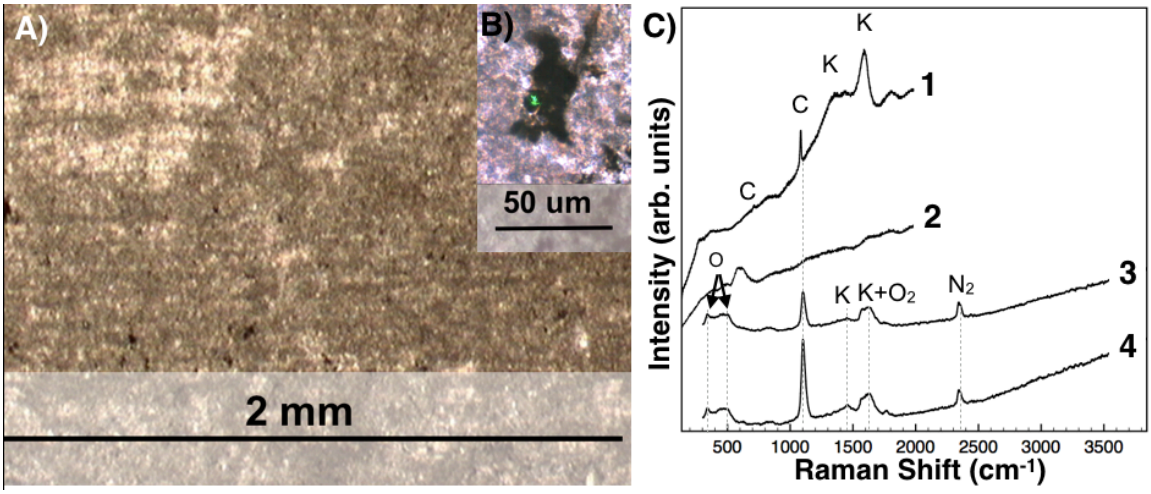

Figure 4.6. Stromatolitic limestone analyses. **(A)** A plane-polarized light image is seen of carbonate-rich (light) and organics-rich (dark) laminations with interruptions of lighter, patchy recrystallized carbonate regions visible. **(B)** The transmitted light imaging on the V-CW Raman imaging system captured a filamentous and irregular kerogen cluster preserved in a fine-grained calcite matrix. The location of the green laser spot is visible where V-CW Raman spectra in (D) were obtained. **(C)** Two V-CW Raman spectra were acquired for the kerogen grain shown in (B). Spectrum 2 shows the lowest power setting attempted for this sample (1.3 mW). No kerogen D or G bands or host matrix bands were seen. (The broad 600 cm^{-1} band is unidentified.) The same location was interrogated with systematically increased power settings. It revealed calcite (at 1086 cm^{-1}) and both D and G kerogen bands at 28 mW (spec. 1). UV-G spectra of both the organic-rich (spec. 3) and carbonate-rich (spec. 4) laminations confirmed kerogen present in a calcite-rich matrix. Abbreviations are as noted previously.

4.3.1.6. Eocene lacustrine carbonate, Green River Formation (GRF), Wyoming

The Green River Formation has various members with different compositions and textures (e.g., Surdam and Stanley, 1979). The sample analyzed here is from a lacustrine

limestone member. Limestone formed by precipitation of fine-grained (micritic) carbonate as calcite and dolomite, within the water column, which later settled to the lake bottom.

This sample shows both microscopic particulate kerogen surrounded by a carbonate-rich matrix (Figure 4.7A) and macroscopic preservation of fossils. High background fluorescence precluded identification of the carbonate matrix minerals using V-CW Raman. This was the case for all power settings tried (Figure 4.7B spectrum 2). After multiple attempts with increasing power levels, kerogen was detectable with high certainty despite fluorescence (Figure 4.7B, spectrum 1). All kerogen bands (D and G bands and weak 2nd order bands) and their calcite matrix were detectable with confidence with UV-G Raman (Fig. 4.7B spectrum 5).

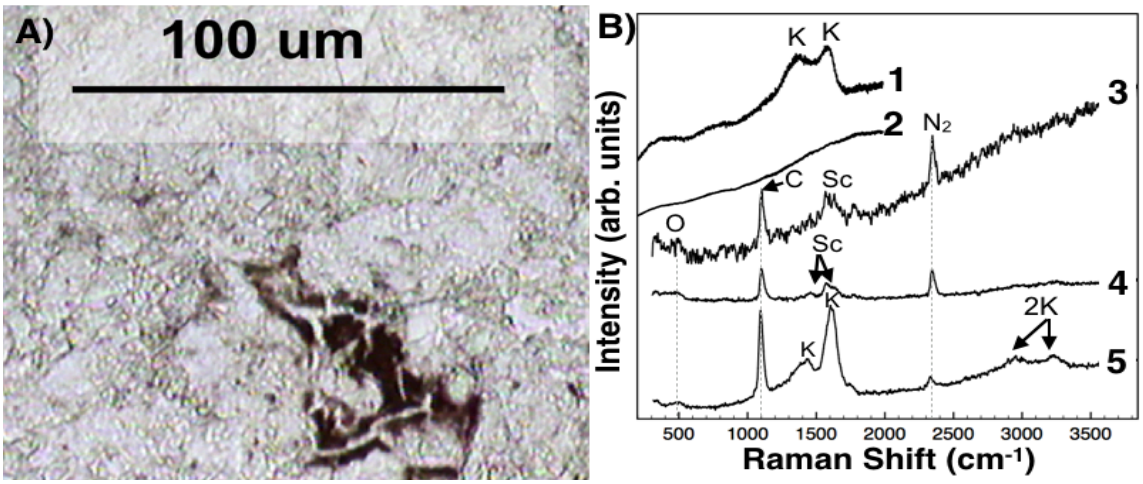

Figure 4.7. Lacustrine carbonate analyses. **(A)** Plane-polarized light imaging showed a fine-grained carbonate preserving dark regions of kerogen. **(B)** Spectrum 1 shows a representative V-CW Raman spectrum for D and G kerogen bands along with a matrix region in spectrum 2. The mineral matrix (Spec. 2) did not reveal any Raman information. Two UV-G Raman spectra are shown for a matrix region in spectrum 3 (long gate) and spectrum 4 (short gate). Surface contaminants (Figure 4.10) were visible in matrix spectra. Spectrum 5 is a short gate kerogen-rich region. Calcite is visible in all UV-G Raman spectra. Both D and G bands, as well as second order bands for kerogen are detectable in this kerogen spectrum. Symbols are as noted previously.

4.3.1.7. Miocene-Pliocene evaporitic mudstone, Verde Basin, Arizona

The clay-rich evaporitic mudstone analyzed is from the Miocene-Pliocene Verde Formation in Verde Basin (from Chapter 2). The rocks sampled were deposited in a playa lake setting that experienced episodic deposition of evaporites within playa muds (Bressler and Butler, 1978; Nations et al., 1981 and references therein). This mudstone consists of a carbonate-rich mud matrix (as magnesite) containing primary gypsum that grew displacively within the mud, forming abundant crystal clusters. A variety of coarse, detrital grains were abundant in the matrix (Figure 4.8A). The mudstone is also rich in clays (i.e., muscovite mica, as in Figure 4.8B, saponite, and montmorillonite). Suspected kerogen was seen with microscopy throughout the mudstone matrix in moderate abundance (Figure 4.8C). Microscopy also revealed the presence of clasts with rust colored, iron-rich alteration rims (Figure 4.8C) and other iron oxide phases such as hematite, goethite, and lepidocrite (Shkolyar and Farmer, in preparation; Figure 2.4). For complete details on this sample, see Chapter 2.

V-CW Raman analysis revealed only fluorescence when the mudstone matrix and kerogen regions were interrogated, regardless of acquisition settings (Figure 4.8D). However, V-CW Raman provided useful identifications of other phases in the matrix which had low fluorescence (Table 4.1). UV-G Raman analyses did not reveal compositional information (Figure 4.8D).

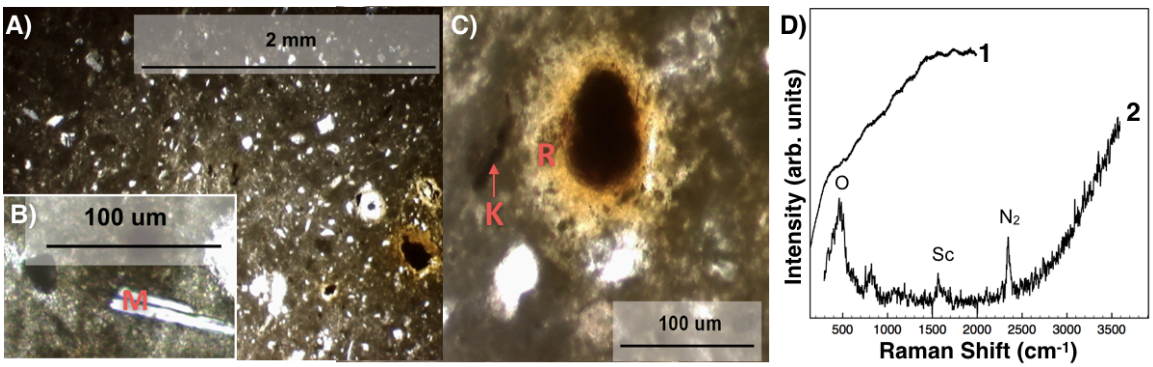

Figure 4.8. Evaporitic mudstone analyses. **(A)** A plane-polarized light photomicrograph is shown of the fine-grained clay-rich and magnesite-rich matrix with abundant detrital grains visible (e.g., quartz and feldspar). **(B)** Many coarse-grained platy micas were visible in the matrix. **(C)** A black clast is shown, with a hazy orange rim ("R") visible. A suspected kerogen grain is also indicated. **(D)** Spectrum 1 shows a representative V-CW Raman spectrum, revealing only wavy noise. Spectrum 2 shows a representative short gate UV-G Raman spectrum, revealing no compositional information about the sample, either. Other symbols are as noted previously.

4.3.2. Analytical Results

In a Raman spectrum, a G band would commonly be expected in kerogen (Pasteris and Wopenka, 2003; Marshall et al., 2010). In UV-G Raman spectra, a weak G band was evident in many cases where kerogen was not targeted (Figs. 5, 7, and 8). Here, the band is attributed to aromatic surface contaminants with a Raman mode at ~1600 cm^{-1} (Ray et al., 2000; Ferrari and Robertson, 2001), mimicking a kerogen band.

A method was developed (section 2.2) to quantify and distinguish the *S/N* of a true G band in UV-G Raman spectrum versus a weak G band due to contamination. Fig. 9 presents the results. A clear threshold emerged in the detection of kerogen detection using UV-G Raman and the suite of samples studied. The *S/N* threshold value, 12, is indicated at the lowest true kerogen band value, occurring in the siliceous mudstone. Where evidence of kerogen at the spot interrogated was confirmed by microscopy, those

spectra were found to have a *S/N* >12, *irrespective* of acquisition parameters. In spectra with *S/N* < 12, the weak G band signal is attributed to the presence of airborne or surface contaminants rich in aromatic carbon. The detection of these contaminants is attributed to selective UV resonance Raman vibration enhancement of aromatic organics (Ferrari and Robertson, 2001; Hug et al., 2005; Asher, 1993) where individual resonant organic species are not (and need not be) identifiable. See Discussion, section 4.4, for details.

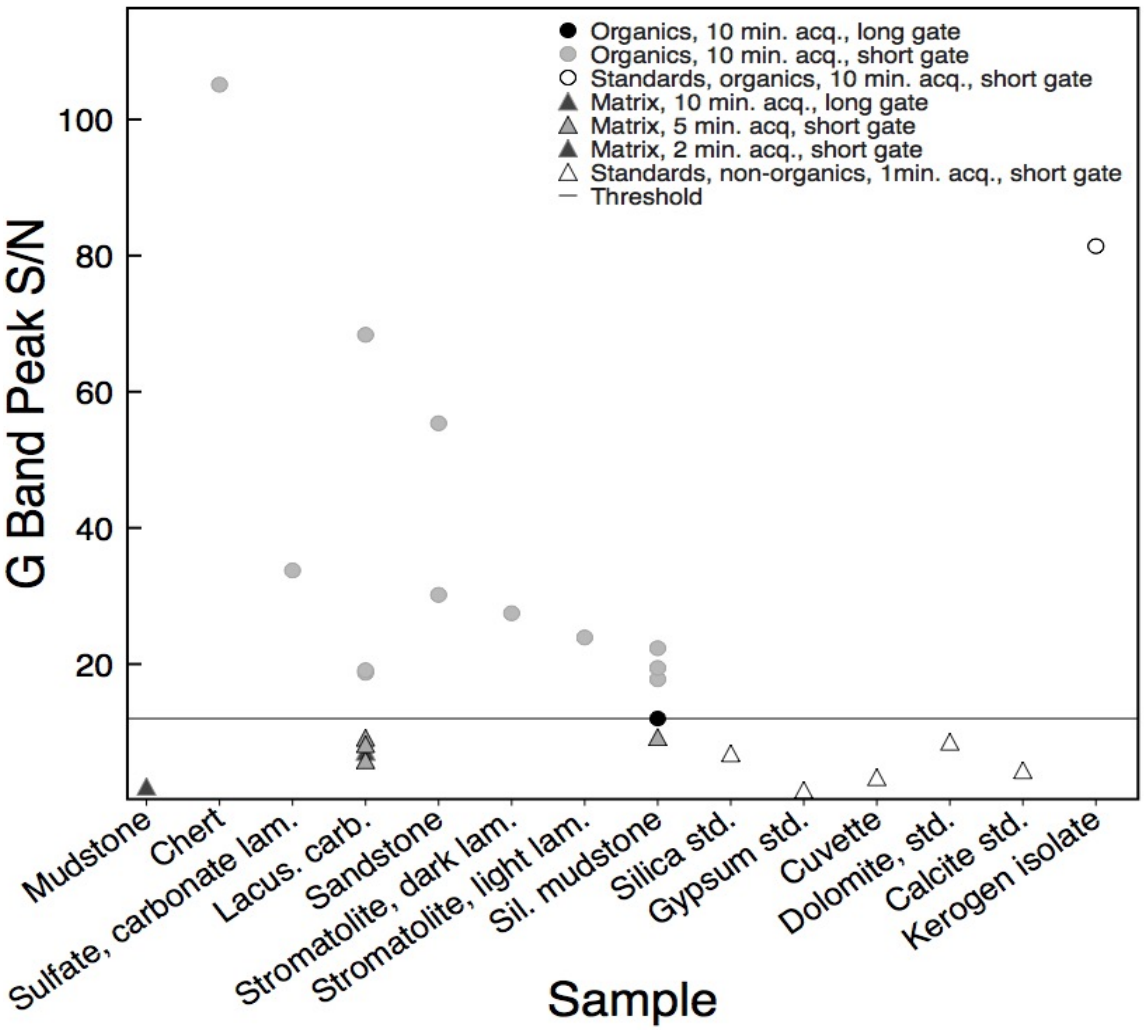

Figure 4.9. S/N in G band of UV-G Raman spectra. *S/N* values (equation 1) are shown for the G band appearing in true kerogen (circles) and matrix (triangles) regions in samples and standards. Acquisition parameters are noted in the legend using various shadings. Standards are not shaded. The *S/N* threshold value, 12, is indicated by a line at the lowest G band value. An empty plastic cuvette is added for comparison.

Goal 3 was addressed in Figure 4.10, which summarizes the UVLITR fluorescence results. Two categories of organic fluorescence patterns were revealed. Type 1 organics spectra (Figure 4.10A) were grouped based on the similar morphology of the 407 - 475 nm band in samples (spectra 1-4) and in the kerogen standard (spectrum 5): the band is broad and centered around ~430 nm. These spectra were acquired on kerogen

grains identified by microscopy and confirmed with UV-G Raman before fluorescence interrogation, except for spectrum 1. (Spectrum 1 was acquired on a targeted matrix region but where kerogen was evident in most analyses with both Raman systems.) Type 2 fluorescence spectra (Figure 4.10B) showed a combination of at least two bands with peaks at 415 nm and (less intensely) 430 nm. This fluorescence appeared in spectra where kerogen was not targeted or visible on the surface during Raman or microscopy analyses (hence the "matrix" label). In addition, these spectra differ from that of the kerogen standard (Figure 4.10A spec. 5). A sticker marker displayed fluorescence similar to Type 2 samples (Figure 4.10B, spec. 6), with the addition of a feature at ~510 nm, not seen in any samples. While Type 2 spectra were all acquired on carbonate and sulfate lithotypes, spectra also differ from those of synthetic carbonate and sulfate standards. Those standards also showed weak fluorescence at 400 - 450 nm (Figure 4.9C). (One exception is the dolomite standards, in Fig. 4.10C spectrum 4, which display type 2 organic features, consistent with a contamination explanation.)

Fluorescence decay lifetimes were extracted on the 407-475 nm feature from both organics categories in samples whose fluorescence peak feature (short gate) is marked with an asterisk in Figure 4.10A-B. The lifetime of the peak in the spectra analyzed was $\lesssim$5 ns in all cases investigated. (Further sensitivity on multi-component organic compounds was limited by the method used, which assumed single-component decays.) See Section 4.3 for discussion.

Fluorescence features ranging from 300 to 400 nm were also visible (Figure 4.10A, spectra 3-4; Figure 4.10B spectrum 5). These were observed in long but not short gate spectra, suggesting long decay lifetimes consistent with inorganic sources (Figure

4.1). This could not be confirmed with accurate calculations of inorganic lifetimes because these features were convolved with organic bands.

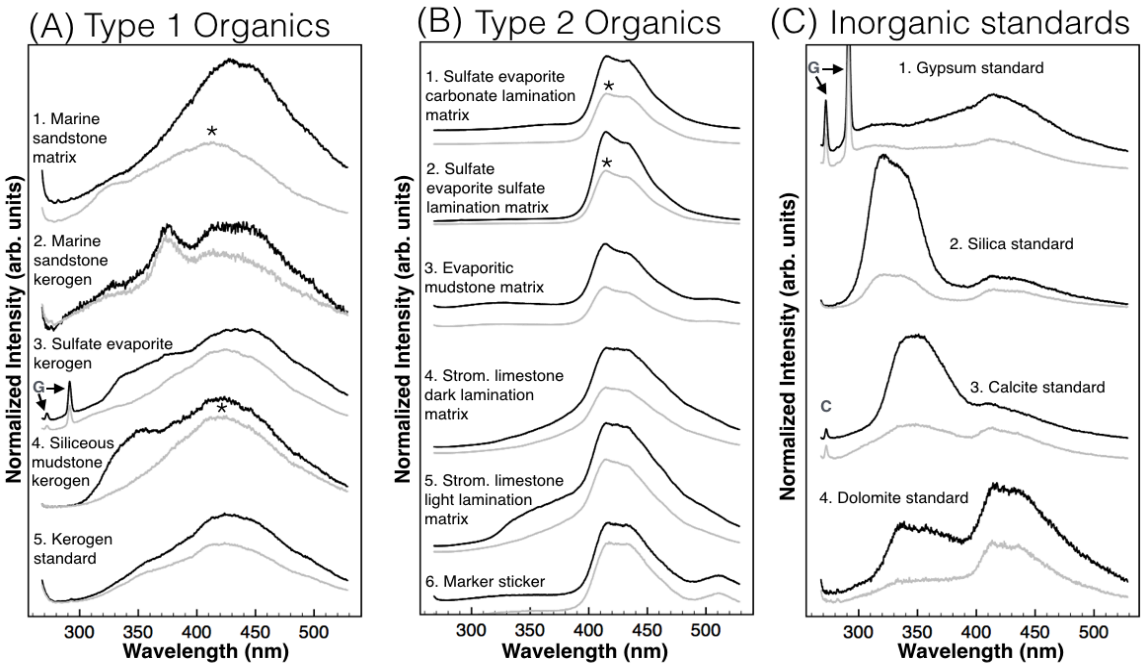

Figure 4.10. Fluorescence spectra of organic and inorganic components. Black and grey spectra indicate long and short gates, respectively, acquired on the same spots. Fluorescence spectra attributed to **(A)** Type 1 organics, **(B)** Type 2 organics, and **(C)** synthetic mineral standards are shown. Sharp bands below 300 nm are Raman bands from calcite ("C") or gypsum ("G"). All intensities are offset and normalized for clarity and comparison.

4.3.3. Summary of Results

Table 4.2 presents a summary of the goals investigated (defined in the Introduction) in relationship to each sample.

Table 4.2

Summary of Results by Sample Corresponding to Study Goals

Sample	Goal 1	Goal 2	Goal 3
Hydrothermal Chert	• Lowest fluorescence (kerogen and matrix) • No florescence mitigation necessary	• Mature kerogen and silica lithotype caused low fluorescence. • Ideal for kerogen and matrix identification with both Raman systems.	• Type 1 organics identified (kerogen and matrix region)
Siliceous Mudstone	• Moderate fluorescence (kerogen and matrix) • Higher success in kerogen detection with λ_{ex} =266 nm	• Low fluorescence in silica lithotypes enabled clear detections (both Raman systems). • Ideal for kerogen and matrix identification with both Raman systems.	• Type 1 organics identified (kerogen region)
Marine Sandstone	• Moderate fluorescence (matrix) • High fluorescence (kerogen) • No florescence mitigation necessary	• Carbonate-cemented sandstone fluorescence did not impede either Raman analysis	• Type 1 organics identified (matrix and kerogen regions)
Sulfate Evaporite	• Moderate to high fluorescence (kerogen and matrix) • Higher success in kerogen detection with λ_{ex} =266 nm	• Carbonate laminations: most fluorescence and difficulty with V-CW Raman. • Sulfate laminations: moderate, non-impeding fluorescence	• Type 1 organics identified (kerogen regions) • Type 2 organics (carbonate an sulfate laminations)
Stromatolitic Limestone	• High, impeding fluorescence (kerogen and matrix) • Higher success in kerogen and mineral detection with λ_{ex} =266 nm	• Carbonate lithotype caused the most fluorescence and difficulty with V-CW Raman analyses, improvement with UV-G Raman.	• Type 2 organics identified (carbonate and organic-rich laminations)
Lacustrine Carbonate	• Impeding fluorescence in carbonate • High fluorescence in kerogen • Higher success in mineral detection with λ_{ex} =266 nm • Short gating improved *S/N*	• Carbonate lithotype caused the most fluorescence and difficulty with V-CW Raman analyses.	• Type 1 organics identified (matrix region) • Type 2 organics (kerogen region)
Evaporitic Mudstone	• High fluorescence • No success in kerogen and mineral detection with either Raman	• Carbonate lithotype caused impeding fluorescence with V-CW Raman. • Metal-rich matrix caused impeding UV absorption with UV-G Raman	• Type 2 organics identified

Table 4.2. See text for details.

4.4. DISCUSSION

4.4.1. Raman-Based Fluorescence Reduction

This study sought to assess the effectiveness of gating compared to optimizing λ_{ex} as Raman-based fluorescence reduction strategies to enable successful caching of samples for MSR based on their kerogen content and mineralogy (goal 1). **Compared to V-CW Raman, UV-G Raman allowed mineral and organic identifications with higher reliability in this sample suite.**

In general, fewer attempts and higher success rates of kerogen detection were achieved when targeting a kerogen grain with the UV-G Raman system. As long as kerogen was visible on the surface, it could be confirmed with UV Raman on the first acquisition, without the trial and error required using the V-CW system. This was true even considering challenging location of regions for analysis on sample chips: the transmitted light imaging system on the V-CW system allowed faster location of target regions in thin sections as compared to the same task using reflected light on chips analyzed with the UV-G system.

With V-CW Raman, fluorescence sometimes impeded the detection of matrix minerals (e.g., stromatolitic limestone), whereas with UV-G Raman, fluorescence reduction was achieved in all cases except the evaporitic mudstone (see sample-specific discussion, Section 4.2). UV-G Raman showed the most significant improvement on the detectability of the fluorescent matrix of the lacustrine carbonate (Figure 4.6B).

UV-G Raman spectra of kerogen could be obtained from all samples (except the evaporitic mudstone; see Section 4.2) and are consistent with those of Czaja et al. (2009), who investigated fossil ferns with a λ_{ex} = 244 nm UV Raman. Both G and D bands were

present in all samples where kerogen was targeted. One exception is the chert, in which the lack of a D band is attributed to the sample's high thermal maturation. This caused kerogen "graphitization," evident by the fact that the UV-G Raman chert spectrum (Figure 4.2D) is similar to that of ordered graphite (Tuinstra and Koenig, 1970). In addition to the D and G bands, broad, low-intensity second-order kerogen features were sometimes revealed (Figs. 2B, 7B, and less confidently in Figure 4.3C and 4D).

Kerogen was not the only organic material identified with UV-G Raman. Many UV-G matrix spectra often showed a weak G band (Figs. 5D, 7B, and 8D), which occurred when kerogen was not targeted or visible in microscopy observations. A *S/N* thresholding analysis was performed on the G band in UV-G Raman spectra (Fig. 9). Consequently, the weak G band to aromatic surface contaminants were detectable due to resonance enhancement of Raman vibrational modes of aromatic organic species (Ray et al., 2000; Ferrari and Robertson, 2001) at trace abundances on sample surfaces, even after careful preparation, handling, and polishing. Although identifying or quantifying the contaminants was outside the scope of this study, this result highlights the need to further understand potential organic contaminants that may affect rover-based analyses (e.g., rocket fuel, cosmogenic organics, etc.). This result also suggests that SHERLOC, a UV Raman system with a range of 810 cm^{-1} to ~3600 cm^{-1}, is suited to detect all Raman bands associated not only with kerogen (1350 cm^{-1}, 1600 cm^{-1}, and 2900–3300 cm^{-1} bands) but also other organics, especially at low abundances, and without being impeded by fluorescence interference.

The higher efficiency and level of certainty in identifications with UV-G compared to V-CW Raman could be due either to λ_{ex} optimization or to gating. To isolate

the effect of λ_{ex} on fluorescence reduction, spectra of the same samples taken with the V-CW Raman and long gate UV-G Raman were compared. Using the UV-G system in long gate mode mimicked a CW acquisition, leaving λ_{ex} as the only fluorescence mitigation variable. It was found that λ_{ex} optimization had more impact than gating on fluorescence mitigation. Long gating and λ_{ex} = 266 nm enabled the clearest matrix mineral detections on the first attempt, as exemplified by the lacustrine carbonate sample, in Figure 4.7B (and many other spectra not shown): in the main kerogen and mineral region, between 400 and 1800 cm^{-1}, kerogen and minerals could be seen under UV excitation (Figure 4.6C, 7B), unimpeded by fluorescence below 2000 cm^{-1}, whereas V-CW Raman spectra were often overwhelmed by fluorescence. Short gating reduced fluorescence and improved S/*N* compared to long gating on the same sample spot. It did not otherwise affect spectral interpretations.

To isolate the effects of gating, UV-G spectra and varied gate lengths were acquired to quantify the resulting *S/N* (See Appendix A and Figure A.1 for method) on a subset of samples. The shorter the gate (and laser pulse), the more effective gating became. Short gating (5 ns) was appropriate with gated UV Raman instruments for detecting kerogen and matrix minerals. A 5-ns gate allowed the identification of kerogen and matrix minerals and allowed us to quantify fluorescence removal (see Appendix A). Fluorescence removal at two different Raman signal strengths, 50% and 80%, was examined (Table A.1). Fluorescence was reduced by 50% or more in all cases investigated. This result is preliminary but encouraging and warrants further studies to *quantify* how well gating reduces fluorescence. Rather than recommending specific

gating setups, this study emphasizes that tradeoffs should be considered between competing experimental priorities for any Raman system.

Some studies warn that λ_{ex} > 260 nm usually triggers fluorescence of biochemical materials, limiting the variety of samples for which Raman spectra can be obtained without fluorescence interference (Hug et al., 2005). In contrast, it was found in this study that UV Raman at λ_{ex} = 266 nm is well-suited for mitigating fluorescence signals in Raman spectra, providing successful identifications of both kerogen and matrix minerals. Based on these results, UV excitation had more impact than gating on fluorescence mitigation. This result suggests that an *ungated* UV Raman instrument such as SHERLOC is suited for the detection of organics and minerals in lithologies likely to be targeted on Mars.

4.4.2. Sample-Specific Challenges with V-CW and G-UV Raman

Addressing goal 2, this study sought to identify sample-specific issues that could challenge identifications using Raman spectroscopy. **Two sample-dependent issues occurred in both Raman analyses and may arise during MSR scenarios: (1) The success of kerogen identification with V-CW Raman depended on lithotype; and (2) the mudstone sample impeded both V-CW and UV-G Raman analyses due to two different mechanisms.**

The success of kerogen identification with V-CW Raman was dependent on sample lithotype. Carbonates, whose fluorescence has been long known (Nichols et al., 1918), showed the highest fluorescence using V-CW Raman. With the carbonate-rich stromatolite, lacustrine carbonate, and the carbonate laminations of the sulfate evaporite,

it took us many attempts to identify kerogen with V-CW Raman, requiring high laser power (e.g., Figure 4.6C). This was true even though microscopy clearly showed kerogen was present at the location interrogated (e.g., Figure 4.6B). In some cases, kerogen or calcite could not be confirmed due to fluorescence unless the laser power was as high as 28 mW (Figure 4.6C). At such high laser powers and prolonged exposures, it is likely that the source of the fluorescence was burned away (known as "photo-quenching"; Bozlee et al., 2005) and allowed Raman detection. This can alter samples (Jorge-Villar and Edwards, 2013), especially those containing thermally immature organic matter (Marshall et al., 2010). This may give rise to spurious carbonaceous signatures, compromising both rover-based Raman data interpretations and Earth-based biogenicity analyses. Neither this study nor others have identified relationships between power, exposure time, band intensity, and organic or mineral thermal decomposition in Raman analyses. These likely depend on complex sample properties, such as composition and thermal conductivity.

In contrast to the carbonates, the two quartz-rich samples, the siliceous mudstone (Fig. 2B) and chert (Fig. 3C), showed low fluorescence in V-CW Raman, despite representing different ages and depositional environments. The chert matrix required the fewest attempts to identify kerogen and minerals (i.e., quartz). This is attributed to the dense, microcrystalline quartz matrix, which contributed to both the preservation of abundant organic matter and low fluorescence. The siliceous mudstone displayed slightly higher fluorescence than the chert, likely because it contained more immature kerogen. In diagenetically mature kerogen, abundant polycyclic aromatic hydrocarbons (PAHs) can quench fluorescence (Bertrand et al., 1986). Thus, the quartz lithotypes and those

containing diagenetically mature kerogen are considered "well-behaved" samples which will typically yield good quality Raman spectra, while challenging lithotypes such as highly fluorescent carbonates may reveal data that could lead to the minimization of Raman-based fluorescence and optimization of instrument performance. It is recommended that samples for Raman instrument optimization studies should be selected with this understanding.

In the evaporitic mudstone, mineral identification was challenging not only with V-CW Raman (due to fluorescence), but also with UV-G Raman (Figure 4.8D). In the latter case, the absence of mineral information in the mudstone, which contains abundant transition metal phases, is attributed to strong UV absorption by transition metal coordination complexes close to λ_{ex} = 266 nm combined with the weakness of inelastic Raman scattering. The mudstone matrix contains iron-bearing phases such as hematite (Table 4.1). UV absorption can occur in such phases at abundances as low as 0.01% by bulk weight (Cloutis et al., 2008). These and many other minerals commonly exhibit intense and broad charge transfer absorptions between 200 - 300 nm and especially 240-260 nm, such as octahedrally-coordinated Fe^{3+} transitions in hematite (Cloutis et al., 2008 and references therein). It is noted that iron and other transition metal-rich minerals were also identified in the marine sandstone matrix (Table 4.1), perhaps because of a different distribution and types of these phases, or differences in Raman scattering cross-sections (Stopar et al., 2005).

Although many Fe- and other transition metal-bearing minerals are confirmed or expected on Mars, the occurrences and abundances of metals, their oxidation state, ion species, coordination environment, metal–O covalency, mineral grain size, and

distribution (within detrital grain, as interlayer ions, on weathering rims, etc.) could affect the intensity and wavelength of UV absorption (Cloutis et al., 2008 and references therein). Thus, it is not possible to infer the success of UV Raman studies on Mars based on this result. Furthermore, no known studies (including the present one) have systematically explored UV Raman detections of biosignatures in a suite samples with metal-rich matrices preserving kerogen. In preparation for the upcoming Mars 2020 mission, on which the SHERLOC will have a λ_{ex} in the range of these absorptions, further work is recommended on the potential of UV Raman to detect biosignatures in samples with metal-rich matrices. Such studies should examine how UV-G Raman detections depend on the abundance and distribution of *both* kerogen and transition metal species in the matrix. They should also consider absorption due to scales, distributions, and mechanisms (e.g., phonon vibrations vs. fluorophores) and assess how instrument factors (power density, spot size differences) affect performance.

4.4.3. Detecting Organics with Fluorescence Spectroscopy

Goal 3 was to assess the capabilities of UVLITR fluorescence spectroscopy for detecting kerogen in the sample suite. **It was found that fluorescence spectroscopy allowed the detection of two types of organic fluorescence in all samples.** All fluorescence spectra were dominated by an ~100 nm-wide feature with a peak wavelength from 407 nm - 475 nm (Figure 4.10). This feature is caused by at least two types of organic fluorophores. The grouping of Type 1 organics (Figure 4.10A) was based on the morphology of the 407 - 475 nm feature, which is similar to that of the

kerogen standard. This similarity suggests a common composition between the standard and samples, such as aromatic components in PAHs.

In contrast, Type 2 organics spectra (Figure 4.10B) are attributed to surface contaminants. These spectra were obtained on regions where kerogen was not targeted, and show features similar to those of a sticker marker. In addition, Raman analyses of these spots showed a weak G band with a *S/N* below the threshold for true kerogen (section 3.2).

A second line of evidence for an organic origin for both Type 1 and 2 regions was found. Both had fluorescence decay lifetimes of ≲5 ns, consistent with organic chromophores (Sharma et al., 2003; Bozlee et al., 2005; Clegg et al., 2015) but whose quenching environment was unknown due to sample complexity. For instance, humic acids (kerogen precursors) have lifetimes <1-14 ns (Hemmingsen and McGown, 1997). For single PAHs, Eshelman et al. (2015) measured lifetimes of 2.2-7.3 ns with the same UV-G instrument used. Overall, fluorescence results suggest that a fluorescence spectroscopy instrument with ns-time resolution and the capability to capture a wavelength emission range >268 nm is suited to identify potential biosignatures on Mars.

In the evaporitic mudstone, fluorescence spectroscopy revealed organics (Figure 4.10B spectrum 3) otherwise not seen in Raman spectra (Figure 4.8D). Should a sample this challenging be analyzed with the Mars 2020 payload, multiple data sets will need to be combined to make robust caching decisions. Such decisions do not require knowledge of organic composition or origin (which fluorescence spectra alone cannot provide, according to these results); those analyses will be performed on Earth. Instruments such as PIXL (Allwood et al., 2015) and SuperCam, capable of measuring gated, ns-μs

fluorescence spectra, will likely work together to identify samples for caching based on evidence of potential biosignatures and geological context at multiple scales. This seems likely given recommendations from analog studies (e.g., Bishop et al., 2004) and based on the past success of this strategy with recent Martian rovers.

4.5. CONCLUSIONS

Using V-CW Raman and combined UV-G Raman / UVLITR fluorescence spectroscopy, kerogen and matrix mineral identification was investigated in a diverse, natural, realistic, Mars analog sample suite of seven samples representing a broad range of depositional environments regarded to be important targets for future sample return missions.

It was found that UV-G Raman could detect minerals and organics in samples without fluorescence interference, and with fewer attempts and higher confidence than V-CW Raman in all but one sample. In several samples, when examining the G band, the UV-G Raman system was able to sensitively detect mixed aromatic organics due to UV resonance Raman vibrational band enhancement in trace amounts of aromatic surface contaminants. A *S/N* threshold was defined to distinguish *in situ* kerogen versus similarly structured surface contaminants in the samples studied.

It was found that UV excitation has more impact than gating on fluorescence mitigation with UV-G Raman. Consequently, this study concluded that an ungated UV Raman instrument, such as SHERLOC, is well-suited for detecting a variety of minerals and organics, even at trace abundances, without being impeded by fluorescence likely to be present in samples targeted on Mars.

Two sample-dependent challenges were found with both types of Raman systems that may impact MSR. First, confident V-CW Raman identifications were harder in lithotypes having a carbonate host matrix than in samples dominated by quartz and diagenetically mature kerogen. Second, UV absorption in transition metal-containing phases complicated UV-G Raman analyses of the evaporitic mudstone sample. It is unclear how this result might impact biosignature detection with SHERLOC, a UV wavelength excitation system.

UV gated fluorescence spectra revealed two types of organic fluorescence, attributed to two different organic sources in all samples. In one case (evaporitic mudstone), fluorescence data revealed organics otherwise undetected in Raman spectra. This result suggests that time-resolved fluorescence spectra may provide sufficient information about biosignatures for rover caching decisions. Such decisions do not require firm knowledge of organic composition or origin (which fluorescence spectra alone cannot provide); detailed analyses will need to be performed on Earth. Results suggest that a fluorescence spectroscopy instrument with ns-time resolution and the capability to capture a wavelength emission range >268 nm is suited to identify potential biosignatures on Mars.

The results presented here are intended to guide strategies for caching decisions and MSR, and to inform future development of Raman and fluorescence instruments. These results highlight the need for further studies of this kind, guided by sample-dependent and science-driven considerations, in light of the approaching Mars 2020 launch. Four recommendations for such studies include:

1. Use challenging, natural samples containing non-extracted kerogen to develop databases of data sets expected on Mars;
2. Investigate fluorescence rejection strategies in visible wavelength Raman systems, especially gating, while considering relationships between laser power, exposure time, Raman band intensity, and impacts on biosignature and/or mineral thermal alteration;
3. Understand the limits of biosignature detection in transition metal-rich natural samples with UV excitation Raman systems;
4. Develop protocols to gain information about samples by combining *in situ* data sets (e.g., Raman plus fluorescence) from multiple payload instruments that span spacial scales.

CHAPTER 5

CONCLUDING THOUGHTS

The research presented in this dissertation is a marriage of sample-dependent challenges and instrument-dependent considerations. The goal of this dissertation research was to inform biosignature studies on Mars using realistic, natural samples and *in situ* Raman spectroscopy techniques targeted for upcoming astrobiology investigations on Mars.

In Chapter 1, an introductory framework and motivations for this dissertation were provided. Two upcoming missions, Mars 2020 (NASA) and ExoMars (European Space Agency), will usher in a new era in Mars exploration: the rover-based search for potential biosignatures, based on the perceived BPP based on results from *in situ*, rover-based instruments. To enhance the success of these missions, studies, such as those presented in this dissertation, are needed to refine the understanding of the BPP under different depositional environments and using *in situ*, non-destructive, and micro-scale techniques. An improved understanding of BPP is necessary to ensure successful *in situ* target sampling strategies and biosignature assessments in ancient habitable, aqueous environments on Mars with high preservation potential.

Chapter 2 demonstrated an approach for addressing BPP on Mars through the study of a Miocene-Pliocene age playa evaporite sequence in the Verde Formation of central AZ. Our studies of the Verde Fm. playa evaporite system revealed a complex sequence of diagenetic events. The results presented in Chapter 2 may help refine taphonomic models for understanding BPP in evaporite deposits that originate from Mg-

Na-Ca-SO_4-Cl brines in continental basins. For similar habitable environments on Mars, this observational framework may help guide identification of samples having the highest BPP for both *in situ* and MSR analyses.

Chapter 2 concluded that the concept of BPP needs to be further refined using micro-scale, non-destructive, and quantifiable results from investigations of analog sedimentary systems that are considered as high-priority exploration targets for MSR, based on recommendations of the astrobiology and Mars communities. One path forward could include the use of electron microprobe analysis (EMPA) to characterize organic matter *in situ* in samples. EPMA has been commonly used for characterizing morphologies of microfossils and to map the distribution of elements associated with organic phases in various geological materials (e.g., meteorites). Chapter 2 investigated a potential EPMA method for quantifying the BPP in Verde Fm. playa evaporites through the creation of 2D carbon maps on thin section rounds. The method involved using the carbon area coverage as a proxy for BPP within one subfacies that could be compared against other subfacies. However, this approach showed that there are many limitations that prevent the success of this method at the present time, detailed further in Chapter 2. Further studies, using EPMA or other techniques, are recommended to develop robust, quantifiable, and nondestructive methods for examining BPP in analog samples considered high-priority for MSR.

EPMA-based BPP analysis may have applications not only for investigations of kerogen preserved in the Martian rock record, but also for studies of organic matter in meteorites. Adsorption of organic matter onto meteoritic minerals, followed by later stage heating and alteration in the space environment, may be analogous to the capture and

preservation of kerogen in sedimentary terrestrial environments, followed by environmental diagenesis. Destructive and bulk techniques are standard for studies of meteoritic organic matter. Better understanding these processes using *in situ*, non-destructive methods could lead to a better understanding of the relationship between meteoritic organic matter and minerals, as well as their origin and alteration history in the solar system. Future work could also explore the application of EPMA-based *in situ* biosignature mapping to meteoritic organic matter.

The sampling strategy envisioned for the Mars 2020 mission is to identify and cache samples that have a high BPP. This requires an integrated instrument payload that can select samples with the highest BPP, utilizing non-destructive methods to detect and identify potential biosignatures. Raman spectroscopy has the potential to provide such *in situ* measurements. Three Raman instruments are scheduled to be launched on two upcoming astrobiology-based Mars rover missions. In light of this development, it is fundamentally important that sample-dependent limitations of Raman systems being developed for flight be understood ahead of time to ensure optimal performance during missions. Chapter 3 highlighted the use of Raman spectroscopy in characterizing four major lithotypes that have been given a high-priority for Mars astrobiology and MSR. Four major findings were identified that have the potential to impact the future development of Raman systems for space missions. Most importantly, sample-dependent issues were discussed that can affect data acquisition and interpretations. Raman-based fluorescence interference was found to be the major sample-dependent issue discussed in Chapter 3. Further studies of fluorescence rejection techniques in Raman systems are warranted to improve the understanding of the relationships between Raman laser power,

exposure time, Raman peak intensity, and the impacts of thermal decomposition of organics and minerals in samples. Further studies should also focus on reducing fluorescence in Raman instruments for flight using realistic, challenging natural samples that have a high-priority for MSR. It is hoped that this study will help identify practical science-driven strategies for developing Raman systems for future flight missions.

Chapter 4 continued the theme of Raman-based fluorescence rejection strategies by highlighting two fluorescence reduction techniques that share similarities with two Raman systems to be launched on the Mars 2020 rover: time-gating and UV laser excitation wavelength optimization. Chapter 4 compared a visible laser excitation Raman system with a combined UV laser excitation gated Raman and laser-induced time resolved fluorescence spectroscopy system to investigate kerogen and matrix mineral identifications in a Mars analog sample suite representing a broad range of depositional environments regarded to be important targets for MSR. The same suite of samples investigated in Chapter 3 was expanded in Chapter 4 to include more challenging analog samples.

Chapter 4 found that UV-gated Raman could detect minerals and organics without fluorescence interference, with fewer attempts, and with higher confidence than visible Raman in all but one sample. Results obtained in Chapter 4 also showed that UV excitation had more impact than gating on fluorescence mitigation with UV-gated Raman system.

Chapter 4 results suggest that promising results can be obtained with Raman and fluorescence instruments from the Mars 2020 payload. Chapter 4 concluded that SHERLOC, a UV Raman system, is well-suited to detect all Raman bands associated

with not only with kerogen, but also other organics, especially those that occur at low abundance. Additionally, Chapter 4 concluded that Raman-based detection using UV Raman is unimpeded by fluorescence interference. Furthermore, results suggested that an *ungated* UV Raman instrument, such as SHERLOC, is suited for detecting organics and minerals in lithotypes that are likely to be targeted for astrobiology investigations on Mars. Finally, fluorescence results suggested that a fluorescence spectroscopy instrument with ns-time resolution and the capability to capture a wavelength emission range >268 nm is suited to identify potential biosignatures on Mars.

Chapter 4 also documents two sample-dependent challenges with both types of Raman systems that could impact MSR: (1) Confident V-CW Raman identifications were harder for lithotypes that had a carbonate host matrix as compared to lithotypes dominated by quartz and diagenetically mature kerogen; and (2) an evaporitic mudstone that contains phases with transition metals proved challenging using the UV-G Raman system. In preparation for the upcoming Mars 2020 mission, where SHERLOC will have an excitation wavelength in the range of transition metal absorptions, further work will be needed to fully understand the potential of UV Raman to detect biosignatures. Such studies should examine how UV-G Raman detections depend on the abundance and distribution of both kerogen and transition metal species in fine-grained matrixes. Such studies should also consider absorption effects due to scales, distributions, and mechanisms (e.g., phonon vibrations vs. fluorophores) and assess how instrument factors (power density, spot size differences) affect performance.

Taken together, the results obtained in this dissertation align with NASA's

recommendations to inform *in situ* approaches for the upcoming Mars 2020 mission and Mars Sample Return by:

1. Refining models for biosignature preservation in realistic, challenging, and relevant natural Mars analog samples;
2. Improving the ability to select and cache samples on Mars with the highest biosignature preservation potential, in order to increase the potential success of finding life in samples *in situ,* following their return to Earth for detailed studies; and
3. Informing fluorescence reduction strategies and instrument development for future Raman systems that will be used to target biosignatures *in situ*, such as those planned to launch onboard the next two Mars missions.

Once *in situ* rover analysis select and successfully cache samples for Earth return, analyses on Earth are likely to be challenging. This is based on lessons learned from studies of Earth's earliest fossil record and reports of putative microfossils in the Martian meteorite, ALH84001. More studies are needed to define standardized, end-to-end protocols to confirm or reject the biogenicity of samples returned from Mars. One such effort is currently in development. This effort will entail developing a protocol for analysis of returned samples by performing detailed characterizations of geological context and spatial distributions of minerals and biosignatures in relevant, challenging Mars analogs, integrating diverse techniques that span spatial scales. This work plans to bridge the MSR goals discussed in this dissertation with efforts to inform NASA's strategies for analyses of returned samples from Mars.

REFERENCES

Aiello, I.W., Garrison, R.E., Moore, J.C., Kastner, M., Stakes, D.S., 2001. Anatomy and origin of carbonate structures in a Miocene cold-seep field. Geology 29, 1111-1114.

Allison, P.A., Briggs, D.E., 1991. *Taphonomy of nonmineralized tissues. Taphonomy: Releasing the Data Locked in the Fossil Record*: Plenum Press, New York, 25-70.

Allison, P.A., Pye, K., 1994. Early diagenetic mineralization and fossil preservation in modern carbonate concretions. Palaios 561-575.

Allwood, A.C., Walter, M.R., Kamber, B.S., Marshall, C.P. and Burch, I.W., 2006. Stromatolite reef from the Early Archaean era of Australia. Nature 441(7094), 714-718.

Allwood, A.C., Grotzinger, J.P., Knoll, A.H., Burch, I.W., Anderson, M.S., Coleman, M.L., Kanik, I., 2009. Controls on development and diversity of Early Archean stromatolites. Proc. Natl. Acad. Sci. U. S. A. 106, 9548-9555.

Allwood, A., Clark, B., Flannery, D., Hurowitz, J., Wade, L., Elam, T., Foote, M., Knowles, E., 2015. Texture-specific elemental analysis of rocks and soils with PIXL: The Planetary Instrument for X-ray Lithochemistry on Mars 2020, In 2015 IEEE Aerospace Conference, 1-13.

Anderson, R.Y., Dean, W.E., Kirkland, D.W., Snider, H.I., 1972. Permian Castile varved evaporite sequence, West Texas and New Mexico. Geological Society of America Bulletin 83, 59-86.

Anthony, J.W., Williams, S.A., Bideaux, R.A., 1982. *Mineralogy of Arizona:* University of Arizona Press.

Asher, S., 1993. UV resonance Raman spectroscopy for analytical, physical, and biophysical chemistry. Analytical Chemistry 65(4), 201A-210A.

Ayers, S., 2012. A taste of seasons past at the Camp Verde Salt Mine. Verde Independent. Retrieved from http://verdenews.com/main.asp SectionID=74&subsectionID=696&articleID=46875

Baker, P.A., Bloomer, S.H., 1988. The origin of celestite in deep-sea carbonate sediments. Geochim. Cosmochim. Acta 52, 335-339.

Banin, A., Han, F., Kan, I., Cicelsky, A., 1997. Acidic volatiles and the Mars soil. J. Geo. Res.: Planets (1991–2012) 102, 13341-13356.

Barbieri, R., Stivaletta, N., Marinangeli, L., Ori, G.G., 2006. Microbial signatures in sabkha evaporite deposits of Chott el Gharsa (Tunisia) and their astrobiological implications. Planet. Space Sci. 54, 726-736.

Bartholomew, P., 2012. Fluorescence interference in Raman spectroscopy: will the geoscience community drive the instrument industry? In 2012 GSA Annual Meeting, paper #267-9.

Bartholomew, P., 2014. The role of intensity and instrument sensitivity in Raman mineral identification. LPI Contributions 1783, abstract #5087.

Beegle, L., Bhartia, R., White, M., Deflores, L., Abbey, W., Wu, Y.-H., Cameron, B., Moore, J., Fries, M., Burton, A., Edgett, K.S., Ravine, M.A., Hug, W., Reid, R., Nelson, T., Clegg, S., Wiens, R., Asher, S., Sobron, P., 2015. SHERLOC: Scanning habitable environments with Raman & luminescence for organics & chemicals, In: IEEE Aerospace Conference Proceedings, #7119105.

Beers, Y., 1957. *Introduction to the theory of error*: Addison Wesley Publishing Company, Reading.

Bellanca, A., Calvo, J., Censi, P., Neri, R., Pozo, M., 1992. Recognition of lake-level changes in Miocene lacustrine units, Madrid Basin, Spain: Evidence from facies analysis, isotope geochemistry and clay mineralogy. Sediment. Geol. 76, 135-153.

Benison, K.C., Jagniecki, E.A., Edwards, T.B., Mormile, M.R. and Storrie-Lombardi, M.C., 2008. “Hairy blobs:” microbial suspects preserved in modern and ancient extremely acid lake evaporites. Astrobiology 8 (4), 807-821.

Berenblut, B., Dawson, P., Wilkinson, G., 1973. A comparison of the Raman spectra of anhydrite ($CaSO_4$) and gypsum ($CaSO_4$)$*2H_2O$. Spectrochim. Acta, Pt. A: Mol. Spectrosc. 29, 29-36.

Bertrand, P., Pittion, J., Bernaud, C., 1986. Fluorescence of sedimentary organic matter in relation to its chemical composition. Org. Geochem. 10, 641-647.

Bibring, J.P., Langevin, Y., Gendrin, A., Gondet, B., Poulet, F., Berthe, M., Soufflot, A., Arvidson, R., Mangold, N., Mustard, J., Drossart, P., OMEGA team, 2005. Mars surface diversity as revealed by the OMEGA/Mars Express observations. Science 307, 1576-1581.

Bibring, J.P., Langevin, Y., Mustard, J.F., Poulet, F., Arvidson, R., Gendrin, A., Gondet, B., Mangold, N., Pinet, P., Forget, F., Berthe, M., Bibring, J.P., Gendrin, A., Gomez, C., Gondet, B., Jouglet, D., Poulet, F., Soufflot, A., Vincendon, M., Combes, M., Drossart, P., Encrenaz, T., Fouchet, T., Merchiorri, R., Belluci, G., Altieri, F., Formisano, V., Capaccioni, F., Cerroni, P., Coradini, A., Fonti, S., Korablev, O., Kottsov, V., Ignatiev, N., Moroz, V., Titov, D., Zasova, L., Loiseau, D., Mangold, N., Pinet, P., Doute, S., Schmitt, B., Sotin, C., Hauber, E., Hoffmann, H., Jaumann, R., Keller, U., Arvidson, R., Mustard, J.F., Duxbury, T., Forget, F., Neukum, G., 2006. Global mineralogical and aqueous mars history derived from OMEGA/Mars Express data. Science 312 (400), 400-404.

Bish, D.L., Blake, D.F., Vaniman, D.T., Chipera, S.J., Morris, R.V., Ming, D.W., Treiman, A.H., Sarrazin, P., Morrison, S.M., Downs, R.T., Achilles, C.N., Yen, A.S., Bristow, T.F., Crisp, J.A., Morookian, J.M., Farmer, J.D., Rampe, E.B., Stolper, E.M., Spanovich, N., MSL Science Team, 2013. X-ray diffraction results from Mars Science Laboratory: Mineralogy of Rocknest at Gale crater. Science 341, 1238932.

Bishop, J.L., Murad, E., Lane, M.D., Mancinelli, R.L., 2004. Multiple techniques for mineral identification on Mars: A study of hydrothermal rocks as potential analogues for astrobiology sites on Mars. Icarus 169 (2), 311-323.

Bishop, J., Lane, M., Dyar, M., Brown, A., 2008. Reflectance and emission spectroscopy study of four groups of phyllosilicates: Smectites, kaolinite-serpentines, chlorites and micas. Clay Miner. 43, 35-54.

Blacksberg, J., Rossman, G.R., Gleckler, A., 2010. Time-resolved Raman spectroscopy for in situ planetary mineralogy. Appl. Opt. 49, 4951-4962.

Blacksberg, J., Maruyama, Y., Charbon, E., Rossman, G.R., 2011. Fast single-photon avalanche diode arrays for laser Raman spectroscopy. Opt. Lett. 36, 3672-3674.

Blacksberg, J., Alerstam, E., Maruyama, Y., Charbon, E., Rossman, G., Shkolyar, S., Farmer, J., 2013. Planetary surface exploration using Raman spectroscopy for minerals and organics. 2013 AGU Fall Meeting (Vol. 1, p. 1803), abstract #P51G-1803.

Blacksberg, J., Alerstam, E., Maruyama, Y., Cochrane, C., Rossman, G., 2014a. Time-Resolved Raman spectroscopy for planetary science. LPI Contributions 1783, 11th International GeoRaman Conference, abstract #5055.

Blacksberg, J., Maruyama, Y., Alerstam, E., Cochrane, C., Rossman, G., Shkolyar, S., Farmer, J., 2014b. Time-Resolved Raman spectroscopy of Mars analog minerals and organics. In 45th Lunar and Planetary Science Conference, abstract #1544.

Blake, W.P., 1890. Thenardite, mirabilite, glauberite, halite and associates of the Verde Valley, Arizona Territory. Am. Jour. Sci., 39, 43-45.

Bost, N., Ramboz, C., Lebreton, N., Foucher, F., Lopez-Reyes, G., De Angelis, S., Josset, M., Venegas, G., Sanz-Arranz, A., Rull, F., 2015. Testing the ability of the ExoMars 2018 payload to document geological context and potential habitability on Mars. Planet. Sp. Sci. 108, 87-97.

Bozlee, B.J., Misra, A.K., Sharma, S.K., Ingram, M., 2005. Remote Raman and fluorescence studies of mineral samples. Spectrochim. Acta Part A: Mol. Biomol. Spectrosc. 61, 2342-2348.

Brasier, M.D., Green, O.R., Jephcoat, A.P., Kleppe, A.K., Van Kranendonk, M.J., Lindsay, J.F., Steele, A., Grassineau, N.V., 2002. Questioning the evidence for Earth's oldest fossils. Nature 416 (6876), 76-81.

Bressler, S.L., Butler, R.F., 1978. Magnetostratigraphy of the late Tertiary Verde Formation, Central Arizona. Earth Planet. Sci. Lett. 38, 319-330.

Bristow, T.F., Bish, D.L., Vaniman, D.T., Morris, R.V., Blake, D.F., Grotzinger, J.P., Rampe, E.B., Crisp, J.A., Achilles, C.N., Ming, D.W., 2015. The origin and implications of clay minerals from Yellowknife Bay, Gale Crater, Mars. Am. Mineral. 100, 824-836.

Brody, R.H., Edwards, H.G., Pollard, A.M., 2001. A study of amber and copal samples using FT-Raman spectroscopy. Spectrochim. Acta Part A: Molec. and Biomolec. Spec. 57, 1325-1338.

Brown, A.J., Hook, S.J., Baldridge, A.M., Crowley, J.K., Bridges, N.T., Thomson, B.J., Marion, G.M., de Souza Filho, Carlos R, Bishop, J.L., 2010. Hydrothermal formation of clay-carbonate alteration assemblages in the Nili Fossae region of Mars. Earth Planet. Sci. Lett. 297, 174-182.

Butler, G.P., 1973. Strontium geochemistry of modern and ancient calcium sulphate minerals, in The Persian Gulf. Springer, pp. 423-452.

Cady, S.L., 2001. Paleobiology of the Archean. Adv. Appl. Microbiol. 50, 3-35.

Carroll, A.R. and Bohacs, K.M., 2001. Lake-type controls on petroleum source rock potential in nonmarine basins. AAPG Bulletin 85 (6), 1033-1053.

Clark, R.N., King, T.V., Klejwa, M., Swayze, G.A., Vergo, N., 1990. High spectral resolution reflectance spectroscopy of minerals. J. Geophys. Res.: Solid Earth 95, 12653-12680.

Clegg, S.M., Wiens, R.C., Maurice, S., Gasnault, O., Sharma, S.K., Misra, A.K., Newell, R., Forni, O., Lasue, J., Anderson, R.B., Nowak-Lovato, K.L., Fouchet, T., Angel, S.M., Rull, F., Johnson, J.R., 2015. Remote geochemical and mineralogical analysis with supercam for the Mars 2020 rover. In 46th Lunar and Planetary Science Conference, abstract #2781.

Cloutis, E.A., McCormack, K.A., Bell, J.F., Hendrix, A.R., Bailey, D.T., Craig, M.A., Mertzman, S.A., Robinson, M.S., Riner, M.A., 2008. Ultraviolet spectral reflectance properties of common planetary minerals. Icarus 197, 321-347.

Cornell, R., Schwertmann, U., 2001. The *Iron Oxides. Structure, Properties*: Wiley-VCH.

Czaja, A.D., Kudryavtsev, A.B., Cody, G.D., Schopf, J.W., 2009. Characterization of permineralized kerogen from an Eocene fossil fern. Org. Geochem. 40, 353-364.

Des Marais, D.J., 2001. Isotopic evolution of the biogeochemical carbon cycle during the Precambrian. Reviews in Mineralogy and Geochemistry 43, 555-578.

Des Marais, D.J., Nuth III, J.A., Allamandola, L.J., Boss, A.P., Farmer, J.D., Hoehler, T.M., Jakosky, B.M., Meadows, V.S., Pohorille, A., Runnegar, B., 2008. The NASA astrobiology roadmap. Astrobiology 8, 715-730.

DeWitt, E., Langenheim, V., Force, E., Vance, R.K., Lindberg, P., Driscoll, R., 2008. Geologic map of the Prescott National Forest and the headwaters of the Verde River, Yavapai and Coconino Counties, Arizona.

Dharmasena, G., Frech, R., 1993. The stabilization of phase III and phase I in sodium sulfate by aliovalent cation substitution. J. Chem. Phys. 99, 8929-8935.

Dickensheets, D.L., Wynn-Williams, D.D., Edwards, H.G., Schoen, C., Crowder, C., Newton, E.M., 2000. A novel miniature confocal microscope/Raman spectrometer system for biomolecular analysis on future Mars missions after Antarctic trials. J. Raman Spec. 31, 633-635.

Donchin, J.H., 1983. Stratigraphy and sedimentary environments of the Miocene-Pliocene Verde Formation in the southeastern Verde Valley, Yavapai County, Arizona. MS Thesis, University of Arizona.

Donovan, J., Rose, A., 1992. The chemical jump: Hydrologic control of brine reaction path within calcareous aquifers and alkaline lakes, semi-arid northern Great Plains, USA, Proceedings of the 7th International Symposium on Water Rock interaction, 639-42.

Downs, R., 2006. The RRUFF Project: an integrated study of the chemistry, crystallography, Raman and Infrared spectroscopy of minerals. In Program and Abstracts of the 19th General Meeting of the International Mineralogical Association.

Edwards, H., Farwell, D., 1996. Fourier transform-Raman spectroscopy of amber. Spectrochimica Acta Part A: Molecular and Biomolecular Spectroscopy 52, 1119-1125.

Edwards, H., Hutchinson, I., Ingley, R., 2012. The ExoMars Raman spectrometer and the identification of biogeological spectroscopic signatures using a flight-like prototype. Analy Bioanal Chem 404, 1723-1731.

Ehlmann, B.L., Mustard, J.F., Fassett, C.I., Schon, S.C., Head III, J.W., Des Marais, D.J., Grant, J.A., Murchie, S.L., 2008a. Clay minerals in delta deposits and organic preservation potential on Mars. Nature Geoscience 1, 355-358.

Ehlmann, B.L., Mustard, J.F., Murchie, S.L., Poulet, F., Bishop, J.L., Brown, A.J., Calvin, W.M., Clark, R.N., Marais, D.J., Milliken, R.E., Roach, L.H., Roush, T.L., Swayze, G.A., Wray, J.J., 2008b. Orbital identification of carbonate-bearing rocks on Mars. Science 322 (5909), 1828-1832.

Eneva, M., Falorni, G., Teplow, W., Morgan, J., Rhodes, G., Adams, D., 2011. Surface deformation at the San Emidio geothermal field, Nevada, from satellite radar interferometry. Geothermal Resources Council Transactions 35, 1647-1653.

Eshelman, E., Daly, M.G., Slater, G., Dietrich, P., Gravel, J.-F., 2014. An ultraviolet Raman wavelength for the in-situ analysis of organic compounds relevant to astrobiology. Planet. Sp. Sci. 93–94, 65–70.

Eshelman, E., Daly, M., Slater, G., Cloutis, E., 2015. Time-resolved detection of aromatic compounds on planetary surfaces by ultraviolet laser induced fluorescence and Raman spectroscopy. Planet. Space Sci. 119, 200-207.

Esposito, A. and Wouters, F.S., 2004. Fluorescence lifetime imaging microscopy. Current Protocols in Cell Biology, 4-14.

Eugster, H.P., Surdam, R.C., 1973. Depositional environment of the Green River Formation of Wyoming: a preliminary report. Geological Society of America Bulletin 84, 1115-1120.

Eugster, H.P., 1980. Geochemistry of evaporitic lacustrine deposits. Annu. Rev. Earth Planet. Sci. 8, 35.

Farmer, J.D., 1995. Mars exopaleontology. Palaios 10, 197-198.

Farmer, J., 1998. Thermophiles, early biosphere evolution, and the origin of life on Earth: implications for the exobiological exploration of Mars. Journal of Geophysical Research: Planets 103, 28457-28461.

Farmer, J.D., 1999. Environmental and Mineralogical Controls on Fossilization: Key Elements in a Strategy for Mars Exopaleontology 1, 6224.

Farmer, J.D., Des Marais, D.J., 1999. Exploring for a record of ancient Martian life. J Geophys. Res.: Planets (1991–2012) 104, 26977-26995.

Farmer, J.D., 2012. Science Priorities for Mars Astrobiology. LPI Contributions 1679, In Concepts and Approaches for Mars Exploration, abstract #4304.

Ferrari, A., Robertson, J., 2001. Resonant Raman spectroscopy of disordered, amorphous, and diamondlike carbon. Phys. Rev. B 64, 075414.

Frosch, T., Tarcea, N., Schmitt, M., Thiele, H., Langenhorst, F., Popp, J., 2007. UV Raman Imaging A Promising Tool for Astrobiology: Comparative Raman Studies with Different Excitation Wavelengths on SNC Martian Meteorites. Anal. Chem. 79, 1101-1108.

Gaft, M., Nagli, L., 2009. Gated Raman spectroscopy: potential for fundamental and applied mineralogy. European J. Mineral. 21, 33-42.

Gaft, M., Panczer, G., 2013. Laser-induced time-resolved luminescence spectroscopy of minerals: a powerful tool for studying the nature of emission centres. Mineral. Petrol. 107 (3), 363–372.

Gendrin, A., Mangold, N., Bibring, J.P., Langevin, Y., Gondet, B., Poulet, F., Bonello, G., Quantin, C., Mustard, J., Arvidson, R., LeMouelic, S., 2005. Sulfates in Martian layered terrains: the OMEGA/Mars Express view. Science 307, 1587-1591.

Glotch, T.D., Bandfield, J.L., Christensen, P.R., Calvin, W.M., McLennan, S.M., Clark, B.C., Rogers, A.D., Squyres, S.W., 2006. Mineralogy of the light‐toned outcrop at Meridiani Planum as seen by the Miniature Thermal Emission Spectrometer and implications for its formation. J. Geophys. Res.: Planets (1991–2012) 111.

Glotch, T.D., Rogers, A.D., 2007. Evidence for aqueous deposition of hematite‐and sulfate‐rich light‐toned layered deposits in Aureum and Iani Chaos, Mars. Journal of Geophysical Research: Planets 112 (E6).

Golden, D., Ming, D.W., Morris, R.V., Mertzman, S.A., 2005. Laborator-simulated acid-sulfate weathering of basaltic materials: Implications for formation of sulfates at Meridiani Planum and Gusev crater, Mars. J Geophys. Res: Planets (1991–2012) 110.

Goncharov, A.F. and Crowhurst, J.C., 2005. Pulsed laser Raman spectroscopy in the laser-heated diamond anvil cell. Rev.of Sci. Instr. 76, 63905-63905.

Gorevan, S., Myrick, T., Davis, K., Chau, J., Bartlett, P., Mukherjee, S., Anderson, R., Squyres, S., Arvidson, R., Madsen, M., 2003. Rock abrasion tool: Mars exploration rover mission. J Geophys. Res.: Planets (1991–2012), 108.

Grotzinger, J.P., 2009. Beyond water on Mars. Nature Geoscience 2, 231-233.

Grotzinger, J.P., Sumner, D.Y., Kah, L.C., Stack, K., Gupta, S., Edgar, L., Rubin, D., Lewis, K., Schieber, J., Mangold, N., Milliken, R., Conrad, P.G., DesMarais, D., Farmer, J., Siebach, K., Calef, F.,3rd, Hurowitz, J., McLennan, S.M., Ming, D., Vaniman, D., Crisp, J., Vasavada, A., Edgett, K.S., Malin, M., Blake, D., Gellert, R., Mahaffy, P., Wiens, R.C., Maurice, S., Grant, J.A., Wilson, S., Anderson, R.C., Beegle, L., Arvidson, R., Hallet, B., Sletten, R.S., Rice, M., Bell, J.,3rd, Griffes, J., Ehlmann, B., Anderson, R.B., Bristow, T.F., Dietrich, W.E., Dromart, G., Eigenbrode, J., Fraeman, A., Hardgrove, C., Herkenhoff, K., Jandura, L., Kocurek, G., Lee, S., Leshin, L.A., Leveille, R., Limonadi, D., Maki, J., McCloskey, S., Meyer, M., Minitti, M., Newsom, H., Oehler, D., Okon, A., Palucis, M., Parker, T., Rowland, S., Schmidt, M., Squyres, S., Steele, A., Stolper, E., Summons, R., Treiman, A., Williams, R., Yingst, A., MSL Science Team, 2014. A habitable fluvio-lacustrine environment at Yellowknife Bay, Gale crater, Mars. Science 343, 1242777.

Grotzinger, J.P., Gupta, S., Malin, M.C., Rubin, D.M., Schieber, J., Siebach, K., Sumner, D.Y., Stack, K.M., Vasavada, A.R., Arvidson, R.E. and Calef, F., 2015. Deposition, exhumation, and paleoclimate of an ancient lake deposit, Gale crater, Mars. Science, 350 (6257), aac7575.

Hamilton, A., Menzies, R.I., 2010. Raman spectra of mirabilite, Na2SO4·10H2O and the rediscovered metastable heptahydrate, $Na_2SO_4 \cdot 7H_2O$. J Raman Spec. 41, 1014-1020.

Hardie, L.A., 1968. The origin of the recent non-marine evaporite deposit of Saline Valley, Inyo County, California. Geochim. Cosmochim. Acta 32, 1279-1301.

Hardie, L.A., Eugster, H.P., 1970. The evolution of closed-basin brines. Mineralogical Society of America Special Publication 3, 273-290.

Hemmingsen, S.L., McGown, L.B., 1997. Phase-resolved fluorescence spectral and lifetime characterization of commercial humic substances. Appl. Spectrosc. 51 (7), 921-929.

Hesse, 1990. Origin of chert. In McIlreath, I. A., & Morrow, D. W. 1990. Diagenesis (Vol. 4). Geological Association of Canada.

Hofmann, H., Grey, K., Hickman, A., Thorpe, R., 1999. Origin of 3.45 Ga coniform stromatolites in Warrawoona group, Western Australia. Geol. Soc. of Am. Bull. 111, 1256-1262.

Hooijschuur, J., Davies, G., Ariese, F., 2014. Raman Spectroscopy of Deinococcus Radiodurans and beta-carotene on a mineral background. LPI Contributions 1783, 11th International GeoRaman Conference, abstract #5068.

Hug, W.F., Bhartia, R., Taspin, A., Lane, A., Conrad, P., Sijapati, K., Reid, R.D., 2005. Status of miniature integrated UV resonance fluorescence and Raman sensors for detection and identification of biochemical warfare agents. Proceedings of SPIE – The International Society for Optical Engineering, 5994.

Hunt, C.B., 1975. *Death Valley: Geology, Ecology, Archaeology*: Univ of California Press, Berkeley.

Jankowski, J., Jacobson, G., 1989. Hydrochemical evolution of regional groundwaters to playa brines in Central Australia. Journal of Hydrology 108, 123-173.

Jehlicka, J., Edwards, H.G., Culka, A., 2010. Using portable Raman spectrometers for the identification of organic compounds at low temperatures and high altitudes: exobiological applications. Philos. Trans. A. Math. Phys. Eng. Sci. 368 (1922), 3109-3125.

Jorge-Villar, S.E., Edwards, H.G., 2013. Microorganism response to stressed terrestrial environments: a Raman spectroscopic perspective of extremophilic life strategies. Life 3, 276-294.

Kasprzyk, A., 2013. Distribution of strontium in the Badenian (Middle Miocene) gypsum deposits of the Nida area, southern Poland. Geol. Quarterly 38, 497-512.

Katz, B.J., Bissada, K.K., Wood, J.W., 1987. Factors limiting potential of evaporites as hydrocarbon source rocks, SEG Technical Program Expanded Abstracts, pp. 281-283

Kennedy, M.J., Pevear, D.R., Hill, R.J., 2002. Mineral surface control of organic carbon in black shale. Science 295, 657-660.

Kieffer, S.W., 1979. Thermodynamics and lattice vibrations of minerals: 2. Vibrational characteristics of silicates. Rev. Geophys. 17, 20-34.

Kloprogge, J.T., Ruan, H., Duong, L.V., Frost, R.L., 2001. FT-IR and Raman microscopic study at 293 K and 77 K of celestine, $SrSO_4$, from the middle triassic limestone (Muschelkalk) in Winterswijk, The Netherlands. Geol. Mijnbouw 80, 41-48.

LaFuente, B., Downs, R., Yang, H., Stone, N., 2015. The power of databases: the RRUFF project. Highlights in Mineralogical Crystallography, 1-30.

Langbein, W.B., 1961. Salinity and hydrology of closed lakes (No. 412). USGS Professional Paper, 412.

Lausen, C., 1928. Hydrous sulphates formed under fumerolic conditions at the United Verde mine. Am. Mineral. 13, 203-229.

Liu, Y., Wang, A., Freemen, J., 2009. Raman, MIR, and NIR spectroscopic study of calcium sulfates: gypsum, bassanite, and anhydrite. In 40th Lunar and Planetary Science Conference, abstract #2128.

Lockard, J.C., 2009. Microbial Biosignature Capture and Preservation in Sulfate Evaporites. MS Thesis, Arizona State Unviersity.

Lowe, D.R., 1980. Stromatolites 3,400-myr old from the archean of Western Australia. Nature 284, 441-443.

Lowenstein, T.K., Schubert, B.A., Timofeeff, M.N., 2011. Microbial communities in fluid inclusions and long-term survival in halite. GSA Today 21, 4-9.

Madden, M.E., Bodnar, R., Rimstidt, J., 2004. Jarosite as an indicator of water-limited chemical weathering on Mars. Nature 431 (2010), 821-823.

Maeda, H., G. Tanaka, N. Shimobayashi, T. Ohno, and H. Matsuoka, 2011. Cambrian Orsten Lagerstätte from the Alum Shale Formation: Fecal pellets as a probable source of phosphorus preservation. Palaios 26 (4), 225-231.

Mancinelli, R., Fahlen, T., Landheim, R., Klovstad, M., 2004. Brines and evaporites: analogs for Martian life. Advances in Space Research 33, 1244-1246.

Marshall, C.P., Carter, E.A., Leuko, S., Javaux, E.J., 2006. Vibrational spectroscopy of extant and fossil microbes: relevance for the astrobiological exploration of Mars. Vibrational Spectroscopy 41, 182-189.

Marshall, C.P., Edwards, H.G., Jehlicka, J., 2010. Understanding the application of Raman spectroscopy to the detection of traces of life. Astrobiology 10, 229-243.

Marshall, C.P., Emry, J.R., Marshall, A.O., 2011. Haematite pseudomicrofossils present in the 3.5-billion-year-old Apex Chert. Nat. Geosci. 4, 240-243.

Marshall, A.O., Emry, J.R., Marshall, C.P., 2012. Multiple generations of carbon in the Apex Chert and implications for preservation of microfossils. Astrobiology 12, 160-166.

Martyshkin, D., Ahuja, R., Kudriavtsev, A., Mirov, S., 2004. Effective suppression of fluorescence light in Raman measurements using ultrafast time gated charge coupled device camera. Rev. Sci. Instrum. 75, 630-635.

Maruyama, Y., Blacksberg, J. and Charbon, E., 2013. A 1024 x 8 700ps time-gated SPAD line sensor for laser raman spectroscopy and LIBS in space and rover-based planetary exploration. In 2013 IEEE International Solid-State Circuits Conference Digest of Technical Papers, 110-111.

Maruyama, Y., Blacksberg, J., and Charbon, E., 2014. A 1024 x 8, 700-ps Time-Gated SPAD Line Sensor for Planetary Surface Exploration With Laser Raman Spectroscopy and LIBS. IEEE Journal of Solid-State Circuits 49, 179-189.

Maurice, S., Wiens, R., Anderson, R., Beyssac, O., Bonal, L., Clegg, S., DeFlores, L., Dromart, G., Fischer, W., Forni, O., 2015. Science objectives of the SuperCam instrument for the Mars 2020 rover. 46, 2818.

McLennan, S., Bell, J., Calvin, W., Christensen, P., Clark, B.d., De Souza, P., Farmer, J., Farrand, W., Fike, D., Gellert, R., 2005. Provenance and diagenesis of the evaporite-bearing Burns Formation, Meridiani Planum, Mars. Earth Planet. Sci. Lett. 240, 95-121.

Melezhik, V.A., Fallick, A.E., Medvedev, P.V. and Makarikhin, V.V., 2001. Palaeoproterozoic magnesite: lithological and isotopic evidence for playa/sabkha environments. Sedimentology 48 (2), 379-397.

Melvin, J.L., 1991. *Evaporites, petroleum and mineral resources*: Elsevier, Garland.

Meyers, P.A., 1994. Preservation of elemental and isotopic source identification of sedimentary organic matter. Chem. Geol. 114, 289-302.

Milliken, R.E., Grotzinger, J.P. and Thomson, B.J., 2010. Paleoclimate of Mars as captured by the stratigraphic record in Gale Crater. Geophysical Research Letters, 37(4).

Mojzsis, S.J., Arrhenius, G., McKeegan, K.D., Harrison, T.M., Nutman, A.P., Friend, C.R., 1996. Evidence for life on Earth before 3,800 million years ago. Nature 384, 55-59.

Moore, J.N., 1979. Geology map of the San Emidio, Nevada geothermal area. (No. DOE/ET/28392-33).

Morris, E.H., 1928. An Aboriginal salt mine at Camp Verde, Arizona. American Museum of Natural History.

Morris, R.V., Lauer, H.V., Lawson, C.A., Gibson, E.K., Nace, G.A., Stewart, C., 1985. Spectral and other physicochemical properties of submicron powders of hematite (α-Fe2O3), maghemite (γ-Fe2O3), magnetite (Fe3O4), goethite (α-FeOOH), and lepidocrocite (γ-FeOOH). J Geophys. Res.: Solid Earth 90, 3126-3144.

Morris, R.V., Ruff, S.W., Gellert, R., Ming, D.W., Arvidson, R.E., Clark, B.C., Golden, D.C., Siebach, K., Klingelhofer, G., Schroder, C., Fleischer, I., Yen, A.S., Squyres, S.W., 2010. Identification of carbonate-rich outcrops on Mars by the Spirit rover. Science 329 (5990), 421-424.

Morris, R. V., et al., 2016. Silicic volcanism on Mars evidenced by tridymite in high-SiO2 sedimentary rock at Gale crater. PNAS, 201607098.

Mulac, A.J., Flower, W.L., Hill, R.A. and Aeschliman, D.P., 1978. Pulsed spontaneous Raman scattering technique for luminous environments. Applied Optics 17, 2695-2699.

Muller, K., Waloszek, D., Maas, A., 2009. *Fossils and Strata, Morphology, Ontogeny and Phylogeny of the Phosphatocopina (Crustacea) from the Upper Cambrian Orsten of Sweden:* John Wiley & Sons.

Murchie, S.L., Mustard, J.F., Ehlmann, B.L., Milliken, R.E., Bishop, J.L., McKeown, N.K., Noe Dobrea, E.Z., Seelos, F.P., Buczkowski, D.L., Wiseman, S.M., 2009. A synthesis of Martian aqueous mineralogy after 1 Mars year of observations from the Mars Reconnaissance Orbiter. J Geophy. Res.: Planets (1991–2012) 114.

Mustard, J., Adler, M., Allwood, A., Bass, D., Beaty, D., Bell III, J., Brinckerhoff, W., Carr, M., Des Marais, D., Drake, B., 2013. Report of the Mars 2020 Science Definition Team, 154 pp., posted July, 2013, by the Mars Exploration Program Analysis Group (MEPAG). Retrieved from http://mepag.jpl.nasa.gov/reports/MEP. Mars_2020_SDT_ Report_Final.pdf

Nachon, M., Clegg, S., Mangold, N., Schröder, S., Kah, L., Dromart, G., Ollila, A., Johnson, J., Oehler, D., Bridges, J., 2014. Calcium sulfate veins characterized by ChemCam/Curiosity at Gale Crater, Mars. Journal of Geophysical Research: Planets, 119, pp.1991-2016.

NASA, 2015, NASA Astrobiology Strategy. Hays, L., Ed. Retrieved from https://astrobiology.nasa.gov/uploads/filer_public/01/28/01283266-e401-4dcb-8e05-3918b21edb79/nasa_astrobiology_strategy_2015_151008.pdf

National Research Council (NRC), 2011. *Vision and Voyages: For planetary science in the decade 2013-2022*: National Academies Press.

Nations, J.D., Hevly, R.H., Blinn, D.W., Landye, J.J., 1981. Paleontology, paleoecology, and depositional history of the Miocene-Pliocene Verde Formation. Yavapai County, Arizona: AZ Geol. Soc. Digest 13, 133-149.

Nichols, E., Howes, H., Wilber, D., 1918. The photoluminescence and kathodo-luminescence of calcite. Phys. Rev. 12 (5), 351.

Noe Dobrea, E., Wray, J., Calef, F., Parker, T., Murchie, S., 2012. Hydrated minerals on Endeavour Crater's rim and interior, and surrounding plains: New insights from CRISM data. Geophys. Res. Lett. 39.

Norton, C. F., and W.D. Grant, 1988. Survival of halobacteria within fluid inclusions in salt crystals. J Gen. Microbiol. 134, 1365-1373.

Norton, C. F., T. J. McGenity, and W. D. Grant, 1993. Archaeal halophiles (halobacteria) from two British salt mines. J. Gen. Microbiol.139, 1077-1081.

Novak, K.S., Kempenaar, J.G., Redmond, M., Bhandari, P., 2015. Preliminary surface termal design of the Mars 2020 Rover. In 45th International Conference on Environmental Systems.

Osborne, R.H., Licari, G.R., Link, M.H., 1982. Modern lacustrine stromatolites, Walker Lake, Nevada. Sediment. Geol. 32, 39-61.

Ott, R., 2014 Incision History of the South-Western Colorado Plateau Margin. Master's Thesis, Universität Tübingen.

Pasteris, J.D., Wopenka, B., 2003. Necessary, but not sufficient: Raman identification of disordered carbon as a signature of ancient life. Astrobiology 3 (4), 727-738.

Phillips, K.A., 1987, Arizona Industrial Minerals, 2nd. Edition, Arizona Department of Mines & Minerals Mineral Report 4, 185.

Popa, R., Kinkle, B.K., Badescu, A., 2004. Pyrite framboids as biomarkers for iron-sulfur systems. Geomicrobiol. J. 21, 193-206.

Powell, T., 1986. Petroleum geochemistry and depositional setting of lacustrine source rocks. Mar. Pet. Geol. 3, 200-219.

Prasad, P., Pradhan, A., Gowd, T.N., 2001. In situ micro-Raman investigation of dehydration mechanism in natural gypsum. Current Science Bangalore 80, 1203-1207.

Rapin, W., Meslin, P.Y., Maurice, S., Vaniman, D., Nachon, M., Mangold, N., Schröder, S., Gasnault, O., Forni, O., Wiens, R.C. and Martínez, G.M., 2016. Hydration state of calcium sulfates in Gale crater, Mars: Identification of bassanite veins. Earth and Planetary Science Letters, 452,197-205.

Ray, M.D., Sedlacek, A.J., Wu, M., 2000. Ultraviolet mini-Raman lidar for stand-off, in situ identification of chemical surface contaminants. Rev. Sci. Instrum. 71, 3485-3489.

Richardson, C.D., Hinman, N.W., Scott, J.R., 2009. Effect of thenardite on the direct detection of aromatic amino acids: implications for the search for life in the solar system. Int. J.of Astrobiol. 8, 291-300.

Rividi, N., van Zuilen, M., Philippot, P., Ménez, B., Godard, G. and Poidatz, E., 2010. Calibration of carbonate composition using micro-Raman analysis: application to planetary surface exploration. Astrobiology 10, 293-309.

Robinson, W., 1969. Kerogen of the Green River formation, in Organic Geochemistry. Springer, pp. 619-637.

Rothschild, L. J., Giver, L. J., White, M. R. and Mancinelli, R. L., 1994. Metabolic activity of microorganisms in gypsum-halite crusts. J. Phycol. 30, 431–438.

Ruff, S.W., Farmer, J.D., Calvin, W.M., Herkenhoff, K.E., Johnson, J.R., Morris, R.V., Rice, M.S., Arvidson, R.E., Bell, J.F., Christensen, P.R., 2011. Characteristics, distribution, origin, and significance of opaline silica observed by the Spirit rover in Gusev crater, Mars. J. Geophys. Res.: Planets (1991–2012) 116.

Rull, F., 2014. Development Status of the Raman Instrument (RLS) for Exomars 2018 Mission and Scientific Operation Mode on Mars. LPI Contributions 1783, 11th International GeoRaman Conference, abstract #5056.

Schidlowski, M., Appel, P.W., Eichmann, R., Junge, C.E., 1979. Carbon isotope geochemistry of the 3.7×10^9-yr-old Isua sediments, West Greenland: implications for the Archaean carbon and oxygen cycles. Geochim. Cosmochim. Acta 43, 189-99.

Schidlowski, M., 1988. A 3,800-million-year isotopic record of life from carbon in sedimentary rocks. Nature 333, 313-318.

Schidlowski, M., 2001. Carbon isotopes as biogeochemical recorders of life over 3.8 Ga of Earth history: Evolution of a concept. Precambrian Res. 106, 117-134.

Schopf, J.W., 1993. Microfossils of the Early Archean Apex chert: new evidence of the antiquity of life. Science 260, 640-646.

Schopf, J.W., Kudryavtsev, A.B., Agresti, D.G., Wdowiak, T.J., Czaja, A.D., 2002. Laser–Raman imagery of Earth's earliest fossils. Nature 416, 73-76.

Schopf, J.W., Farmer, J.D., Foster, I.S., Kudryavtsev, A.B., Gallardo, V.A., Espinoza, C., 2012. Gypsum-permineralized microfossils and their relevance to the search for life on Mars. Astrobiology 12, 619-633.

Schouten, S., Hartgers, W.A., Lòpez, J.F., Grimalt, J.O., Damsté, J.S.S., 2001. A molecular isotopic study of 13 C-enriched organic matter in evaporitic deposits: recognition of CO 2-limited ecosystems. Org. Geochem. 32, 277-286.

Schreiber, B.C., Philp, R.P., Benali, S., Helman, M.L., Peña, J.A., Marfil, R., Landais, P., Cohen, A.D. and Kendall, C.S.C., 2001. Characterisation of organic matter formed in hypersaline carbonate/evaporite environments: hydrocarbon potential and biomarkers obtained through artificial maturation studies. Journal of Petroleum Geology 24 (3), 309-338.

Senftle, J., Brown, J., Larter, S., 1987. Refinement of organic petrographic methods for kerogen characterization. Int. J. Coal Geol. 7, 105-117.

Sharma, S.K., Lucey, P.G., Ghosh, M., Hubble, H.W., Horton, K.A., 2003. Stand-off Raman spectroscopic detection of minerals on planetary surfaces. Spectrochim. Acta Part A: Mol. Biomol. Spectrosc. 59, 2391-2407.

Shkolyar, S. and J. D. Farmer, 2012. Steps towards choosing Martian samples for fossil biosignature analysis of kerogen: fluorescence microscopy and Raman spectroscopy applications to various analog samples, AGU Fall Mtg., San Francisco, CA, Vol. 1, abstract #P13A-1890, p. 1890.

Shkolyar, S., Farmer, J. D., Alerstam, E., Maruyama, Y., and Blacksberg, J., 2013. Identifying fossil biosignatures and minerals in Mars analog samples using time-resolved Raman spectroscopy, In AGU Fall Meeting Abstracts, Vol. 1, abstract #P51G-1802, p. 1802.

Shkolyar and J. D. Farmer, 2013. Insights on fossil biosignature analysis of kerogen from fluorescence microscopy and Raman spectroscopy studies of samples of diverse Mars analog environments and ages, presented at The 2012 Gordon Research Seminar on The Future of Geobiology: Perspectives from Graduate and Postdoctoral Research, Ventura, CA.

Shkolyar, S., Farmer, J. D., and Blacksberg, J., 2014a. Fossil Biosignatures, Mars Sample Return, and Raman Spectroscopy. Presented at the 11th GeoRaman Conference, St. Louis, MO.

Shkolyar, S., Farmer, J. D., and Blacksberg, J., 2014b. Identifying High Priority Fossil Biosignatures in Mars Analog Materials Using Raman Spectroscopy. Eighth International Conference on Mars, July 14-18, 2014, Pasadena, California. LPI Contribution #1791, p.1037.

Shkolyar, S., and J. D. Farmer, 2015. Informing Biosignature Studies on Mars: Evaluating Habitable Environments and Preservation Potential in Verde Valley, AZ. In Astrobiology Graduate Conference (AbGradCon), Madison, WI.

Shkolyar, S. and Farmer, J.D., 2016. Impact of Diagenesis on Biosignature Preservation Potential in Playa Lake Evaporites of the Verde Formation, Arizona: Implications for Mars Exploration. In Biosignature Preservation and Detection in Mars Analog Environments, LPI Contributions, 1912, astract #2003.

Shreve, A.P., Cherepy, N.J., Mathies, R.A., 1992. Effective rejection of fluorescence interference in Raman spectroscopy using a shifted excitation difference technique. Appl. Spectrosc. 46 (4), 707-711.

Skok, J., Mustard, J., Ehlmann, B., Milliken, R., Murchie, S., 2010. Silica deposits in the Nili Patera caldera on the Syrtis Major volcanic complex on Mars. Nat. Geosc. 3(12), 838-841.

Skulinova, M., Lefebvre, C., Sobron, P., Eshelman, E., Daly, M., Gravel, J.-F., Cormier, J.-F., Châteauneuf, F., Slater, G., Zheng, W., Koujelev, A., Léveillé, R., 2014. Time-resolved stand-off UV-Raman spectroscopy for planetary exploration. Planet. Sp. Sci. 92, 88–100.

Slotznick, S.P. and Shim, S.H., 2008. In situ Raman spectroscopy measurements of MgAl2O4 spinel up to 1400 C. Amer. Mineralog. 93, 470-476.

Som, S.M., Foing, B.H., 2012. Thermal degradation of organic material by portable laser Raman spectrometry. Int. J Astrobiol. 11, 177-186.

Squyres, S.W., Grotzinger, J.P., Arvidson, R.E., Bell, J.F.,3rd, Calvin, W., Christensen, P.R., Clark, B.C., Crisp, J.A., Farrand, W.H., Herkenhoff, K.E., Johnson, J.R., Klingelhofer, G., Knoll, A.H., McLennan, S.M., McSween, H.Y.,Jr, Morris, R.V., Rice, J.W.,Jr, Rieder, R., Soderblom, L.A., 2004. In situ evidence for an ancient aqueous environment at Meridiani Planum, Mars. Science 306, 1709-1714.

Squyres, S.W., Knoll, A.H., Arvidson, R.E., Clark, B.C., Grotzinger, J.P., Jolliff, B.L., McLennan, S.M., Tosca, N., Bell, J.F.,3rd, Calvin, W.M., Farrand, W.H., Glotch, T.D., Golombek, M.P., Herkenhoff, K.E., Johnson, J.R., Klingelhofer, G., McSween, H.Y., Yen, A.S., 2006. Two years at Meridiani Planum: results from the Opportunity Rover. Science 313, 1403-1407.

Squyres, S.W., Arvidson, R.E., Bell, J.F.,3rd, Calef, F.,3rd, Clark, B.C., Cohen, B.A., Crumpler, L.A., de Souza, P.A.,Jr, Farrand, W.H., Gellert, R., Grant, J., Herkenhoff, K.E., Hurowitz, J.A., Johnson, J.R., Jolliff, B.L., Knoll, A.H., Li, R., McLennan, S.M., Ming, D.W., Mittlefehldt, D.W., Parker, T.J., Paulsen, G., Rice, M.S., Ruff, S.W., Schroder, C., Yen, A.S., Zacny, K., 2012. Ancient impact and aqueous processes at Endeavour Crater, Mars. Science 336 (6081), 570-576.

Stopar, J.D., Lucey, P.G., Sharma, S.K., Misra, A.K., Taylor, G.J., Hubble, H.W., 2005. Raman efficiencies of natural rocks and minerals: Performance of a remote Raman system for planetary exploration at a distance of 10 meters. Spectrochim. Acta Part A: Mol. Biomol. Spectrosc. 61, 2315-2323.

Storrie-Lombardi, M.C., Hug, W.F., McDonald, G.D., Tsapin, A.I., Nealson, K.H., 2001. Hollow cathode ion lasers for deep ultraviolet Raman spectroscopy and fluorescence imaging. Rev. Sci. Instrum. 72, 4452–4459.

Summons, R., Hallman, C., 2014. 12.2–Organic geochemical signatures of early life on Earth. Treatise on Geochemistry, 33-46.

Summons, R.E., Amend, J.P., Bish, D., Buick, R., Cody, G.D., Des Marais, D.J., Dromart, G., Eigenbrode, J.L., Knoll, A.H., Sumner, D.Y., 2011. Preservation of martian organic and environmental records: final report of the Mars Biosignature Working Group. Astrobiology 11, 157-181.

Surdam, R.C., Stanley, K., 1979. Lacustrine sedimentation during the culminating phase of Eocene Lake Gosiute, Wyoming (Green River Formation). Geol. Soc. of Amer. Bulletin 90, 93-110.

Talbot, M., 1990. A review of the palaeohydrological interpretation of carbon and oxygen isotopic ratios in primary lacustrine carbonates. Chemical Geology: Isotope Geoscience Section 80, 261-279.

Tarcea, N., Harz, M., Rösch, P., Frosch, T., Schmitt, M., Thiele, H., Hochleitner, R., Popp, J., 2007. UV Raman spectroscopy—a technique for biological and mineralogical in situ planetary studies. Spectrochim. Acta Part A: Mol. Biomol. Spectrosc. 68, 1029-1035.

Thickpenny, A., 1984. The sedimentology of the Swedish alum shales. Geological Society, London, Special Publications 15(1), 511-525.

Thomson, B.J., Bridges, N.T., Milliken, R., Baldridge, A., Hook, S.J., Crowley, J.K., Marion, G.M., de Souza Filho, C.R., Brown, A.J. and Weitz, C.M., 2011. Constraints on the origin and evolution of the layered mound in Gale Crater, Mars using Mars Reconnaissance Orbiter data. Icarus, 214 (2), 413-432.

Tuinstra, F., Koenig, J.L., 1970. Raman spectrum of graphite. J. Chem. Phys. 53, 1126-1130.

Tursina, T., Yamnova, I., Shoba, S., 1980. Combined stage-by-stage morphological, mineralogical and chemical study of the composition and organization of saline soils. Soviet Soil Science.

Twenter, F.R., Metzger, D.G., 1963. Geology and Ground Water in Verde Valley--the Mogollon Rim Region, Arizona. US Government Printing Office.

Utrilla, R., Vázquez, A. and Anadón, P., 1998. Paleohydrology of the Upper Miocene Bicorb Lake (eastern Spain) as inferred from stable isotopic data from inorganic carbonates. Sedimentary Geology 121 (3), 191-206.

Van Kranendonk, M.J., Webb, G.E., Kamber, B.S., 2003. Geological and trace element evidence for a marine sedimentary environment of deposition and biogenicity of 3.45 Ga stromatolitic carbonates in the Pilbara Craton, and support for a reducing Archaean ocean. Geobiol. 1, 91-108.

van Zuilen, M.A., Lepland, A., Teranes, J., Finarelli, J., Wahlen, M., Arrhenius, G., 2003. Graphite and carbonates in the 3.8 Ga old Isua supracrustal belt, southern West Greenland. Precambrian Res. 126, 331-348.

Vance, R.K., Condie, K.C., 1987. Geochemistry of footwall alteration associated with the early Proterozoic United Verde massive sulfide deposit, Arizona. Economic Geology 82, 571-586.

Vandenbroucke, M., Largeau, C., 2007. Kerogen origin, evolution and structure. Org. Geochem. 38, 719-833.

Vaniman, D.T., Bish, D.L., Ming, D.W., Bristow, T.F., Morris, R.V., Blake, D.F., Chipera, S.J., Morrison, S.M., Treiman, A.H., Rampe, E.B., Rice, M., Achilles, C.N., Grotzinger, J.P., McLennan, S.M., Williams, J., Bell, J.F.,3rd, Newsom, H.E., Downs, R.T., Maurice, S., Sarrazin, P., Yen, A.S., Morookian, J.M., Farmer, J.D., Stack, K., Milliken, R.E., Ehlmann, B.L., Sumner, D.Y., Berger, G., Crisp, J.A., Hurowitz, J.A., Anderson, R., Des Marais, D.J., Stolper, E.M., Edgett, K.S., Gupta, S., Spanovich, N., and the MSL Science Team, 2014. Mineralogy of a mudstone at Yellowknife Bay, Gale crater, Mars. Science 343 (6169), 1243480.

Vitek, P., Edwards, H.G., Jehlicka, J., Ascaso, C., De los Rios, A., Valea, S., Jorge-Villar, S.E., Davila, A.F., Wierzchos, J., 2010. Microbial colonization of halite from the hyper-arid Atacama Desert studied by Raman spectroscopy. Philos. Trans. A. Math. Phys. Eng. Sci. 368, 3205-3221.

Vreeland, R. H., W.D. Rosenzweig, and D.W. Powers, 2000. Isolation of a 250 million-year-old halotolerant bacterium from a primary salt crystal. Nature 407 (6806), 897-900.

Wadell, J.S., 1972. Sedimentation and Stratigraphy of the Verde Formation (Pliocene), Yavapai County, Arizona. MS Thesis, Arizona State University.

Wang, A., Haskin, L.A., Lane, A.L., Wdowiak, T.J., Squyres, S.W., Wilson, R.J., Hovland, L.E., Manatt, K.S., Raouf, N., Smith, C.D., 2003. Development of the Mars microbeam Raman spectrometer (MMRS). Journal of Geophysical Research: Planets (1991–2012) 108.

Wang, A., Freeman, J.J., Jolliff, B.L., Chou, I., 2006. Sulfates on Mars: A systematic Raman spectroscopic study of hydration states of magnesium sulfates. Geochim. Cosmochim. Acta 70 (24), 6118-6135.

Wang, J., Mullins, O.C., 1997. Fluorescence of limestones and limestone components. Appl. Spectrosc. 51, 1890-1895.

Warren, J.K., 1986. Shallow-Water Evaporitic Environments and their Source Rock Potential: Perspectives. Journal of Sedimentary Research 56.

Warren, J., 1999. *Evaporites: Their evolution and economics*: Wiley-Blackwell.

Warren, J.K., 2006. *Evaporites: Sediments, resources and hydrocarbons*: Springer Science & Business Media.

Warren, J.K., 2010. Evaporites through time: Tectonic, climatic and eustatic controls in marine and nonmarine deposits. Earth-Sci. Rev. 98, 217-268.

Westall, F., 2008. Morphological biosignatures in early terrestrial and extraterrestrial materials. Space Science Reviews 135, 95-114.

Westall, F., Cavalazzi, B., 2011. Biosignatures in rocks. Encyclopedia of Geobiology, 189-201.

Winters, Y.D., Lowenstein, T., Timofeeff, M., 2013. Identification of carotenoids in ancient salt from Death Valley, Saline Valley, and Searles Lake, California, using laser Raman spectroscopy. Astrobiology 13, 1065-1080.

Wynn-Williams, D., Edwards, H., 2000. Proximal Analysis of Regolith Habitats and Protective Biomolecules in Situ by Laser Raman Spectroscopy: Overview of Terrestrial Antarctic Habitats and Mars Analogs. Icarus 144, 486-503.

Yaney, P.P., 1972. Reduction of fluorescence background in Raman spectra by the pulsed Raman technique. JOSA 62, 1297-1303.

Zucker, R. and Shim, S.H., 2009. In situ Raman spectroscopy of MgSiO3 enstatite up to 1550 K. Amer. Mineralogist 94,1638-1646.

APPENDIX A

UNDERSTANDING THE EFFECTS OF GATING TO QUANTIFY FLUORESCENCE REDUCTION

The effects of gating on fluorescence reduction in the UV-G Raman system were quantified using a custom-developed method. Figure A.1 illustrates this method as applied to the Alum Formation marine sandstone (Chapter 4, section 4.3.1.3). First, time-resolved fluorescence spectra were acquired, and fluorescence decay curves were extracted on the most prominent band. The total signal of the resulting decay curve was integrated and divided by the integrated Raman time-decay signal of a gypsum standard, taking the ratio as a measure of gating efficiency (i.e., the percentage of fluorescence removed). Ratios were calculated for given percentages of the total Raman signal (Raman signal strength), chosen to be 50% and 80% signal strength (Table A.1). This analysis was performed on the silicified mudstone, marine sandstone, both lamination types in the sulfate evaporite, the lacustrine carbonate, and three optically diverse matrix regions of the stromatolitic limestone. (See Chapter 4 for sample details.)

Results in Table A.1 obtained with this method serve as lower bounds based on only the first 20 ns of the total fluorescence acquisition. Fluorescence could be further reduced with longer gates and by integrating over longer acquisition times (i.e., 100 ns instead of 20 ns), bearing in mind that at the expense of losing data quality and signal strength, gating ratios could be further improved with longer acquisitions.

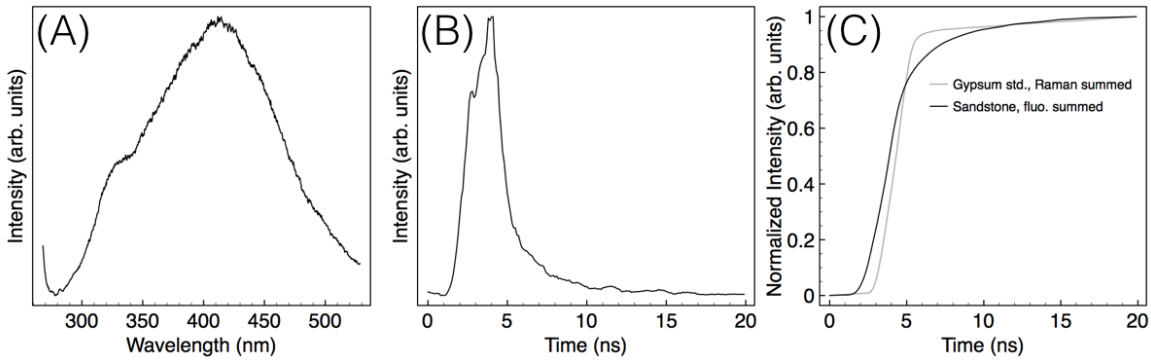

Figure A.1. Quantifying gating effects on fluorescence reduction. This example uses the spectrum of the marine sandstone. **(A)** The short gate is shown of a fluorescence spectrum of the matrix whose most prominent feature is a broad symmetrical feature centered near 425 nm. The fluorescence decay curve for this feature is shown in (B). The integral of the fluorescence decay is shown in **(C)** over the 20-ns acquisition (black). Overlaid (grey) is an integrated Raman spectrum from the gypsum standard, taken under the same conditions as the fluorescence data. In **(C)**, the intensity axis is normalized to 1.

Table A.1

Selected Results Showing Quantified Fluorescence Removal

	Percentage fluorescence removed			
Raman signal strength	**Organics**	**Minerals**	**Average, percent**	$\sigma_{\bar{x}}$
80%	22.9 - 40.1	42.1 - 74.6	62.9	15.7
50%	38.0 - 55.0	54.2 - 84.8	50.1	19.1

Table A.1. Selected results showing quantified fluorescence removal at 80% and 50% Raman signal strength in selected samples for fluorescence bands attributed to organic and mineral sources. Average percentages and standard deviations ($\sigma_{\bar{x}}$) in both cases are also given

BIOGRAPHICAL SKETCH

Svetlana Shkolyar was born in Kichinev, Moldova. She and her family immigrated to Jacksonville, Florida, where she grew up, attended school, and eventually enrolled at the University of North Florida. There, she graduated with a bachelor's degree in Physics with Interdisciplinary Honors (U. of North Florida, Jacksonville, FL). Her interests in inspiring the public's engagement in space exploration led her to pursue an MA in Mass Communication with a focus on science communication (U. of Florida, Gainesville, FL). She then received an MS in Space Studies (U. North Dakota, Grand Forks, ND). Her NASA summer internships (Kennedy Space Center and Goddard Space Flight Center) solidified her interests in pursuing an astrobiology-focused PhD in the School of Earth and Space Exploration at ASU in Geological Sciences. While at ASU, she also worked on a project funded by NASA Space Grant to enhance science engagement among children by creating astrobiology-themed lessons for middle and high school educators. During her time at ASU, she served as an Executive Director at SAGANet.org, a grassroots online social network for astrobiology researchers, students, mentors, and educators. When Svetlana is not thinking about Mars or engaging the public in science, she enjoys salsa dancing and performing another kind of science experiment: cooking.